



Provided by the author(s) and University of Galway in accordance with publisher policies. Please cite the published version when available.

Title	Processing of adaptive optics photoreceptor images and application to the study of healthy and diabetic retinas
Author(s)	Mariotti, Letizia
Publication Date	2017-11-17
Item record	http://hdl.handle.net/10379/6975

Downloaded 2024-04-25T06:40:00Z

Some rights reserved. For more information, please see the item record link above.



PROCESSING OF ADAPTIVE OPTICS
PHOTORECEPTOR IMAGES AND
APPLICATION TO THE STUDY OF
HEALTHY AND DIABETIC RETINAS

by Letizia Mariotti

Supervisor: Dr. Nicholas Devaney



A thesis submitted in partial fulfilment of the
requirements for the degree of Doctor of Philosophy

Applied Optics Group, School of Physics
National University of Ireland, Galway

November 2017

DECLARATION

The work in this thesis is based on research carried out at the Applied Optics Group, School of Physics, National University of Ireland, Galway. No part of this thesis has been submitted elsewhere for any other degree or qualification and it is all my own work unless otherwise referenced in the text.

Letizia Mariotti
Galway, November 2017

ABSTRACT

The introduction of adaptive optics (AO) into vision science has made it possible for clinicians to study the human retina in vivo with high-resolution images. The study of AO images of the cone photoreceptor mosaic is becoming a fundamental step in the assessment and monitoring of the health of the retina and in the understanding of the photoreceptor physiology. However, the development of automated algorithms for the analysis of such high amount of information is a necessary step towards the use of AO imaging in clinical practice.

In this thesis we aimed at developing a procedure for the automated analysis of the cone mosaic in AO images and we showed its application to the study of properties of cone reflectance in healthy eyes and eyes affected by retinopathy. The work towards the achievement of this aim is presented here in the form of three journal publications and one conference paper. Using a custom developed technique for the simulation of realistic cone images, we optimised and evaluated the performance of automated cone detection algorithms. Using automated cone detection and semi-automated retinal vessel segmentation, we analysed the cone mosaic of a healthy subject over time. We observed that the difference in cone reflectance increases with the time separation between the data acquisitions, negatively affecting the tracking of the same cones over time. With the same method we then investigated cone reflectance in healthy and mild non-proliferative diabetic retinopathy subjects. We were able to determine cone reflectance metrics that quantified reflectance spatial distribution and showed a significant difference between the two groups. Finally, we discuss possible future directions for research that could build on our results.

ACKNOWLEDGMENTS

*The highest reward for a man's toil
is not what he gets by it
but what he becomes by it*

— John Ruskin

First of all, I would like to give a special thank to my supervisor, Dr. Nicholas Devaney. If my PhD was successful, I owe it especially to him and to his constant help and guidance. Thanks to him, I had the amazing opportunity to come to Ireland, for which I will be always grateful. I would like to sincerely thank Gomathy, who even in the final stages of her PhD still found the time to share her codes and explain her work to me. I believe that my start wouldn't have been as easy without her precious help.

I then want to thank Marco for providing the images used in this work, for his helpful suggestions on the clinical aspects of the project and for giving me the opportunity to visit the Fondazione Bietti in Rome. I also thank Giuseppe, Daniela and the rest of the group for their help and for making me feel welcome during my time in Rome and during the ARVO meeting.

The past four years haven't been perfect, there were good times and not-so-good times, but what I learned from them will be with me for the rest of my life. When I think about it, I always feel very lucky of the people that I had the chance to meet here in Galway and that made these years fly. So I want to thank my colleagues in the Applied Optics Group (Colm, Conor, Ken, Kim, Mark, Niamh) and Lisa for welcoming me so warmly when I first arrived and for giving me their friendship. I also thank all the postgrads in the School of Physics, the ones that were here when I arrived as well as the new ones, for being such a great group of people. I am sure it wouldn't have been the same without all of you.

Vorrei fare un ringraziamento speciale ai miei genitori, a mio fratello e a mia sorella, che mi hanno sempre sostenuto nelle mie scelte. Nonostante mi sia trovata bene a Galway, come per me non é sempre stato facile stare lontano da casa cosí posso pensare che lo sia stato anche per voi avermi lontana. Vi ringrazio per non avermelo mai fatto pesare, facendo di ogni mio ritorno a casa una festa. Spero che saró in grado un giorno di restituirvi una minima parte di quello che mi avete dato.

I would like to thank the Irish Research Council for funding this project.

CONTENTS

ABSTRACT	iii
ACKNOWLEDGMENTS	iv
ACRONYMS	vii
PUBLICATIONS	viii
1 INTRODUCTION	1
1.1 The eye and the retina	2
1.1.1 Photoreceptor cells	4
1.2 Retinal imaging	4
1.2.1 Adaptive optics	7
1.2.2 Retinal imaging modalities in combination with adap- tive optics	9
1.2.2.1 The rtx1 camera	11
1.2.3 Imaging retinal structures with adaptive optics	13
1.2.3.1 Imaging of photoreceptors	15
1.2.3.2 Assessment of the cone photoreceptor mosaic	17
1.3 Clinical applications of adaptive optics retinal imaging	19
1.3.1 Adaptive optics imaging of retinal pathologies	20
1.3.1.1 Diabetic retinopathy	21
1.4 Retinal image processing	23
1.4.1 Image pre-processing	24
1.4.2 Ramaswamy's PhD thesis	26
1.4.3 Analysis and interpretation	26
1.4.3.1 Photoreceptor detection	28
1.4.3.2 Blood vessel segmentation	28
1.5 Aims and objectives	29
2 PAPER I	31
2.1 Contributions	31
3 CONFERENCE PAPER	42
3.1 Contributions	42
4 PAPER II	47
4.1 Contributions	47
5 PAPER III	68

5.1	Contributions	68
6	CONCLUSIONS	85
6.1	Summary of thesis work	85
6.1.1	Processing of the cone mosaic	85
6.1.2	Analysis of the cone mosaic over time	86
6.1.3	Cone mosaic reflectance in NPDR	86
6.2	Proposal for future work	87
6.2.1	Reliability of automated cone detection	87
6.2.2	Analysis of large retinal patches over time	87
6.2.3	Biomarkers for diabetic retinopathy	88
	BIBLIOGRAPHY	89
A	APPENDIX: ADDITIONAL IMAGES	101
B	APPENDIX: DETAILS ON STATISTICAL ANALYSIS	104
B.1	Choice of a mixed model	104
B.2	Procedure for the analysis of the data	105
B.3	Interpretation of the results	107

ACRONYMS

AMD	Age-related Macular Degeneration
ANOVA	Analysis of Variance
AO	Adaptive Optics
AOSLO	Adaptive Optics Scanning Laser Ophthalmoscope
BIC	Bayesian Information Criterion
CCD	Charged Couple Device
DM	Deformable Mirror
DR	Diabetic Retinopathy
FROC	Free-response Receiver Operating Characteristic
IS	Inner Segment
LED	Light-Emitting Diode
NA	Numerical Aperture
NPDR	Non Proliferative Diabetic Retinopathy
NND	Nearest Neighbour Distance
OCT	Optical Coherence Tomography
OS	Outer Segment
ROC	Receiver Operating Characteristic
SLD	Super-Luminescent Diode
SLO	Scanning Laser Ophthalmoscope
SNR	Signal to Noise Ratio
TD-OCT	Time Domain OCT

PUBLICATIONS

JOURNAL ARTICLES

Mariotti, L.; Devaney, N.; Lombardo, G. & Lombardo, M. Analysis of cone mosaic reflectance properties in healthy eyes and in eyes with non-proliferative diabetic retinopathy over time. *Investigative Ophthalmology & Visual Science* (2017) accepted for publication

Giannini, D.; Lombardo, G.; Mariotti, L.; Devaney, N.; Serrao, S. & Lombardo, M. Reliability and agreement between metrics of cone spacing in adaptive optics images of the human retinal photoreceptor mosaic. *Investigative Ophthalmology & Visual Science*, **58**, 3127-3137 (2017)

Mariotti, L.; Devaney, N.; Lombardo, G. & Lombardo, M. Understanding the changes of cone reflectance in adaptive optics flood illumination retinal images over three years. *Biomedical Optics Express*, **7**, 2807-2822 (2016)

Mariotti, L. & Devaney, N. Performance analysis of cone detection algorithms. *Journal of the Optical Society of America A*, **32**, 497-506 (2015)

CONFERENCE PROCEEDINGS

Mariotti, L. & Devaney, N. Background estimation in adaptive optics photoreceptor images. *IRISH MACHINE VISION & IMAGE PROCESSING Conference proceedings 2016*, Devaney, N. (Ed), (Irish Pattern Recognition & Classification Society), pp. 3-4 (2016)

Mariotti, L.; Devaney, N.; Lombardo, G. & Lombardo, M. Understanding the changes of cone reflectance in adaptive optics flood illumination retinal images over three years. *Investigative Ophthalmology & Visual Science*, (The Association for Research in Vision and Ophthalmology), **57**, 69-69 (2016)

Mariotti, L. & Devaney, N. Cone detection and blood vessel segmentation on AO retinal images *IRISH MACHINE VISION & IMAGE PROCESSING Conference proceedings 2015*, Dahyot, R.; Lacey, G.; Dawson-Howe, K.; Pitié, F. & Moloney, D. (Eds.), (Irish Pattern Recognition & Classification Society), 126-128 (2015)

INTRODUCTION

Among the human inner tissues, the retina has the unique property of being accessible for observation *in vivo* with non-invasive imaging tools. Imaging the retina has proved to be a powerful tool for the diagnosis of retinal pathologies. The advances made in the retinal imaging field in the last decades (above all, the implementation of adaptive optics) have provided the possibility not only to diagnose retinal diseases, but also to detect retinal abnormalities when the disease has not yet affected vision. In some cases, the early detection and cure allow the prevention of important vision alterations.

However, the detection of a greater number of retinal defects has to deal with the huge quantity of data to be analysed. Since the development of commercial adaptive optics (AO) imaging systems, the number of images with microscopic resolution available for analysis has greatly increased. The visual examination of a large number of images by an expert is time consuming, limiting either the thoroughness or the extent of retinal screening processes. Because of this, automated algorithms for the analysis of retinal images are a pressing need. Many studies have focused on this task, aiming at the development of reliable analysis algorithms that limit the human contribution to a minimum. The aim of this thesis is to investigate the automation of the analysis of high resolution AO images for the study of the retina, in particular of the cone photoreceptors.

In this introductory chapter, a brief review of the current state of AO retinal imaging and the processing of its data is presented. After an introduction to the eye anatomy, AO and the most common systems to image the retina are described in Section 1.2. After an overview of the clinical applications of AO in Section 1.3, Section 1.4 presents how the fundus images of the photoreceptor mosaic are processed.

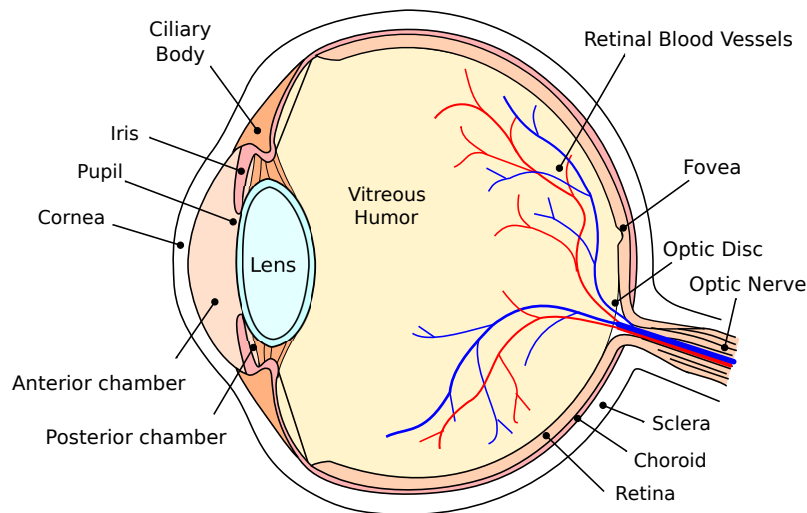


Figure 1.1: Cross section of the human eye (adapted from Wikimedia Commons)

1.1 THE EYE AND THE RETINA

The eye is the organ of our body that provides visual information on the external world. It works as an optical system that collects light and transmits information about its spatial and energetic distribution to the brain, where it is processed [1].

The vision process consists of many phases, and every part of the eye is dedicated to a specific one (Figure 1.1). The first part of the eye starting from the outside is the cornea, a transparent layer that surrounds and protects the front of the eye bulb. The light then enters the eye through an aperture called the pupil. The pupil is surrounded by the iris, a tissue that can vary the size of the pupil to modulate the amount of light that passes through it. Between the cornea and the pupil there is a curved space, the anterior chamber, that is filled with a viscous substance called the aqueous humour. The cornea and the anterior chamber contribute about $2/3$ of the optical power of the eye, but also to its aberrations [2].

The next optical component passed by the light is the crystalline lens, which accounts for the remaining $1/3$ of the optical power of the eye. The lens is a transparent structure, the shape of which can be modified by the ciliary body in a process called accommodation, in order to regulate the focal distance of the eye. The cornea, lens and iris together make up the eye's optical system.

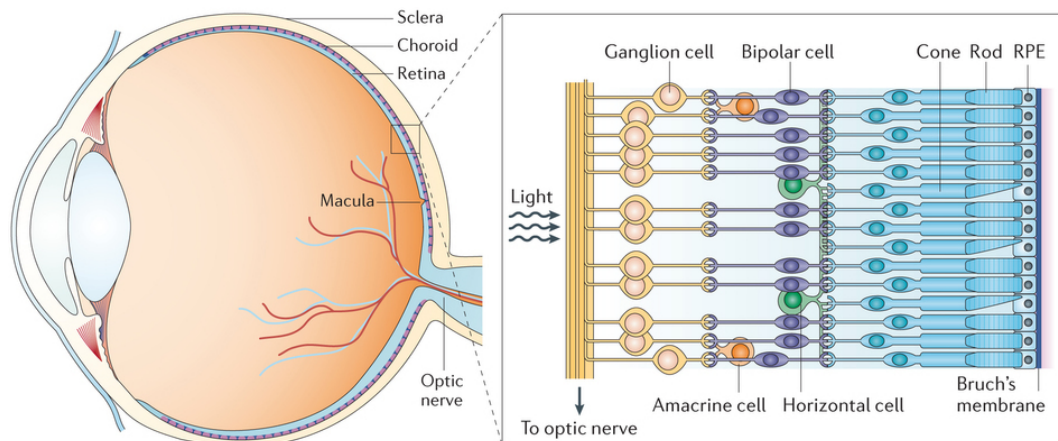


Figure 1.2: Schematic of retinal cell layers. Reprinted by permission from Macmillan Publishers Ltd.: Nature Reviews Drug Discovery [4], copyright 2015

Before reaching the back of the eye, the light passes the eye bulb, which is filled with a clear gel called the vitreous humour. The element of the eye in which the light is detected is the retina (Figure 1.2). In human vision, the retina is the sensor that receives the photons and converts them into nerve impulses. The retina tissue is approximately ~ 0.5 mm thick and develops from the embryonic forebrain, which makes the retina a part of the brain [3].

The retina itself is made up of numerous layers and in a way that is not intuitive the cells that are dedicated to the collection of the photons, the photoreceptors, lie in the back part of the retina. Because of this, the light has to first pass through other layers, which for this purpose are mostly transparent. However, in front of the retina there are the blood vessels that nourish the retinal cells, and their structure is opaque in retinal images.

Inward, i.e. towards the cornea and lens, of the photoreceptors there are layers of neuron cells, that connect the output information from the photoreceptors to the brain. The innermost layer of retinal neurons is made up of ganglion cells, each having a long axon that extends through the retina forming the so called retinal nerve fibre layer. The nerve fibres and the blood vessels exit the eye through an aperture in the retina called the optic disc or optic nerve head. No photoreceptors are present in the disc and so the disc represents a blind spot in vision [5].

1.1.1 *Photoreceptor cells*

The photoreceptors are of two types, the cones and the rods, named after their shape. The cones are the cells optimised to work in bright light and can be divided again in three subtypes, as they are sensitive to three different ranges of wavelengths. These are commonly referred to as short, medium and long wavelength cones after the wavelength at which they have their peak sensitivity (419 nm, 531 nm and 558 nm). The rods instead peak at only one wavelength (496 nm) and because of this do not sense colour, but are more sensitive and work best in low-light conditions [6, 7]. Despite these differences, cones and rods share a similar cellular structure (Figure 1.3). Both photoreceptor cells work by guiding the incoming light through the cell body, so that it reaches the cellular outer segment (OS), where the light-absorbing photopigments are confined. The photopigments are organised into discs that are created and shed during the cyclical renewal process of the OS [8–10].

On average, the human retina contains approximately 4.6 million cones and 92 million rods [11], but the distribution of the photoreceptors is not constant throughout the retina. In fact, most of the cones are located in the central region of the retina, called the macula. At the centre of the macula there is a small region called the fovea centralis (or simply fovea) that is the area specialized for sharp vision. Because of this, the fovea is an avascular zone and is filled only with densely packed cones. As the distance from the fovea increases, the density of cones decreases and the rods start to be present (Figure 1.4).

1.2 RETINAL IMAGING

The possibility to image the retina in vivo is essential for monitoring its health. The birth of retinal imaging can be traced to 1823, when Jan Evangelista Purkyně developed the principles of the ophthalmoscope. The second big step in the development of retinal imaging can be said to be the application of photography to the ophthalmoscope, that lead to the availability of pictures of the retina. The concept of fundus camera, developed in 1910, is still the basis of current retinal imaging techniques [12].

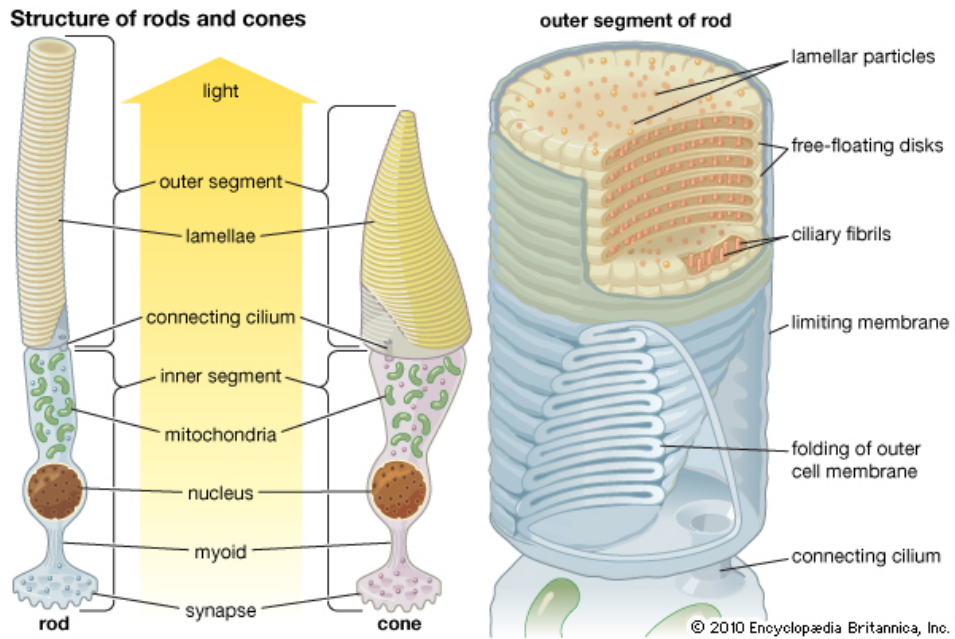


Figure 1.3: Schematic view of rod and cone photoreceptor cells (by courtesy of Encyclopaedia Britannica, Inc., copyright 2012; used with permission)

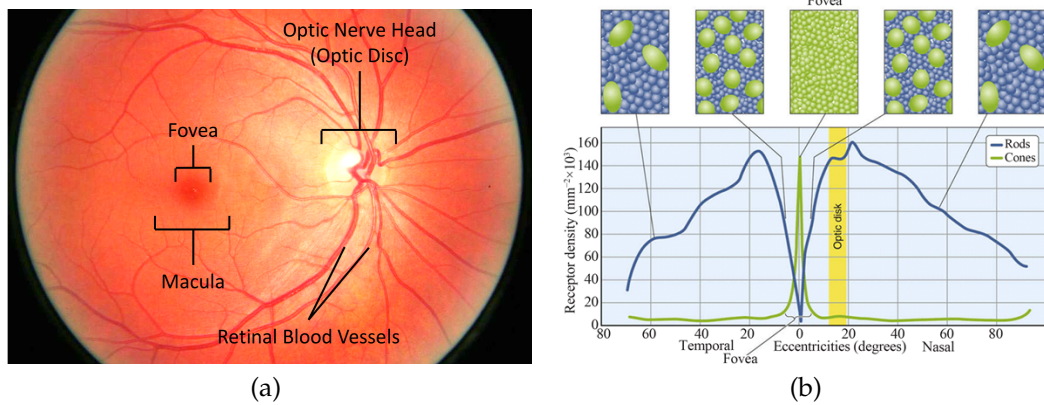


Figure 1.4: (a) Frontal view of the retina (adapted from Wikimedia Commons) (b) Density of cone and rod photoreceptor cells across the retina. Reprinted from [7], copyright 2009, with permission from Elsevier

Most of the techniques used so far to image the retina are in the category of fundus imaging, that is the “process whereby a 2D representation of the 3D retinal semi-transparent tissues projected onto the imaging plane is obtained using reflected light” [12].

A conventional fundus imager ophthalmoscope, or flood-illuminated ophthalmoscope, is a system where the retina is illuminated by a low spatial coherence light source and imaged on a detector. Invented in 1980 by Robert Webb [13], the scanning laser ophthalmoscope (SLO) is also a fundus imaging system, but the difference is that the images are acquired point-by-point, with a laser source that scans the retina and passes through a small aperture (pinhole) before reaching the detector. Unlike flood-illuminated ophthalmoscopes, the most common imaging modality for SLO systems is confocal imaging. In confocal imaging, a small aperture (the confocal pinhole) is positioned close to the detector, and this blocks light that is not scattered from near the plane of focus. In the human eye, the confocal pinhole allows for some optical sectioning, which is the primary advantage over conventional flood-illuminated ophthalmoscopes, but it also provides high-contrast images of the structure of interest [14]. Other imaging modes, such as nonconfocal detection schemes (large pinhole, offset pinhole, dark-field and split-detector) and motion contrast have also been explored recently, with promising results [14].

Optical coherence tomography (OCT) is an interferometric imaging technique that results in a depth image of the retinal layers based on their refractive index [12]. OCT employs a Michelson interferometer in conjunction with a low-coherence light source to coherently filter light reflecting from the retina. Compared to flood-illuminated ophthalmoscopes and SLO, OCT provides higher sensitivity and higher axial resolution [8]. There is a large array of different OCT designs, two of them are spectral domain OCT and swept source OCT. Systems of the first type record the reflected sample signature in the spectral domain. The spectral image is then processed and the result is an intensity reflectivity profile through depth of the retina [8]. In the second type, instead of the super-luminescent diode (SLD) laser typical of spectral domain OCT a short-cavity swept laser is used, which is tunable and can sweep across a broad band of wavelengths with each scan [15].

Until the late 1990s the quality of the pictures taken using fundus cameras was severely limited by the aberrations and scattering due to the optical components of the eye [16]. After the development of digital retinal imaging, adaptive optics and its implementation for clinical use is believed to be the next technique to lead to great advances in the field.

1.2.1 *Adaptive optics*

Adaptive optics (AO) was first developed in astronomy to deal with the effects of atmospheric turbulence on the light coming from astronomical sources. The presence of the atmosphere prevents ground-based telescopes from achieving diffraction limited resolution, as the light wavefronts from astronomical objects are not flat any more but are degraded by the passage through the atmospheric turbulence.

Introduced by Babcock in 1953 [17], the basic idea of AO is that the light wavefronts that are modified by the atmospheric turbulence can be restored. In fact, if the perturbation due to the atmosphere can be measured, then a correction that compensates for it can be applied to the perturbed wavefront in order to retrieve the unperturbed one. The same concept has, in the last decades, been introduced to retinal imaging systems, where the wavefront correction compensates for the aberrations caused by the optics of the eye [8, 18].

Classical AO systems are composed of three parts (Figure 1.5): a sensor, a corrector and a controller [19]. The sensor is dedicated to measurement of the aberrations of a beam of light as it is backscattered from the retina through the eye optics. The most common type of wavefront sensor used nowadays is the Shack-Hartmann wavefront sensor [20], which is made up of an array of lenslets. Each lenslet focuses a portion of the light beam on a charge coupled device (CCD) array where it is detected. If the wavefront is aberration-free, the light is focused on a regular array of spots; if instead the wavefront is aberrated, the spots deviate from their reference positions. The deviation of the spot positions is proportional to the tilt of the wavefront (first derivative of the wavefront) within the area of the corresponding lenslet. Other promising sensing techniques that have been developed as alternatives to the Shack-Hartmann include curvature sensing, pyramid sensing and interferometry [2], but Shack-Hartmann seems

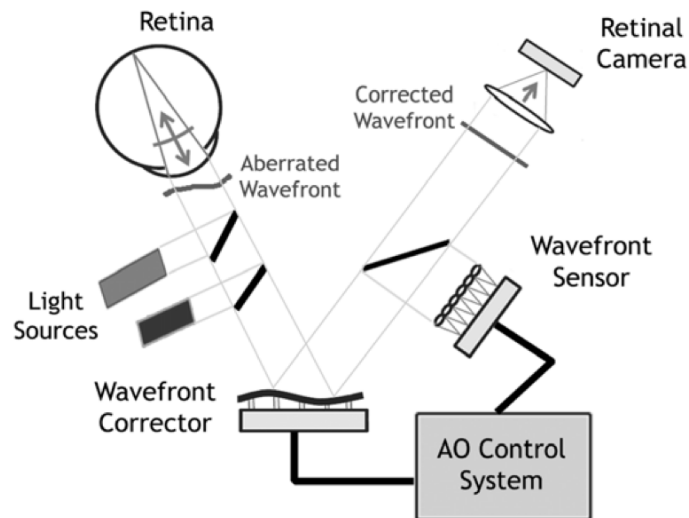


Figure 1.5: Basic layout of an AO system for retinal imaging (reproduced from [2]).

to be still the best approach for AO retinal imaging [14]. Besides wavefront sensing, wavefront sensor-less approaches to AO are also possible. In these systems, the quality of the acquired images (e.g. sharpness) is used to evaluate the effectiveness of the wavefront correction[21].

When the aberrations are measured, they are passed to the controller, which is essentially a computer that calculates and transmits spatial and temporal instructions to the corrector in order to compensate for the measured aberrations. Most recent systems use AO correction in closed loop mode, with an operating speed of several Hz. To determine the efficiency of the wavefront correction, the root mean square error of the residual wavefront can be estimated by the Shack-Hartmann [21].

The purpose of the corrector element in the AO loop is to modify its shape or its physical properties so that the outgoing light wavefront is aberration-corrected. There are two main categories into which the correctors are divided: piston segmented devices and continuous surface mirrors. The correction methods include phase conjugation, computer-generated holograms and deformable mirrors. The way in which phase errors are corrected is by changing the optical path, and this can be achieved with a change either in the refractive index (refractive devices) or the geometrical path length (reflective devices). At present, deformable mirrors (DM), which belong to the category of reflective devices, are the corrector devices most commonly used [2]. In a DM, the shape of the reflective surface is

modified by a number of actuators so that the final result is a surface that reproduces the shape of the wavefront with half of the aberrated amplitude. In this way, the difference in the optical path is summed over the incident and the reflected light. The DM design itself can be either segmented or continuous [2, 19].

1.2.2 Retinal imaging modalities in combination with adaptive optics

By definition, ophthalmoscopes always image the retinal fundus and so they operate by using the optics of the eye (cornea and crystalline lens) as the objective lens [14]. The numerical aperture NA is given by

$$NA = n \cdot \sin(\theta) = n \cdot \sin\left(\arctan\left(\frac{D}{2 \cdot f}\right)\right) \quad (1)$$

where n is the index of refraction of the media in which the light is focused, θ is half the angle of the beam focused at the sample (the retina in the case of the eye), D is the entrance pupil diameter and f is the focal length. For an ophthalmoscope, the focal length and the pupil size are determined by the anatomy of the human eye, so NA can range from 0.03 for a 1 mm pupil to 0.2 for a 7 mm pupil. The resolution R can be calculated as

$$R = \frac{\lambda}{2 \cdot NA} \quad (2)$$

where λ is the wavelength of the light used [14]. Potentially, a diffraction limited ophthalmoscope with a 7 mm dilated pupil and 550 nm light could resolve features as small as 1.3 μm thus allowing the imaging also of the smallest photoreceptors [8, 14]. However, the use of large pupil sizes also increases the effect of the aberrations introduced by the optics of the eye. This significantly reduces the resolving power of an ophthalmoscope to $\sim 5 \mu\text{m}$ at best [8], thus the need to introduce AO for the correction of the aberrations.

AO can be used in combination with different retinal imaging modalities. The first application of AO to a conventional fundus imager ophthalmo-

scope was in 1997 [18]. In a conventional fundus imager ophthalmoscope, or flood-illuminated ophthalmoscope, wavefront sensing is performed typically with a Shack-Hartmann sensor and a point light source (e.g. a SLD). The light that is scattered back from this spot is imaged onto the corrector (e.g. a DM) and is then reflected to the wavefront sensor. The system operates in closed loop until an acceptable level of correction is achieved. After the correction, the retinal imaging is performed on a large patch of the retina (i.e. ~ 1 deg) with another illumination source. The wavefront from this retinal patch is corrected and focused on a camera (e.g. CCD) [8]. The light source used for illumination is chosen to be with low spatial coherence, in order to limit the effect of speckle noise.

After flood-illuminated ophthalmoscopes, AO was subsequently implemented in SLO [22] and OCT [23]. The configuration of SLO systems is well suited for the implementation of AO. In fact, since images are acquired in a point-by-point fashion using a laser source, the same source can be used also for wavefront measurement. However, early applications of AO to SLO were limited by the complexity of the design and the reliance on partially coherent light sources [24]. Once these initial limitations were overcome with different optical design and the availability of better light sources, AOSLO systems were able to produce en face retinal images with higher contrast and resolution than any other imaging modality [14].

In contrast to the imaging systems described earlier, transverse and axial resolutions for OCT are independent, with the latter being dictated by the mean wavelength and bandwidth of the illumination source rather than the numerical aperture NA [8]. On the other hand, transverse resolution is limited by diffraction and aberrations in the same way as for flood illumination systems and SLOs. For this reason, the implementation of AO complementary and allows AO-OCT to reach both high transverse and axial resolutions [8, 21].

In the early years, the complexity of the design limited the use of AO systems outside research laboratories. In recent years AO has been made available also for commercial retinal imagers, both fundus cameras (Imagine eyes, Orsay, France) and AOSLO (Boston Micromachines, Cambridge, MA, USA; Physical Sciences, Inc., Andover, MA, USA; Canon, Inc., Tokyo, Japan [25]). Even if these cameras are a step towards wide spread application of AO retinal imaging in the clinics, they are still intended for research

use only. AO is still at the initial search for potential clinical utility, and not represented as an effective diagnostic technique, with only the fundus camera produced by Imagine eyes (the rtx1) being approved by the U.S. Food and Drug Administration.

1.2.2.1 *The rtx1 camera*

The retinal images used in this study were acquired in the G. B. Bietti Foundation for Study and Research in Ophthalmology (Rome, Italy) by Dr. Marco Lombardo and his team. The camera used for the image acquisition is the rtx1, an AO fundus camera produced by Imagine Eyes (Orsay, France, Figure 1.6) [26]. The rtx1 is a stand-alone imaging system designed to be used also by operators who are not familiar with its optical system. The image acquisition process is comparable to a standard commercial fundus camera and a full examination takes generally a few minutes per eye. For these reasons, the rtx1 is suitable for use in large-scale clinical studies.



Figure 1.6: Picture of the rtx1 camera. Reproduced from [26] with permission, copyright 2011 Society of Photo Optical Instrumentation Engineers.

The internal aberrations of the eye are measured by analysing the reflection of a 750 nm SLD point source with a Shack-Hartmann sensor (HASO 32-eye, Imagine Eyes, France). The sensor has 1280 microlenses in a 40×32 array with spacing between lenses of $110 \mu\text{m}$ and is able to measure refractive errors over a range larger than $\pm 20\text{D}$. The corrector element is a DM (mirao 52e, Imagine Eyes, France) that is placed at an image plane that is conjugated to the pupil plane of the eye. The mirror has 52 actuators and a maximum $\pm 50 \mu\text{m}$ stroke, which can correct for the optical aberrations

present in almost any eye. The AO correction is run in closed loop mode with a loop time of ~ 66 ms (15 Hz) [27].

A field of view of $\sim 5^\circ \times 4^\circ$ on the retina is uniformly illuminated by a 860 nm light-emitting diode (LED). The illumination source has a bandwidth of 35 nm at full width half maximum and as such is considered low-coherence (or short-coherence) [28]. The light that is backscattered by the retina is reflected by the DM and then imaged with a low noise CCD camera (R-CCD, Rooper Scientific, Planegg, Germany) (Figure 1.7 and Figure 1.8). Each pixel corresponds to $1.6 \mu\text{m}$ on the retina of an emmetropic eye. The theoretical transverse resolution of the system is $2 \mu\text{m}$ [29]. In each imaging session, 40 images are captured in sequence with an exposure time of 9 ms for each image. Because of the readout time of the camera, the interval between individual image recordings is 105 ms (10 Hz frame rate). Thus, the acquisition of 40 frames takes approximately 4 s. As the total amount of light on the eye of all the light sources combined is below the safety threshold for ophthalmic devices, the system is classified as a group I device (no potential hazard) under ISO 15004-2:2007.

The viewer interface of the rtx1 shows the first Purkyně images of the cornea and the placement of the entry beam. The placement of the beam inside the Purkyně images is considered as reference from the operators for collecting high-quality images of the retina. The Purkyně images are

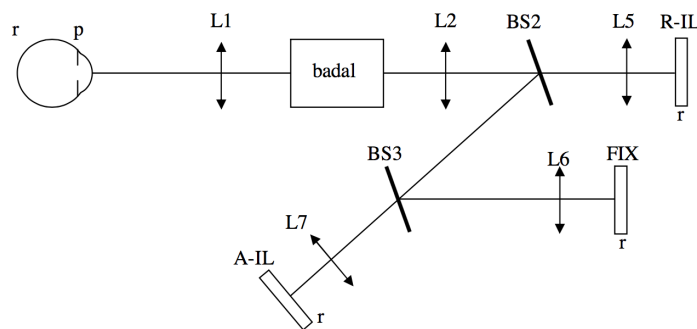


Figure 1.7: Representation of the optical illumination system of the rtx1 camera. Symbols used in the figure: r = retina and planes conjugated with the retina, p = pupil and planes conjugated with the pupil, L1-7 = lenses, badal = badal system for compensation of eye ametropia, BS2-3 = beam splitters, R-IL = retinal illumination source (860 nm LED), FIX = internal miniature monitor used as a fixation target, A-IL = analysis illumination source (750 nm SLD). Reproduced from [26] with permission, copyright 2011 Society of Photo Optical Instrumentation Engineers.

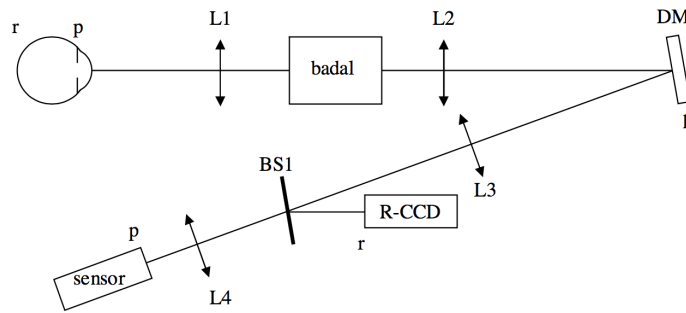


Figure 1.8: Representation of the optical imaging system of the rtx1 camera. Symbols used in the figure: r = retina and planes conjugated with the retina, p = pupil and planes conjugated with the pupil, L1-4 = lenses, badal = badal system for compensation of eye ametropia, BS1 = beam splitter, DM = deformable mirror, R-CCD = CCD camera used for imaging, sensor = wavefront sensor. Reproduced from [26] with permission, copyright 2011 Society of Photo Optical Instrumentation Engineers.

virtual images formed by the light reflected from the structure of the eye. At least four Purkyně images are usually visible, of which the first image is the reflection from the outer surface of the cornea and can be used as eye trackers to measure the position of the eye [30].

1.2.3 *Imaging retinal structures with adaptive optics*

The combination of AO with the different imaging techniques allows to image the retina at a microscopic scale, but the visualisation of the microscopic structures also requires sufficient contrast and signal-to-noise ratio. As most of the retinal layers are nearly transparent in order to let the light reach the photoreceptors at the back, their visualization can be hard to achieve [14].

Despite the poor axial resolution of AO flood illumination cameras, the imaging of different retinal layers is still possible since out-of-focus light reduces image contrast, not resolution [8]. Among the different structures of the retina, AO flood illumination imaging is especially effective in imaging the nerve fibre layer, the retinal blood vessels and the photoreceptor layer (Figure 1.9).

Ganglion cells are weakly scattering and provide low contrast. Because of this they have so far been imaged in living eyes mostly using extrinsic fluorophores [14]. As seen in OCT images the retinal pigment epithelium

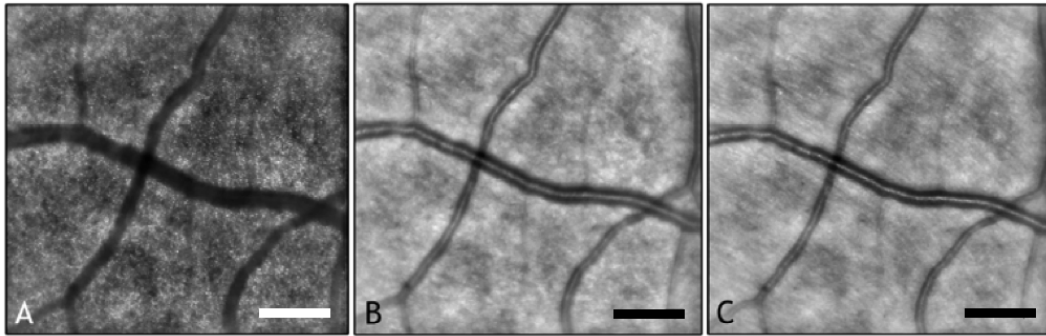


Figure 1.9: Examples of AO fundus images acquired with the rtx1 camera of the photoreceptor layer (A), vasculature (B) and nerve fibre layer (C). Scale bars represent 0.2 mm. In (A) it is possible to see the individual cone photoreceptor cells resolved and the shadows that the blood vessel project on the photoreceptor layer. In (B) the photoreceptors appear in the background and the blood vessel walls are resolved. In (C) it is possible to see the stripe pattern of the nerve fibres on top of the vasculature (reproduced from [2]).

cells are strongly backscattering. Nonetheless, the presence of the stronger scattering from the photoreceptors masks their signal, making the epithelium visible only when the photoreceptor layer is disrupted or with the use of autofluorescence. Recently, nonconfocal AOSLO methods have proven effective in imaging structures that are not normally visible with conventional cameras, such as the pigment epithelium cells in healthy retinas [31] and the blood flow in the retinal vasculature [32, 33]. In addition, nonconfocal AOSLO and OCT angiography can allow the visualisation of the individual blood cells and of the microstructure of the vasculature (e.g. vessel walls). Advancements have been made also in the field of AO-OCT, which recently allowed the imaging of ganglions [34] and retinal pigment epithelium cells [35].

Imaging retinal structures at a microscopic scale makes it possible to analyse their characteristics and possibly to detect pathological abnormalities *in vivo* [2]. It is important to note, however, that imaging can convey information about structural integrity in a way that is dependent on the specific imaging modality that is chosen. In order to be able to use a specific imaging system to determine structural function, it is necessary to understand how the system and the retinal structures interact. For example, there is a major difference between a change in backscattered light intensity observed with short-coherence or long-coherence light sources. If a light source with

short spatial coherence is used, changes in the measured brightness can be caused only by changes in the structure, the absorption rate by the tissue or the refractive index, or a combination of these factors. In the case of a long-coherence light source, changes in the signal can also be caused by interference [14]. The discrimination between short and long-coherence depends on the size of the structures, or modifications in the structures, that are the object of the observations.

Promising attempts at objective functional measurements have involved blood flow, fixation stability and eye movements. Assessment of the structural integrity (and function) of photoreceptors requires some specific considerations, which are given in the next section.

1.2.3.1 *Imaging of photoreceptors*

Photoreceptors were the first cells to be imaged in the retina *in vivo* and remain the most studied with AO imaging. Cone cells have waveguiding properties [36–38], which gives them the ability to backscatter the light very well and so be imaged with with good contrast. In AO-fundus images cones appear as a mosaic of bright dots on a dark background (Figure 1.9A) [39].

According to observations with OCT, it is believed that the main contributions to the light reflected by the cones originate from the OS tips and the inner/outer segment (IS/OS) interface (Figure 1.10). In order to observe changes in the OS length with en-face imaging, the bandwidth of the light source $\Delta\lambda$ has to be narrow enough so that the coherence length is noticeably longer than the whole OS. Round trip coherence length for a Gaussian shaped spectrum can be calculated using $L_c = (2 \ln 2 \lambda_c^2) / (n\pi\Delta\lambda)$ as in [40], where λ_c is the central wavelength of the light source and $n = 1.43$ is the refractive index of the OS [41]. Using the formula, it is possible to see that laser sources are necessary in order to achieve a L_c greater than $\sim 30 \mu\text{m}$, which is the OS length [40]. The long-coherence light of AOSLO systems has also proved able to measure cyclical changes in the OS length due to their renewal process [9]. Changes in cone reflectance have also been observed with AO fundus cameras [42]. However, the low coherence properties of the light source ($L_c = 6.37 \mu\text{m}$ for the rtx1 camera) precludes changes in the observed intensity due to interference between light from

the two ends of the OS. Thus, the cause of the observed intensity changes in AO-flood illumination images is still object of debate [10, 42].

Although these imaging modalities show impressive results, their confocal detection scheme poses a limit to the information that they can convey. One of the new non-confocal imaging modalities, the split-detector AOSLO, provides a new way to assess the integrity of the cone IS without relying on their waveguiding properties [43]. In this way, it is now possible to separate structural integrity from waveguiding function, and to examine the physiological implications if they are not both evident. Another non-confocal

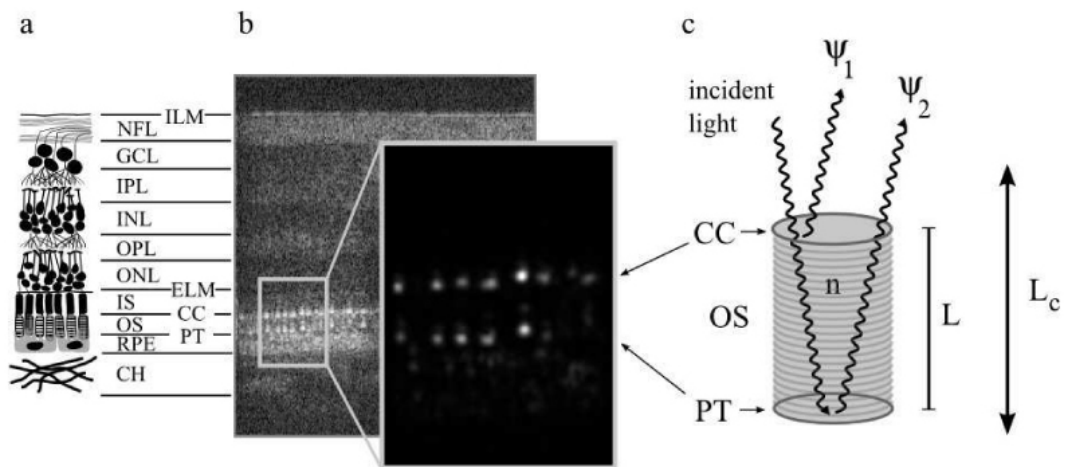


Figure 1.10: (a) A diagram of the major retinal layers, consisting of the inner limiting membrane (ILM), nerve fiber layer (NFL), ganglion cell layer (GCL), inner plexiform layer (IPL), inner nuclear layer (INL), outer plexiform layer (OPL), outer nuclear layer (ONL), external limiting membrane (ELM), the inner segments (IS) and outer segments (OS), the connecting cilia (CC) and posterior tip (PT) layers, the retinal pigment epithelium (RPE), and the choroid (CH). (b) shows a cross-section of an AO-OCT B-scan in log-intensity of the neural retinal layers corresponding to the diagram in (a). The zoomed window is an enlarged view (in linear intensity) of the cone OS, which shows clearly that most of the cone reflection originates at the IS/OS interface (or CC) and at the PT. The peak intensity of CC and PT layers is more than two orders of magnitude greater than the average intensity of all the other layers in the image. (c) shows a model for light propagation through the OS. The bright reflections originating at the interfaces (Ψ_1 and Ψ_2) can be used to observe changes in the OS length if the coherence length of the light source is longer than the OS length $L \ll L_c$. Reprinted with permission from [9]. Copyright 2010 Optical Society of America.

modality, the two-photon fluorescence imaging, is able to show the fluorophores themselves present in the cones, but is not ready for use in living human eyes yet [44].

1.2.3.2 *Assessment of the cone photoreceptor mosaic*

Up to now, most studies involving AO retinal images have focused on characterisation of the photoreceptor mosaic. It has been shown that the characteristics of the photoreceptor mosaic are strongly related to the quality of subject vision [45, 46] and in some cases to the healthiness of the eye itself [47]. Examples of pathologies that can be identified by looking at the packing of the photoreceptors are cone-rod dystrophy [48], retinitis pigmentosa [49, 50] and age related macular degeneration [51]. In order to be able to observe pathological deviations from “normality”, it is essential to characterise the photoreceptor mosaic of a healthy population. The most studied properties of the photoreceptors (particularly cones) so far are the spatial properties, in particular their spatial density.

The *in vivo* measurements of cone density have shown good agreement with histological data acquired *post mortem* [2, 11, 52]. The cone density in the region close to the fovea shows significant variability between subjects, with coefficient of variation (defined as the ratio of the standard deviation to the mean) values ranging between 12% and 20%. Some of the survey studies seem to have disagreeing results, but the differences in the density values could be due to a number of different factors, such as the age of the subjects, the characteristics of their eyes, the imaging and the analysis procedure (for a review of cone density values, see [2]).

The other aspect of the cone mosaic that has received interest is the spatial arrangement of the cones (Figure 1.11). A common assumption about the preferred cone packing arrangement, especially in the early studies, is that similarity to hexagonal packing is index of a healthy cone mosaic, as it is the most efficient sampling of a two-dimensional plane (Figure 1.11c). Using hexagonal packing as reference, studies have shown that regularity in the cone arrangement decreases with the distance from the fovea [29] and that disruption in the cone mosaic can be caused by a retinal condition [53].

The metrics that describe cone packing can be divided in two categories. The first category aims at measuring the regularity of the cone packing arrangement. The most common technique used to evaluate mosaic reg-

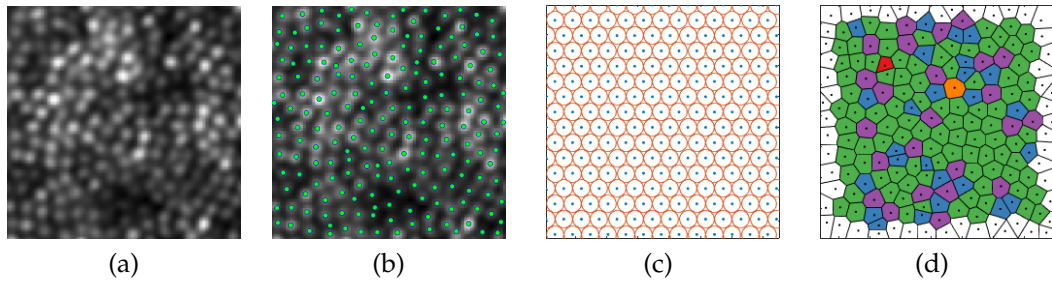


Figure 1.11: Example of analysis of the cone mosaic. A portion of the cone mosaic is selected (a), then the cone positions are marked (b). (c) shows how the cones would be positioned if they had perfect hexagonal packing. (d) shows the Voronoi diagram of the marked cones in (b). The Voronoi cells are coloured according to their number of sides (red = 4, blue = 5, green = 6, purple = 7, orange = 8)

ularity is analysis of the Voronoi diagram (Figure 1.11d). Given a set of points in a two-dimensional space, the Voronoi diagram is a division of the space in polygons according to the minimum distance between the points [54]. So far, regularity based on the Voronoi diagram has been defined as the ratio of hexagons on the total number of polygons [29, 55–57]. However, due to the high sensitivity of the number of sides of the polygons even with only slight changes in the point coordinates, some works introduced counting of the Voronoi tiles with number of sides ranging from 4 to 8 [29, 58–61]. Some disadvantages of the Voronoi approach are the required knowledge of all the cone coordinates, the high sensitivity to the cone positions and to the size of the area selected for analysis. Other approaches to the measurement of packing regularity that do not require knowledge of the cone coordinates are based on the spatial frequency content, such as the autocorrelogram [62] and the Fourier power spectrum [47].

The second category of metrics describes the spacing between cones. The most intuitive way to evaluate cone spacing is to calculate the nearest neighbour distance for each cone and then average the values over the sample area [63]. There have been numerous suggestions for alternative spacing metrics, ranging from deduction from cone density under the assumption of an hexagonal lattice [2, 64] to the use of autocorrelograms [62, 65, 66]. The constant search for spacing metrics is mostly driven by the necessity to find metrics that are the most efficient at early detection of pathological changes in the cone mosaic, as well as to characterise different modalities of

cone mosaic disruption. For this reason, there are studies that have focused on evaluation of the behaviour of spacing metrics with varying severity of cone loss [53, 67].

In addition to cone spacing properties, recent studies have also started to focus on the intensity of the light reflected by the photoreceptors [9, 10, 37, 40, 42, 68–71]. Individual cones imaged in the living retina show significant changes in their brightness, both spatially and temporally, and the changes are present in healthy subjects as well as in diseased eyes. Another property of the cones that can be retrieved from their brightness is their directional tuning, known as the Stiles-Crawford effect [41, 72]. This measurement can be carried out by imaging the cone mosaic varying the entry position of the light beam in the pupil plane of the eye, which results in different incidence angles of the light beam in respect to the cones [73–75]. Due to the more recent nature of the study of cone reflectance, metrics that are able to describe its properties are only starting to be introduced, and are not as developed as the spatial properties.

The inter-subject variability in the cone mosaic parameters, both in the spatial and in the reflectance metrics, confirms the importance of thoroughly studying the features of healthy eyes, in order to determine if deviations in collected data can be ascribed to a retinal condition. The processing techniques used on the photoreceptor images are briefly reviewed in Section 1.4.

1.3 CLINICAL APPLICATIONS OF ADAPTIVE OPTICS RETINAL IMAGING

Because of its high resolution, AO retinal imaging has already been used for the characterisation of a number of eye diseases at different stages. As most retinal degenerations have in general a slow progression, it is believed that the onset of the disease occurs years before the deterioration of visual function [2]. The possibility to image the retina at high spatial resolution given by AO systems has a great potential for clinical applications, as it may provide a way for early identification of retinal pathologies as well as a way to monitor the efficacy of treatments at a cellular level. The impact of AO imaging on ophthalmology is growing in importance, as demonstrated by the increasing number of publications [14].

AO systems can be used to image the same portion of the retina over time, allowing longitudinal tracking of individual cells [76]. Longitudinal analysis is an essential step in the evaluation of disease progression and response to an experimental treatment, which naturally leads to the introduction of AO imaging as a powerful tool for clinical trials. Currently, only one study has been published reporting this application of an AO system [77] but there are at least three ongoing clinical trials that involve the use of AO technology [14].

Microscopic AO imaging can also contribute to the identification of diseases that can benefit the most from early treatment, as well as the choice of the most suitable patients to undergo treatment. For example, the combination of split-detector AOSLO imaging and confocal AOSLO imaging can reveal the presence of cones with intact OS but no or little reflectance properties [43]. Cones with such characteristics would be the best candidates for the recovery of function, as their structure is still present, such as in the case of the rare genetic condition achromatopsia [76, 78].

1.3.1 *Adaptive optics imaging of retinal pathologies*

The major causes of vision loss in the developed world are diabetic retinopathy, age-related macular degeneration and glaucoma. Because of the relatively low resolution of retinal imaging techniques currently used in the clinics to detect abnormalities of the retinal microstructures and the relatively poor sensitivity of functional testing, diagnosis for these retinal conditions usually occurs once the retinal structures are already heavily compromised. Early diagnosis could lead to early treatment that could possibly prevent further deterioration of vision, if not even revert it [2]. AO imaging can also provide new insights into the mechanism of disease progression by monitoring the microscopic alterations in the different structures of the retina, as well as help to decide on approaches for treatment.

Glaucoma is the main cause of irreversible blindness in the world that can be prevented [79]. Glaucoma is a neuropathy that acts on the retina by damaging the ganglion cells and the axons. As a consequence, the nerve fibre layer becomes progressively thinner, locally or diffusively. The loss of axonal tissue is thought to be the first detectable sign of glaucoma, before changes in the optic nerve head and the onset of visual functionality

loss [80]. The contribution of AO to the early detection of changes in the nerve fibers is important, as it makes it possible to resolve individual nerve fibre bundles, both with fundus imaging [81] and OCT [82].

Age-related macular degeneration (AMD) is the leading cause of vision loss in the elderly across the developed world. AMD is a multifactorial disease and involves ocular, systemic and genetic risk factors [83]. There are two forms of AMD, “dry” and “wet”. In both the AMD forms the early stages are asymptomatic but they both present formation of drusen, that are insoluble extracellular aggregates, in the retina. In the late stages, dry AMD presents degeneration of retinal pigment epithelium cells and of the overlying photoreceptors, while wet AMD acts on the circulation, with the growth of new blood vessels toward the outer retina and leakage of fluid [84]. The injection of a fluorescent dye agent (fluorescein angiography) allows identification and classification of the leakages. SD-OCT is used instead to image the structure of the new blood vessels, but the characterization of these structures has to be improved to obtain reliable results. AO fundus imaging, in combination with AO-SD-OCT, could be used to monitor the presence and evolution of drusen in the early stages and to analyze their effects on the photoreceptors and pigment epithelium cells [85]. In this way, patients that present a faster progress of the disease may be identified and followed more effectively.

Our work focused on the effects of diabetic retinopathy on the cone photoreceptors. For this reason, the next section offers a more thorough description of this retinopathy.

1.3.1.1 *Diabetic retinopathy*

Diabetic retinopathy (DR) is a frequently occurring complication of diabetes mellitus (type 1 diabetes). Diabetes causes chronic hyperglycemia that acts on the retinal circulation by damaging the blood vessel walls and producing pathological changes in the vascular structures [86–88]. According to the Early Treatment Diabetic Study severity scale [89, 90], DR can be divided into proliferative or non-proliferative (NPDR), which can be further classified as mild, moderate and severe (Figure 1.12).

As DR causes important changes in the retinal microvasculature, the most commonly accepted theory was to consider that the changes produced in other retinal layers are a consequence of the vascular changes.

However, in recent years another theory, known as the “neurodegenerative theory”, emerged. According to this theory, DR is not a microvascular but rather a multifactorial disease that also involves the retinal neuronal cells early in the course of disease onset and progression [92–98]. The neurodegenerative changes include apoptosis of several populations of retinal cells, such as photoreceptors, bipolar cells, ganglion cells, and astrocytes. Structural and functional impairments of the neural tissue have also been supposed to contribute to the earliest alterations of the vascular structures [99–101]. Some recent studies have observed modifications in the cone photoreceptor mosaic in subjects with type 1 diabetes, even before any signs of DR were evident [102–104]. Such modifications included a reduced cone density and a decreased regularity in the cone spatial arrangement, which seem to imply at least a disruption in the cone reflectance properties, or even the death of the photoreceptor cells. The question of whether the damage in the photoreceptor layer is first caused by the neuronal or vascular side of the disease is still the subject of debate.

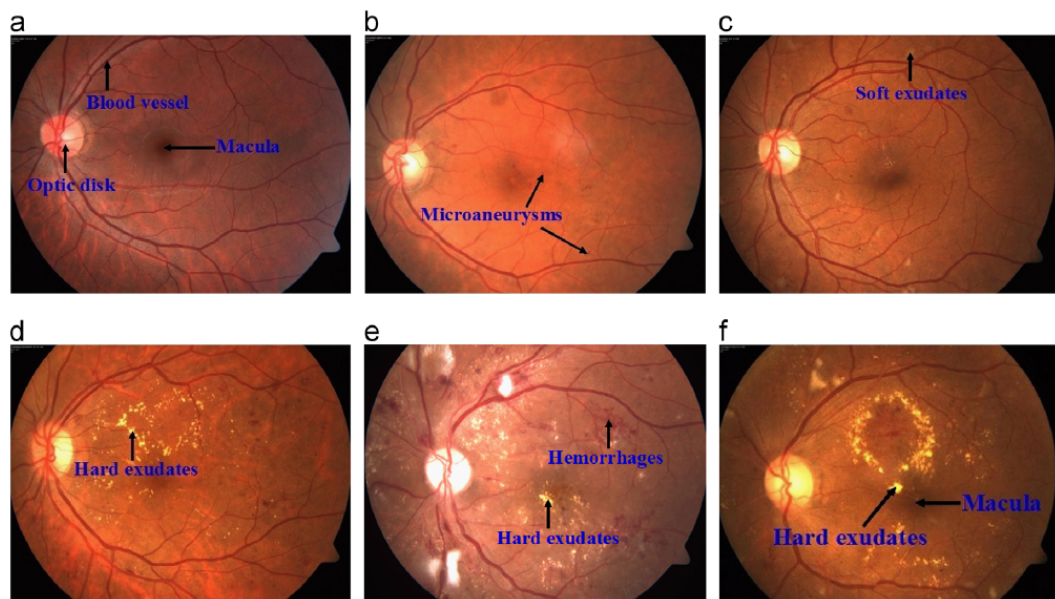


Figure 1.12: Typical fundus images that show increasing severity of retinal damage associated with diabetes. (a) Normal retina, (b) retina with mild NPDR, (c) moderate NPDR, (d) severe NPDR, (e) proliferative DR, (f) macular edema. Reprinted from [91], copyright 2013, with permission from Elsevier.

With fluorescein angiography it is possible to determine the amount of leakage that occurs in the retinal circulation [16, 105, 106]. However, this technique is not always desirable, as the agent could affect the circulation and lead to complications. Non-invasive imaging techniques include fundus imaging, SD-OCT and OCT angiography, which with the implementation of AO are able to detect early retinal changes caused by diabetic retinopathy (such as microaneurysms, micro-haemorrhages, photoreceptor mosaic modifications) and abnormalities in the capillary network (such as the weakening of the blood vessel barriers and the growth of new blood vessels). For example, with the use of confocal AOSLO with motion contrast it is possible to perform structural and functional analysis of the microvasculature near the fovea, which in patients with diabetes showed a higher degree of tortuosity even without signs of DR [107]. AO-SD-OCT and AO-OCT angiography can also be used to image the capillaries, with the advantage that it is possible to create a 3D reconstruction of the capillary network [12, 108] (an optimal approach could involve complementary observations of the retinal vasculature, both en-face and axially.)

1.4 RETINAL IMAGE PROCESSING

Before the advent of image processing techniques for the study of biomedical images, the analysis was carried out entirely manually by experts. The first method for the analysis of retinal images to be published regarded the segmentation of retinal blood vessels on fluorescein angiograms [109] and, as with subsequent works, was based on digitized slides. The first method that detected and characterized abnormalities in the retina was presented in 1983 and it aimed to detect microaneurysms [110]. The field of retinal image processing changed drastically with the advent of digital retinal imaging in the 1990s, together with the increased development of digital image analysis techniques [12].

With AO imaging systems the information content available in retinal images has greatly increased. Along with this, in recent years AO has been made available for commercial retinal cameras, which are ultimately aimed at use in clinics, and so it is now becoming urgent to develop image analysis tools that reduce the human contribution as much as possible, in order not

only to spare the time of the clinicians, but also to overcome the subjectivity inherent in human observation.

Before clinical analysis can be performed, retinal images (and biomedical images in general) usually require computational processing. The processing operations that can be carried out on digital images can be divided in three main categories, namely restoration, enhancement and segmentation [111]. If more than one image is available, then image registration can also be added to the processing operations. For the purpose of this thesis, we will refer to image restoration, enhancement and registration as “pre-processing” steps, that is to say that these operations need to be performed before the analysis that addresses the specific structures of the image (and that are going to be used for image interpretation).

1.4.1 *Image pre-processing*

Image restoration aims to correct for deterioration due to known causes. Operations in this category include noise removal [112] and removal of residual aberrations through deconvolution [112, 113]. Motion is also a known cause of deterioration. As an example, as AOSLO images are acquired point-by-point the motion of the eye introduces distortions in the final video that have to be corrected for in order to produce results that can be analysed [114]. Another important operation that falls into this category is shading correction for global intensity uniformity [115]. Uniformity in the global intensity of the image can be compromised by many factors, such as imperfections in the image formation process, non-uniform illumination, uneven spatial sensitivity of the sensor or imperfections in the camera optics (Figure 1.13) [116].

Image enhancement involves the improvement of an image in order to make it more suitable for subsequent use, which can be either further computational processing or visual examination. Examples of image enhancement include operations on the image histogram [111] and filtering in the spatial and frequency domain [112]. Image quality can be determined through a number of different metrics, which can be chosen according to the image content. In general, for the purpose of retinal image processing an image is said to have “good quality” if features of interest such as photoreceptors, blood vessels and nerve fibers: (i) are resolved (i.e. two adjacent

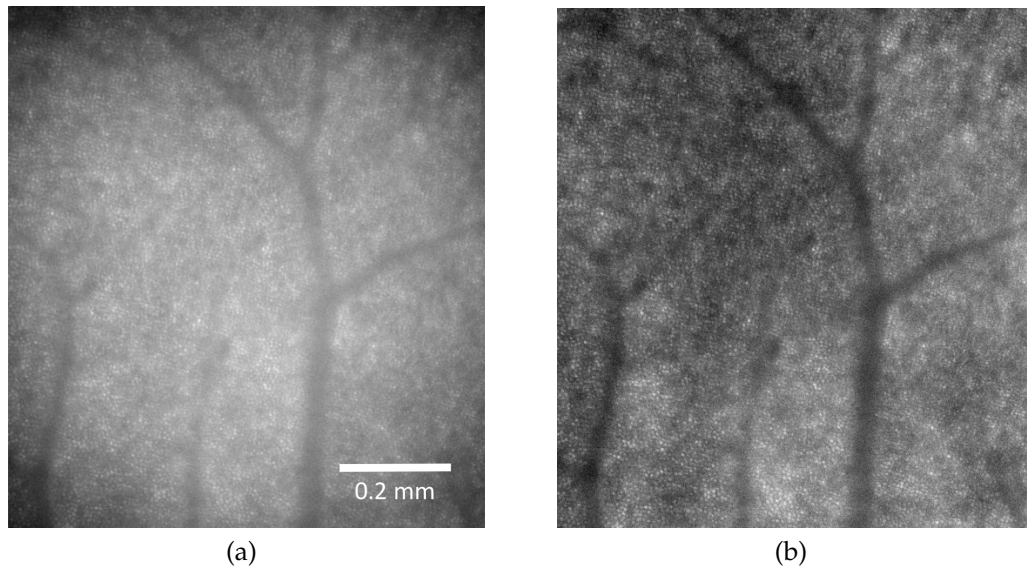


Figure 1.13: Example of flat-field correction for a $2.3^\circ \times 2.6^\circ$ ($0.70 \text{ mm} \times 0.78 \text{ mm}$) photoreceptor layer image acquired with the rtx1 camera. It is possible to see that the brightness of the image decreases towards the edges in (a) while the overall brightness profile is more uniform in (b)

structures can be visualized as separate by the imaging system), (ii) have high contrast (i.e. their difference in luminance and/or color makes them distinguishable), (iii) have high signal-to-noise (SNR) ratio (i.e. the power of the signal strength is greater than the power of the background noise) [14].

Image registration is the process of alignment of two or more images of the same scene. Misalignment can be caused by different camera angles or field of view, or by the use of different image modalities. The alignment can be performed in different ways, such as through the identification of common landmarks (feature based) or through the calculation of metrics from the image grey values (intensity based) [111]. Applications of image registration include image mosaicing to create wide-field montages, comparison of images acquired with different modalities or comparison of images acquired at different times. Registration of images of the same object acquired with a short time difference can be performed in order to average them and produce images with higher SNR.

1.4.2 *Ramaswamy's PhD thesis*

The application of these three topics to AO fundus images of the photoreceptor layer and of the nerve fibre layer were addressed in depth in the PhD thesis of Gomathy Ramaswamy [117]. Using images acquired with the rtx1 camera from Imagine Eyes, Ramaswamy explored different aspects of pre-processing concerning short exposure frames of the photoreceptor layer, which are of special importance when dealing with images with such high resolution.

First different methods for the correction of uneven illumination were analysed, such as subtracting or dividing by the average filtered image, homomorphic filtering and a wavelet based approach. The background-corrected images were then evaluated to measure the image quality using various parameters, including sharpness, variance, power spectrum kurtosis and contrast. A percentage of the frames with the best image quality can then be selected for registration, which was carried out in two stages. First a coarse registration was performed using cross-correlation. Secondly fine registration was performed investigating different approaches, such as parabolic interpolation on the peak of the cross-correlation, maximum-likelihood estimation and tracking of a selection of cones on the images (Figure 1.14). Fine registration allowed to correct for minor rotations present in the frame sequences. It was found that two-stage image registration including correcting for rotation significantly improves the final image contrast and sharpness.

1.4.3 *Analysis and interpretation*

After the preliminary corrections aimed at improving image contrast and SNR, further analysis can be carried out aimed at the interpretation of the structures in the image, such as segmentation of regions of interest or texture analysis. In the case of retinal images, the analysis can be divided in two main categories: (i) locate and segment the retinal features and (ii) detect the presence of abnormalities and lesions. The field of retinal image analysis is broad, as the retina includes many features that can be imaged with many different imaging modalities. For example, in the case of traditional wide-field fundus images the main directions of analysis include

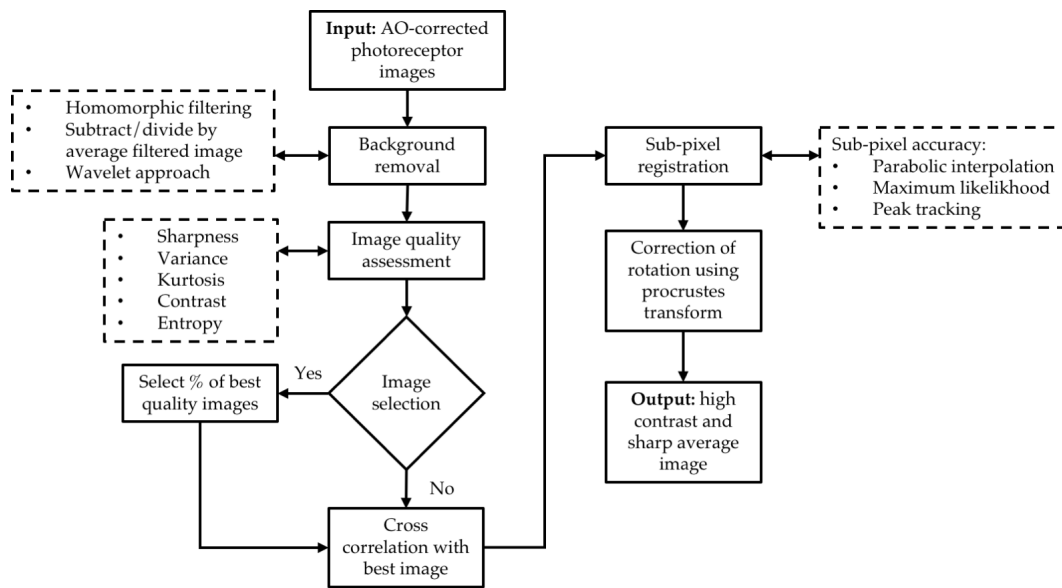


Figure 1.14: Flow diagram of image registration process developed for AO cone images by Ramaswamy [117, 118].

the identification of the optic nerve head, localization of the fovea and vasculature mapping [12]. On the same type of images, there are also many types of detectable abnormalities that are related to the vasculature (hemorrhages, microaneurysms, neovascularization, nerve fiber infarcts), the pigment epithelium (drusens, hyper/hypo-pigmentation) and the choroid (nevus, melanoma, uveitis related) [12].

The analysis of AO images necessarily poses new challenges on the image processing side. The amount of detail that these images provide requires also appropriate techniques that are able to deal with such volume of information. Particular attention has been dedicated to the development of automated image analysis tools, so that the information can be efficiently retrieved in a reasonable amount of time without being too labour-intensive for the clinicians and to have the possibility to increase the number of patients and images for more statistically significant results [14, 55].

For these reasons, the field of automated retinal image analysis has seen a fast development in recent years. Initially used for the detection or measurement of retinal features on small sets of data, the efforts are now going in the direction of generating measurements that can be significant for clinical and public health, and so requiring larger sets of test data [119]. Automated algorithms are currently used for the main purposes of screening large sets to identify the patients that need to be referred for further clinical

analysis, computer-assisted diagnosis to detect the presence or likelihood of a disease from specific signs and determination of biomarkers that are linked significantly with specific conditions. Three further areas that would benefit from the development of reliable automated algorithms for retinal analysis are longitudinal analysis, computer-aided surgery and telehealth, which would be of special importance for less developed countries. In contrast with a push for a more wide-spread use of automated algorithms, the methods for the validation of the algorithms are still neither uniform nor widely agreed upon. Issues include how to deal with the variability of expert annotations, the availability of public large “real-life” datasets for testing and the accepted definition of reference (gold) standards. For a more thorough overview of automated retinal fundus image analysis algorithms and their challenges, see the review by Trucco et al. [119].

1.4.3.1 *Photoreceptor detection*

The importance of using AO for the early diagnosis of retinal conditions on the photoreceptor layer relies on the possibility to image single photoreceptor cells in tissues *in vivo*. In addition, the most commonly used descriptive metrics of the cone mosaic (described in Section 1.2.3.2) require the localization of the individual cones in the image [53, 67].

In order to identify the photoreceptor number and locations in an image, the first method used was manual labelling, where an expert visually analyses the image and chooses the coordinates of every feature believed to be a cone (or a rod, if the resolution of the system allows to resolve them) [120]. This method is still considered by many as the most reliable reference [63]. However, this approach is not desirable if the amount of data is large (e.g. with AO fundus images covering $4 \text{ deg} \times 4 \text{ deg}$ on the retina), as it is generally time-consuming, especially in patients suffering from retinal diseases. Moreover, the quality of the images is not always good enough for visual analysis, and the clinicians need to further process them in order to enhance their quality [121].

1.4.3.2 *Blood vessel segmentation*

The detection of the retinal vessels has been the subject of many studies, even prior to the advent of AO retinal imaging, as the vessels are easily resolvable with traditional imaging systems. The segmentation of the blood

vessels in the retina has more than one application, as it can be used to (i) map the retina and register different images, (ii) detect circulation diseases (e.g. Alzheimer's disease or retinal pathologies that affect circulation, (iii) subtract the vessel profiles from nerve fibre layer images [122].

There are currently many different approaches to the retinal vessel segmentation, all developed for wide field retinal images (for a review, see [123]). However, it is to be noted that the profiles of the blood vessels, or to be precise their projected shadows, have their importance also in the analysis of the photoreceptor layer, in the sense that the area occupied by them is usually excluded from further analysis. This is done because the cones obscured by the largest retinal vessels, which produce visible shadows, are not imaged with the same efficiency as the surrounding cones, making their detection more difficult and unreliable. In order to prevent unreliable estimation of the cone mosaic properties, sample areas are usually selected manually in regions devoid of vessels.

To the best of our knowledge, there are currently no algorithms that have been developed with the specific purpose of segmenting the retinal vessel shadows on AO images of the photoreceptor layer, which present different characteristics than the low-resolution wide field images. We want to point out that, since the retina is one of the most perfused tissues, the exclusion of all areas with vessels would probably result in a residual area of less than 10% of the imaged area. For this reason, we are interested in limiting our segmentation approach only to the vessels that compromise the photoreceptor layer analysis.

1.5 AIMS AND OBJECTIVES

Although the imaging of retinal structures with AO cameras has now been practiced for over a decade, its application to the clinical environment is still to be reached. In order to be able to monitor a large number of subjects and track their progress over time, we believe that it is important to move towards a decrease of the manual intervention in the analysis process. Only in this way the amount of information provided by AO cameras can be considered to give a real advantage over the traditional ophthalmic instrumentation currently used in clinical environments.

The study of photoreceptor images is the most established branch of AO fundus retinal imaging. The spatial distribution of the cones in healthy and in diseased subjects has received most of the attention, while the investigation of the properties of cone reflectance in diseased eyes is still limited. Further studies could help to determine if the reflectance of the cones could be considered as a feature that is complementary to their spatial distribution in the early detection of retinal abnormalities, or provide useful insight into the physiology or pathophysiology of the photoreceptors.

The aims of this work can be divided into two main branches. First, we wanted to perform automated processing of cone photoreceptor images without manual supervision. This step was essential to proceed to the analysis of a considerable amount of images of the same subjects over time and obtain more significant results. Second, we aimed at testing a practical application of the processing method to investigate the reflectance properties of the cone mosaic in healthy subjects and in subjects with DR, as well as over time. The techniques developed in the first part were essential for the implementation of the second part.

The objectives of this study can be summarised as follows:

- To study and assess the reliability of automated cone detection algorithms
- To develop an automated processing method that allows the analysis of the same cone mosaic imaged at different times
- To analyse the reflectance properties of the cone mosaic of a healthy subject over long time scales
- To compare the reflectance properties of the cone mosaic of healthy and DR subjects
- To investigate reflectance parameters as biomarkers for possible detection of early changes in the cone photoreceptors of diabetic subjects

The pursuit of these objectives is presented here in three articles that have been accepted for publication in three peer reviewed journals (Journal of the Optical Society of America A, Biomedical Optics Express and Investigative Ophthalmology & Visual Science) and in one short article that was published in the proceedings of the Irish Machine Vision and Image Processing conference.

PAPER I

Mariotti, L. & Devaney, N.

Performance analysis of cone detection algorithms

Journal of the Optical Society of America A, 32, 497-506 (2015)

2.1 CONTRIBUTIONS

The work presented in this thesis was conceived as a continuation to the PhD project from Gomathy Ramaswamy, “Pre-processing, Registration and Quality Assessment of Adaptive Optics Assisted Retinal Images” [117]. The majority of her project was devoted to the processing of AO short exposure frames of the photoreceptor mosaic in order to produce good quality images, so we decided to focus first on the detection of cone photoreceptor cells on these final images.

By reviewing the literature, it was clear that there was already a number of algorithms developed with the purpose of automated cone detection. Instead of developing a new algorithm, we decided to focus on the quantitative evaluation of the reliability of the available algorithms that were largely used in the research community. We also decided to include an algorithm used in astronomy for the detection of stars in crowded fields, to see if a different approach could produce interesting results. The main innovations that I introduced for this purpose were the development of a custom method for the simulation of realistic cone mosaic images and the use of the Free-response Receiver Operating Characteristic (FROC) curve for the evaluation of the detection performance. In order to have a complete approach to the performance analysis, I quantified the accuracy of different metrics of the cone mosaic also in the presence of increasing deterioration on the images.

The results of the comparison of the algorithms were submitted to the *Journal of the Optical Society of America A* and accepted for publication.

Performance analysis of cone detection algorithms

Letizia Mariotti and Nicholas Devaney*

Applied Optics Group, School of Physics, National University of Ireland, Galway, Ireland

*Corresponding author: nicholas.devaney@nuigalway.ie

Received October 9, 2014; revised January 22, 2015; accepted February 1, 2015;
posted February 4, 2015 (Doc. ID 224577); published March 4, 2015

Many algorithms have been proposed to help clinicians evaluate cone density and spacing, as these may be related to the onset of retinal diseases. However, there has been no rigorous comparison of the performance of these algorithms. In addition, the performance of such algorithms is typically determined by comparison with human observers. Here we propose a technique to simulate realistic images of the cone mosaic. We use the simulated images to test the performance of three popular cone detection algorithms, and we introduce an algorithm which is used by astronomers to detect stars in astronomical images. We use Free Response Operating Characteristic (FROC) curves to evaluate and compare the performance of the four algorithms. This allows us to optimize the performance of each algorithm. We observe that performance is significantly enhanced by up-sampling the images. We investigate the effect of noise and image quality on cone mosaic parameters estimated using the different algorithms, finding that the estimated regularity is the most sensitive parameter. © 2015 Optical Society of America

OCIS codes: (100.0100) Image processing; (170.4470) Ophthalmology; (010.1080) Active or adaptive optics.
<http://dx.doi.org/10.1364/JOSAA.32.000497>

1. INTRODUCTION

Thanks to the advent of Adaptive Optics (AO) in the field of retinal imaging [1] (for a review see [2]), it has been possible for clinicians to detect and resolve individual cells in the retina *in vivo*, while previously this was possible only for tissues examined postmortem. The great advancement produced by the use of AO makes the early detection of retinal diseases and their followup, as well as their early treatment, a real possibility [3].

One important application of AO is the imaging of the photoreceptor mosaic, which is made up of cone and rod cells. It has been shown that the quality of a subject's vision is strongly related to the characteristics of the photoreceptor mosaic [4–6]. With images that have individual photoreceptors resolved, it is possible to determine features such as the cell spatial distribution and density. To identify the photoreceptor number and locations in an image, the first method used is the manual labelling, where an expert visually analyzes the image and chooses the coordinates of every feature believed to be a cone or a rod [7]. This method is still considered by many as the most reliable reference [8]. However, this approach is not desirable if the amount of data is large, as it is generally time and labor consuming, especially in patients suffering from retinal diseases. Moreover, the quality of the images is not always good enough for visual analysis, and the clinicians need to process them further to enhance their quality [9]. Automatic tools for the detection of cones and rods are necessary to spare time and work for the clinicians, and to have the possibility to increase the number of patients and images for more statistically significant results [10].

Several algorithms for cone detection and counting have been described [10–16]. As mentioned, the performance of detection methods has always been estimated by comparing with manual labelling operated by an expert or by the authors themselves. In some cases [10,11], the results of the detections

are also compared with histological data [17] to verify that there is a general agreement. Even if reliable, the manual counting results can vary because of the personal sensitivity of the observer, so observations by more than one physician may be needed to increase the reliability of the reference data [18]. We are not aware of any systematic study and comparison of the performances of the algorithms presented so far. To move toward a truly automated cone detection process, we believe that the algorithms should be tested to know the margins of their reliability when they are run in automated mode, i.e., without further manual corrections.

In this study, we propose to use synthetic cone images based on a real cone image to compare the performance of different cone detection codes. The simulation process has the advantage of having objective reference data to use as “ground truth”. In this way, the reference data does not depend on the sensitivity of an observer and the amount of data that can be analyzed is greatly increased, leading to more statistically significant results. In our performance analysis, we consider not only the number of cones, but also the accuracy of the parameters retrieved from the detections other than the cone density, such as the regularity of the packing and the distance between the cones.

2. TECHNIQUES

In recent years, many algorithms have been proposed to automate the detection of photoreceptor cells. The first cone counting algorithms, and still the most used so far, with some enhancements by users, are those developed by Li and Roorda [10] and by Xue *et al.* [11].

The Li and Roorda algorithm is based on the detection of local maxima in the image. The first step is to filter the image using a Gaussian low-pass filter, with the aim of removing high-frequency noise. The standard deviation of the Gaussian filter is set to 1 μm , which is half of the minimum possible cone

separation (i.e., the mean nearest neighbor distance of the cones in the central fovea [17]). After the filtering, the local maxima are found using the *imregionalmax* built-in function of Matlab (Mathworks, Inc). In the last step, if two or more maxima are closer than the minimum cone separation, their centroids are taken as the final location.

Xue *et al.* base their detection technique on an image histogram analysis. After applying a background subtraction, the image is divided in intensity ranges. Starting from the highest range, the algorithm searches the connected regions of pixels with intensity values which are in the range. The centroids of the connected regions are defined as the cone coordinates and, if two or more coordinates occur closer than the minimum cone separation, their centroids are taken as the final location. A portion of the image with a size set by the user and surrounding each detected cone is excluded from later detection. This process is repeated for each intensity range, from the highest to the lowest.

Chiu *et al.* [12] recently proposed another algorithm. It starts by taking the local maxima as the initial cone detections. A portion of the image surrounding each cone is transformed from the Cartesian domain using the *quasi-polar transform*, developed by the authors in a previous work [19]. The resulting layered structures are segmented using graph theory and dynamic programming, and then the segmentation boundaries are transformed back in the Cartesian domain. This process is iterated for all cones starting from the brightest values and excluding pixels belonging to other cones or segmentations. The entire process is repeated after deblurring the image using maximum likelihood blind deconvolution. The centroids of the segmented areas are the cone coordinates.

Some of the algorithms proposed later used correlation with a cone shape defined by the user [13], content-adaptive filtering to emphasize cell structure [14] and watershed by immersion for improved computational efficiency [15]. Another way to measure the photoreceptor spatial density is to look at the image power spectrum and extract the features that correspond to the cell packing [16], but in this way it is not possible to retrieve the position of the individual cells. The presently proposed algorithms vary both in the degree of automation (i.e., the number of parameters that have to be set by the user) and in the performance of detection.

Among the cone detection algorithms, we chose to test only the algorithms of Li and Roorda, Xue *et al.* and Chiu *et al.*, as they are the most commonly used and their approaches are radically different. To do that, we wrote the codes for the three algorithms according to the descriptions given in the original works. We also evaluated algorithms developed in other image processing fields that could be used for the purpose of cone counting. We initially tested two algorithms for feature extraction—the Harris and Stephen corner detection method [20] and the Scale Invariant Feature Transform [21]. These two methods proved to be unsuitable for our task, as the average cone shape is generally not sharp enough to be considered a corner and the algorithms detect both local maxima and local minima.

We tested instead an algorithm used in astronomy for the detection of stars in crowded fields. We used IRAF/DAOPHOT, a package for stellar photometry available within the IRAF data reduction and analysis environment for

astronomy [22] and, in particular, the utility task that searches for point sources, *daofind*. The *daofind* algorithm first convolves the input image with a Gaussian function having a user-defined width; at each pixel this gives the amplitude of the least square best-fitting Gaussian. It then searches for local maxima in the convolved image whose amplitudes are greater than a detection threshold set by the user. The centers of these local maxima are the cone coordinates.

The final choice of these four algorithms is due to the following reasons; the Li and Roorda algorithm is simple and can in principle be used without changes for the analysis of images with different cone separation. On the other hand, it may miss detections in regions with low contrast (and typically low brightness) or densely packed cones. Xue *et al.* has the advantage that it detects cones at all intensity levels of the image, but if the deletion step is not done properly it may cause false detections. Chiu *et al.* is completely automated and does not require in principle the tuning of its parameters, but its main drawback is the computational complexity and the time required to run it. DAOPHOT uses convolution, which is computationally expensive, but compared to the other algorithms it should not have a preference for the bright cones over the dim ones. Moreover, the coordinates are calculated with sub-pixel precision, and this could benefit the study of the cone arrangement.

3. METHOD

The retinal images used in this study were acquired using a commercial AO-assisted fundus imager, the rtx1 from Imagine Eyes [23]. The pixel size on the retina is approximately 1.5 μm for an emmetropic eye. We focused on our available images where the cones are best resolved by the imager, in particular images acquired at 2.5 degrees temporal from the foveal center.

We used as reference a 16-bit image of a healthy eye obtained from a series of 40 images that were processed for uneven illumination and registered with the procedure presented by Ramaswamy and Devaney [24]. We selected a portion of 256 \times 256 pixels in the center of the registered image without blood vessels, to be considered as our reference for the simulation of a cone image.

We believe that, to have a more realistic simulation, the cone shapes should account for non-integer centering. For this purpose, during the simulation process, we used an image size three times bigger than the final size (768 \times 768 pixels). In this way, the pixel sampling is increased from 1.5 to 0.5 μm , and the cone centers in the final images are located on a grid that is three times finer than the pixel grid.

To simulate the cone packing, we started with a hexagonal grid of points, to which normally distributed random displacements are added. The Nyquist limit for a hexagonal array is $(\sqrt{3}d)^{-1}$ along one axis and $(2d)^{-1}$ along the other, where d is the separation between the points. We note that hexagonal sampling of the retina would be more efficient than rectangular sampling [25]. The cones are first simulated as uniform discs. Based on a visual comparison with the reference image, the disc radius is set equal to a quarter of the mean cone separation. This relation will depend on the distance from the fovea of the simulated image. Any discs that overlap are merged, and their centroids taken as the new cone coordinate [Figs. 1(a)–1(b)].

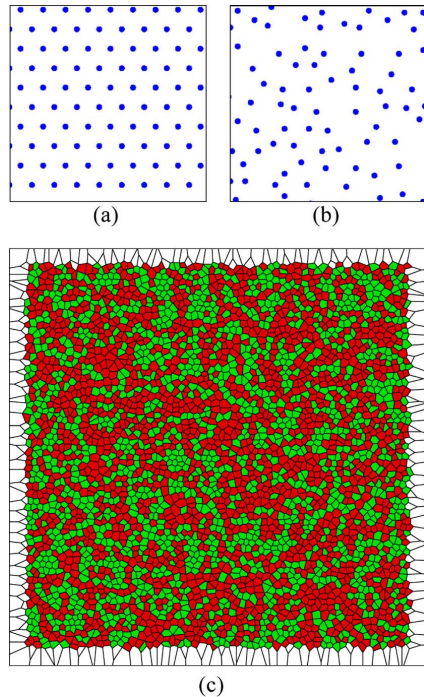


Fig. 1. Detail of the grid of points with (a) hexagonal arrangement and (b) the same grid after the process of coordinate definition. (c) The Voronoi diagram of the final arrangement of one of the simulated images. The diagram shows in light gray (green online) the cells with six sides, while all the other cells are gray (red online).

The regularity of the resulting packing is determined by Voronoi analysis and is defined as the percentage of hexagonal cells [10]. The standard deviation of the random displacements can be chosen to reproduce the desired packing regularity: a bigger standard deviation will result in a lower percentage of hexagonal cells and, thus, in a poorer regularity of the mosaic. A consequence of the merging of points is that the final density is different from the initial one, so its value

has to be calculated again. Cells at image boundaries are excluded from this and all subsequent analyses [Fig. 1(c)].

We tuned our simulation so that the final density is compatible with the values provided by Curcio [17], and the regularity of the mosaic has a value compatible with that found by Li and Roorda [10], and Park *et al.* [26]. The synthetic cone images present a mean cone density of 25,734 cones/mm² and a mean percentage of hexagonal cells of 46.31%, ranging from 45.13% to 48.10%. The mean nearest neighbor distance, NND, has a mean value of 4.79 μm (Table 1).

Before using the described method, the first attempt at the simulation of the cone coordinates was made using a normal distribution truncated at a quarter of the mean cone separation for the displacements, to avoid overlap of the cone discs. However, even though many values of the standard deviation of the distribution were tested, the regularity of the final mosaic was always much higher than the observed values. For this reason, we changed the approach and used the merging of the cone discs instead. This agrees with results from previous studies that suggest how the cone mosaic cannot be reproduced only by adding random deviations to a continuous hexagonal pattern [27]. In general, cones seem to have a preferred arrangement that varies with the distance from the fovea, but the factors involved in the mosaic arrangement are not fully understood.

To assign the cone intensities, we used as a starting point a smoothed version of the reference image, to reproduce the low-frequency brightness variation in the background and in the cones. The intensities were defined as values normally distributed around the values of the smoothed reference image at the cone positions. The standard deviation is chosen by comparing the histogram of cone brightness to that of the reference image (obtained by the Li and Roorda algorithm).

Once the coordinates and the intensities of the cones are defined, the synthetic image was obtained by summing two images which we refer to as “peaks” and “background” images. The peaks image was obtained by placing circles at the cone positions with intensities obtained as described above and a radius equal to a quarter of the mean cone separation, and then blurring them with a Gaussian filter, as done also in previous works [11], with a standard deviation equal to 0.75 times the radius of the circles. It is to be noted that, even if upsized by a factor 3, the sampling of the reference image is still too poor to reproduce a good disc shape. As background

Table 1. Parameters of the Series of Simulated Images, with Their Mean and Standard Deviation in the Last Row^a

Image	Cone Density (cones/mm ²)	Number of Cones (Boundaries Excluded)	Regularity (Percentage of Hexagonal Cells)	Mean NND (μm)
1	25,933	3606	46.03	4.76
2	25,583	3557	47.17	4.82
3	25,691	3576	45.33	4.80
4	25,598	3566	45.54	4.81
5	25,805	3592	47.80	4.79
6	25,825	3596	45.13	4.78
7	25,607	3570	46.44	4.79
8	25,764	3588	48.10	4.80
9	25,663	3576	46.39	4.81
10	25,867	3600	45.14	4.77
Mean \pm St Dev	25,734 \pm 123	3583 \pm 16	46.31 \pm 1.09	4.79 \pm 0.02

^aThe Mean Density and Percentage of Hexagonal Cells is Compatible with Values of Previous Works at Corresponding Retinal Eccentricity [17,10,26].

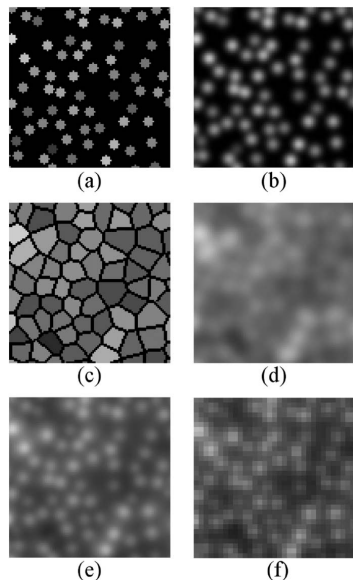


Fig. 2. To obtain the “peaks” image, circles are (a) first placed and then (b) blurred with a Gaussian filter. The “background” image was obtained through (d) the Gaussian blurring of (c) a Voronoi diagram. The two images (b) and (d) were then summed (e). The sum image was then rebinned by a factor three (f).

contribution, we used an image reproducing the Voronoi diagram, where every Voronoi cell has an intensity equal to that of the cone at its center. The Voronoi diagram image was also blurred with a Gaussian filter, broader than the one used for the peaks. The two images were subsequently summed. The resulting image was downsized by a factor of three using rebinning. Figure 2 illustrates the simulation process.

The reason for using the sum of two different images as defined can be explained if we consider the images acquired

by a fundus imager to be the result of convolution of the object, i.e., the photoreceptor layer, with a Point Spread Function (PSF) that presents both in-focus and out-of-focus contributions [28]. If we consider that the light is reflected from the cone cells in two points at different depths, then the “peaks” and “background” images simulate the light reflected at two different depths and with different focusing, reproduced with the different sizes of the Gaussian filters. We found that the approach of smoothing the Voronoi diagram gives simulated images which are more similar to real images than other approaches such as smoothing the reference image or using broader Gaussians in the cone location. This was determined by evaluating the difference between the intensity histograms of images with different backgrounds with the Earth Mover’s Distance metric [29]. This metric was minimized in the case of the Voronoi background.

Finally, we added Gaussian noise to the image. The variance of the noise was estimated according to the method presented by Lee and Hoppel [30], which considers the noise variance of an image as the minimum of the intensity variances calculated in blocks small enough to select only homogeneous areas of the image. We used for this the whole registered image, of which the reference image is a 256×256 pixel portion at the center, as the whole image presents also blood vessels, which have homogeneous areas in their inner sections. Figure 3 shows the comparison between a simulated image and the real image used as reference.

Each counting algorithm (Li and Roorda, Xue *et al.*, Chiu *et al.*, DAOPHOT) was tested on these synthetic images. In each case, the Voronoi diagram of the detected cones was determined, to exclude the cells at the boundaries from the statistics and to compare the regularity of the mosaic.

4. ANALYSIS

To test the performance of the detection algorithms, we used a variant of the Receiver Operator Characteristic (ROC) curve. The ROC curve is widely used in medical imaging to estimate the performance of detection techniques [31]. The ROC analysis was conceived for classification problems, i.e., when the

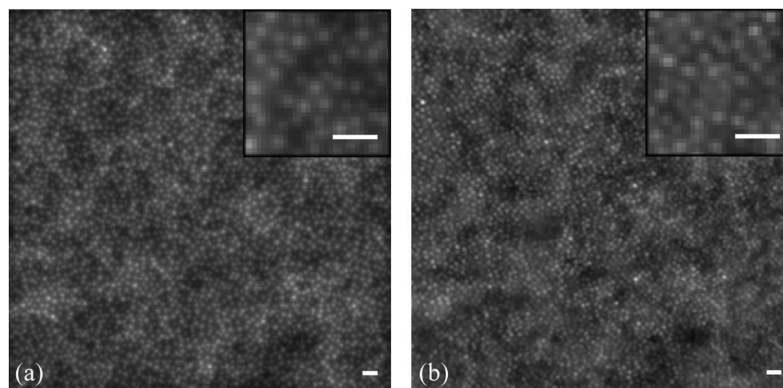


Fig. 3. (a) Example of a synthetic image obtained with the outlined process. The real image is shown in (b). The low-frequency variation of cone intensities follows the same pattern as the original image, but the coordinates and intensities of individual cones vary randomly. In the upper right corners, details of the respective images are shown (scale bars are $15 \mu\text{m}$). It can be noticed that the real image shows some patches with low brightness and no apparent presence of cones. It is not clear if this is because of illumination conditions or because of the characteristics of the retina itself.

detection process results in a positive/negative response, where positive means that a feature (e.g., a lesion) is present in the image and negative means that such feature is not present. In our case this is not applicable, as the task is to know how many cones are detected in the image and possibly if their position is correct. We therefore used a variant of the ROC analysis, the Free-response Receiver Operating Characteristic (FROC) curve.

The FROC analysis was introduced to integrate the localization task into the ROC analysis of data in the presence of multiple lesions [32]. When the detections are compared with ground truth data, they are divided into two types: true positive (TP), when a detection is within a specified tolerance from a true lesion, and false positive (FP) otherwise. The results are summarized by a plot of the fraction of detected lesions (TP over the number of real lesions) against the mean number of FP per image, obtained for different levels of confidence. The horizontal axis of the FROC curves is not normalized, as it can extend to an arbitrary number of FP. Each curve gives the detection performance for a detection algorithm (or “observer”). The perfect observer curve is a straight line that lies on the vertical axis from 0 to 1, where all the true lesions are detected and there are no FP. In comparing the performance of different observers, we can say that one observer is better than another if its curve is closer to the vertical axis and/or is higher.

In our study, the observers are represented by the detection algorithms. For each algorithm, a threshold (i.e., confidence level) was defined and varying the threshold traces a curve in the FROC plane. In the Li and Roorda algorithm, the threshold parameter is the value of the dimmest local maxima that are found after applying the *imregionalmax* function. In Xue *et al.*, the threshold is the peak value of the dimmest cone, and in the original version of the algorithm this was set by the user. In DAOPHOT, the threshold is the amplitude of the dimmest local maxima in the convolved image. Chiu *et al.*, compared with the other algorithms, does not have a parameter that can be straightforwardly chosen as a threshold. However, as the algorithm, similar to Xue *et al.*, has a preference for bright cones over dim cones, we set the same threshold that we used for Xue *et al.*, i.e., the peak value of the dimmest cone. The codes of the four algorithms were run by varying the threshold from the strictest one, with fewer detections, to the most relaxed one, with more detections.

Each of the four methods uses its own parameters besides the threshold value. The only parameter in Li and Roorda is the standard deviation of the Gaussian low-pass filter, but as it corresponds to the minimum cone separation, this has a fixed value. The Xue *et al.* parameters are the standard deviation of the Gaussian filter that is applied for the estimation of the background, the number of intensity ranges, and the size of the mask used to delete the detected cones. The Chiu *et al.* parameters were empirically found by the authors in the original work and were not modified here. In DAOPHOT, the only parameter is the standard deviation of the Gaussian used for the convolution. Before comparing them, we run Xue *et al.* and DAOPHOT algorithms with different values of the parameters, to find the combination of values that results in the best performance. This was done by tracing an FROC curve for each parameter combination of each code and choosing the parameter values that gave the highest

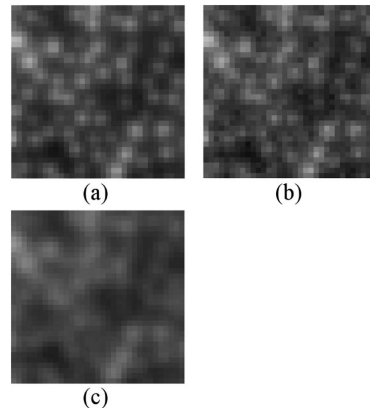


Fig. 4. Detail of (a) a simulated image, (b) detail of the same image with five times the original noise, and (c) with a Gaussian blur filter of 1 pixel standard deviation.

curve. Contrary to the ROC analysis, at present there is no universally accepted method for fitting FROC curves nor a single index that summarizes the overall performance [33]. Two of the criteria commonly used to evaluate the detection algorithms are the calculation of the area under the curve up to a certain FP value [34] and the TP fraction value at a fixed FP number [35]. We use the latter in this work.

A problem that is not usually assessed in cone detection studies is how the quality of the images affects the detection. Registration and summing of frames is performed to obtain a final image with increased signal-to-noise ratio and quality [24]. However, the final image can present poor quality, especially in the case of diseased eyes [36]. We therefore simulated two series of images with decreasing quality by applying a Gaussian blur of increasing width (with standard deviations of 0, 0.25, 0.5, 0.75, and 1 pixel) and by adding a stronger noise (with standard deviation from 1 to 5 times the value retrieved from the reference image) to one image with the same features as the previously simulated images (Fig. 4).

While DAOPHOT uses interpolation to retrieve the cone positions with sub-pixel accuracy, the cones found by the Li and Roorda and the Xue *et al.* algorithms have integer coordinates for the majority of the detections. Li and Roorda and Xue *et al.* detections, in fact, have non-integer coordinates only when the centroids are calculated for connected regions that are non-symmetrical with respect to the pixel grid, and this is not usually the case. Chiu *et al.* use centroids of connected regions as well, but it is more common that the connected areas are non-symmetrical compared to the other two algorithms.

For this reason, we also performed the whole detection process after increasing the size of the images by a factor 2 and by a factor 3 using cubic interpolation [27], to increase the sampling to 0.75 and 0.5 μm per pixel and see how this affects the cone localization. Even if the resizing process does not add information to the images, we performed it because we wanted to determine if the accuracy of the localization process has a significant influence on the calculation of those image parameters that are position dependent, such as the percentage of hexagonal cells and the mean NND.

The benefit of using the FROC analysis is not only to have a method to compare the algorithms, but also to have an objective way to determine the best operating point along the curve, i.e., threshold value, at which the detection operates. As the horizontal axis is unbound, in clinical practice FROC curves are usually displayed only over the FP range that is considered of clinical interest, with the choice of a maximum acceptable value of FP. The cone density varies significantly, even between individual healthy subjects and at the eccentricity studied by us, 2.5 degrees temporal, the coefficient of variation can reach 15% [17,36]. Therefore, we considered 500 FP (approximately to 15% of the mean number of cones per image) as the maximum acceptable FP value, determining that if the FP exceeds this value, then the error is too large to be useful. The operating point was chosen similarly as for the ROC analysis by selecting the point on the curve closest to the upper left corner (0,1).

We therefore run four algorithms with the threshold at the operating point for every image, and then calculate the cone parameters (cone density, percentage of hexagonal voronoi, and mean NND) as if the results were not corrected by human intervention, i.e., considering all the detections as TP. This was done to test the reliability of the results of the algorithms if they are run in automated mode.

5. RESULTS

To trace the FROC curves, we used three values for the radius of the tolerance region for the discrimination between TP and FP: 0.5, 1.0, and 1.5 μm , that correspond to 0.33, 0.67, and 1.0 pixel on the original size images. Figures 5(a)–5(c) show the FROC curves of the four algorithms averaged over 10 simulated images.

As expected, the overall performance for all of the algorithms increases as the tolerance radius is relaxed. Li and Roorda is the algorithm that, according to the definition of FROC curve, performs best, with a curve very close to the vertical axis if exact localization is not required. Nonetheless, even if the algorithm gives almost no FP, the percentage of correctly detected cones in our case reaches 85% if the images are not resized. With resizing, the percentage slightly increases but does not exceed 90% in any case. With images at their original size, the operating point of the Xue *et al.* algorithm stops at 66% of TP, with a number of FP that correspond to 4% of the real cones. However, the performance increases steadily with the resizing factor, as the TP fraction goes from 85% with a resizing of two, to 92% with a resizing of three, with FP percentages that are respectively of 2% and 0.7%. The Chiu *et al.* performance on original size images is similar to Li and Roorda, with 82% TP and almost no FP. After resizing is applied, the TP fraction increases to 97% and 94%, with an FP percentage less than 1% in both cases. DAOPHOT performance in the first case is similar to Xue *et al.*, with a TP fraction of 59% and an FP percentage of 3%. For resized images, DAOPHOT performance at the operating point is practically identical to Chiu *et al.*

The cone parameters as calculated from the detections were compared to the real values, i.e., the values used in the simulation and presented in Table 1. Table 2 shows the means and standard deviations of the percentage differences of the parameters.

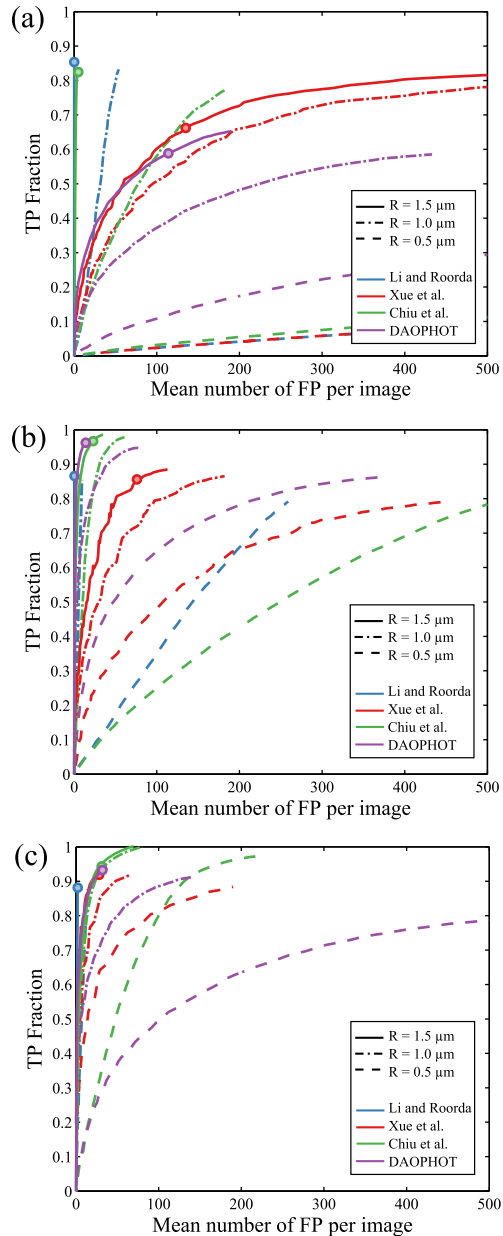


Fig. 5. FROC curves for ten images (a) without resizing, (b) resized by two, and (c) resized by three. Each plot displays the curves for the three tolerance radii (solid, dashed-dotted, and dashed line) and for the four algorithms (blue, red, green, and purple). The operating points are marked with circles on the solid lines.

The cone density is underestimated by all the algorithms. The best overall estimates are achieved by Chiu *et al.* and DAOPHOT after doubling the size of the images, with a mean

of -2.68% and -2.84% difference from the real value. If the images are resized, Xue *et al.*, Chiu *et al.*, and DAOPHOT achieve better estimates of the cone density than Li and Roorda, for which the mean percentage difference is greater than 10% in both cases. The regularity of the cone mosaic is the parameter that has the overall biggest uncertainty in its calculation, with standard deviations from 1.62% to 3.10% . As for the cone density, the regularity is underestimated in every case, with a difference that goes from -0.58% for Chiu *et al.* with resizing 2 to -20% for Xue *et al.* with no resizing. The mean NND, on the

other hand, is generally overestimated, with the exception of DAOPHOT. Compared to the corresponding estimates of cone density and regularity for the same algorithm, NND estimates are usually more accurate, with a difference that does not exceed 13% in any case.

Figure 6 shows how the quality of the images (noise and blur) affects the calculation of the cone parameters. The plots display the percentage difference of the parameters against the standard deviation of the Gaussian noise (in counts per pixel) and the standard deviation of the Gaussian filter used

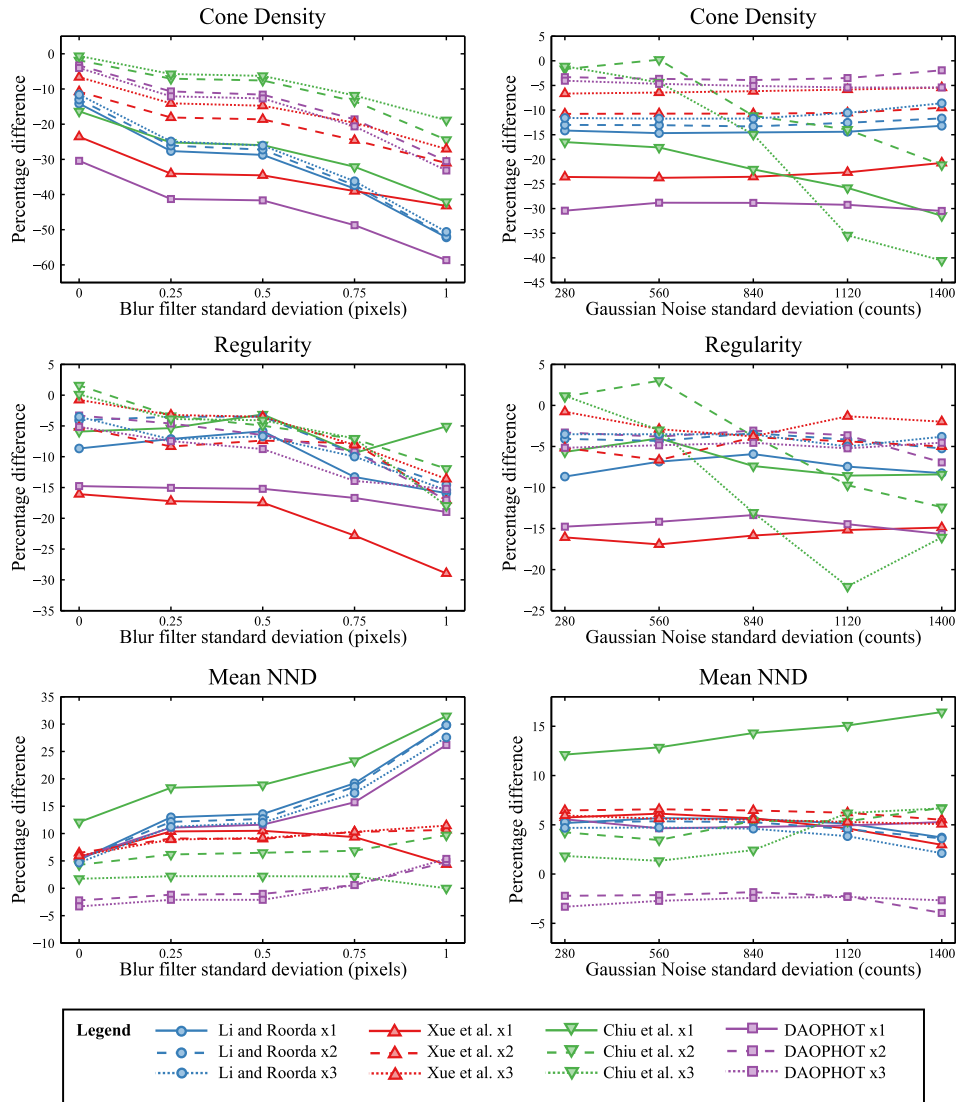


Fig. 6. Cone parameters for increasing blur and noise. The resizing used is shown with different lines; the algorithms are marked with different colors and markers.

for the blurring (in pixels). The amount of noise in the image, even if increased to five times the value retrieved from the original images, does not significantly affect the results, with the exception of Chiu *et al.* The amount of blur, on the other

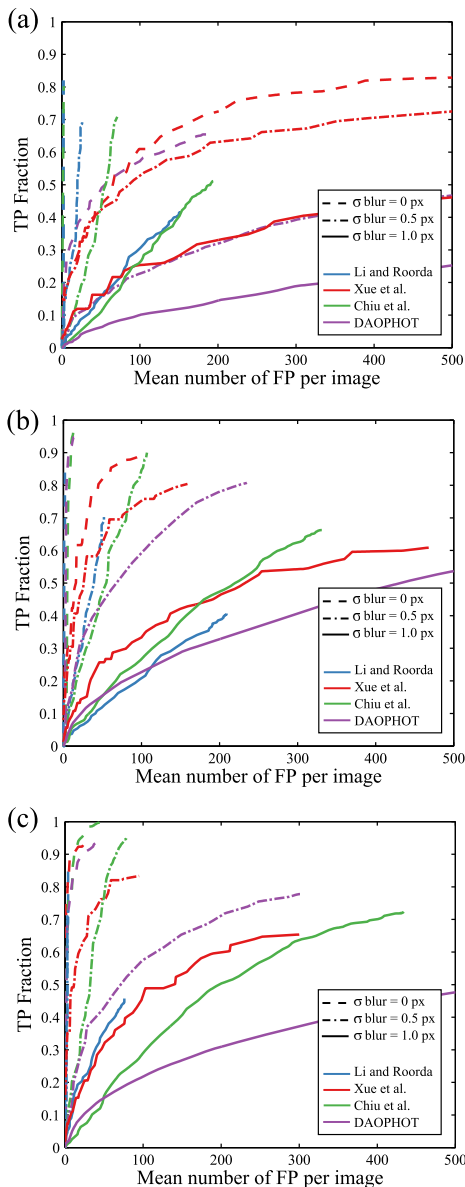


Fig. 7. FROC curves for one image with increasing blur (a) without resizing, (b) resized by two, and (c) resized by three. The tolerance radius used is $1.5 \mu\text{m}$. Each plot displays the curves for three standard deviations of the Gaussian filter applied on the same image (dashed, dashed-dotted, and solid line) and for the four algorithms (blue, red, green, and purple colors).

Table 2. Mean Values and Standard Deviations of the Parameters' Percentage Differences for the Detections on the Images Compared to the Values Presented in Table 1

	Cone Density	Regularity	Mean NND
Resize x1			
Li and Roorda	-13.83 ± 0.92	-10.68 ± 2.81	5.69 ± 0.53
Xue <i>et al.</i>	-28.00 ± 3.68	-20.59 ± 2.50	9.32 ± 2.65
Chiu <i>et al.</i>	-17.09 ± 0.54	-7.24 ± 2.48	12.75 ± 0.38
DAOPHOT	-37.41 ± 2.00	-18.35 ± 3.10	10.80 ± 1.48
Resize x2			
Li and Roorda	-12.88 ± 0.86	-8.83 ± 2.19	5.60 ± 0.60
Xue <i>et al.</i>	-11.57 ± 1.30	-8.71 ± 2.54	7.19 ± 0.78
Chiu <i>et al.</i>	-2.68 ± 0.64	-0.58 ± 1.62	4.67 ± 0.34
DAOPHOT	-2.84 ± 0.23	-4.08 ± 2.19	-1.85 ± 0.35
Resize x3			
Li and Roorda	-11.39 ± 0.66	-8.48 ± 2.39	4.78 ± 0.49
Xue <i>et al.</i>	-7.32 ± 0.73	-4.91 ± 1.64	6.36 ± 0.39
Chiu <i>et al.</i>	-3.19 ± 1.78	-2.98 ± 1.85	2.03 ± 0.55
DAOPHOT	-5.18 ± 0.35	-6.93 ± 2.42	-2.56 ± 0.40

hand, has a greater effect on the detections for all the algorithms. In the worst case, in fact, only 40% of the cones are detected, and the mean NND peaks at 30% difference from the real value.

Figures 7(a)–7(c) show the FROC curves of the four algorithms for the same image with gradually decreasing quality (since we saw that the noise effect is limited, we include only the FROC curves for increasing levels of blur). The radius of the tolerance region corresponds to the most relaxed of the radii used in Fig. 5 ($1.5 \mu\text{m}$). All of the algorithms show a significant decrease in their performance as the quality of the image worsens, leading to less detection of TP, as well as more FP.

6. DISCUSSION

In this study, we developed a method for the simulation of AO corrected images of cone photoreceptors, and we used the simulated images to test the performance of four automated cone detection algorithms.

If the simulated images are analyzed at their original size, then the Li and Roorda algorithm has the best results and it is, together with Chiu *et al.*, the only one with an acceptable performance, with 85% of the cones detected. It can be seen that the process of increasing the size of the images by factors of two and three improves the performance of Xue *et al.*, Chiu *et al.*, and DAOPHOT algorithms, even if no new information is added. We believe that the main cause for this change is the better sampling of the images. In Xue *et al.*, the fact that the cones are better sampled allows a more precise deletion in the deletion step, reducing the detection of FP at the borders of the deleted areas. The best performance reached by the algorithm, 96% of TP, is close to the value given in the original study, 97.7% [11]. Chiu *et al.* also benefit from the improved sampling of the images, as the segmentation of the cones is more precise. In the case of DAOPHOT, a Gaussian function is used to fit the cones. The Gaussian function is the best choice for well-sampled images, i.e., PSF with a full width half-maximum of at least 2.5 pixels [22], but this is approximately the size of the cones with the original sampling.

Doubling the size of the images is already sufficient to reach a very good performance with DAOPHOT, and it is not improved by further increasing the size.

Even if the FROC curves are a useful way to visualize the overall performance of the algorithms, we are more interested in the accuracy of the cone packing parameters (Table 2), as these represent the information actually used by clinicians. Without the discrimination between TP and FP, the most noticeable consequence is that the number of FP detections can compensate for an equal number of missed TP, leading to a better estimate of the cone density with an actually poorer detection performance. For this reason, the choice of an operating point is very important as it actually sets a limit to the number of FP and to apparently good, but actually incorrect, density estimates. From Table 2, we can see that density is always underestimated. The fact that the Li and Roorda algorithm incurs fewer FP, but also has fewer TP than the other algorithms at their best, leads to worse estimates of cone density and mosaic regularity.

The mean NND results improve with the resizing, as the increased sampling allows a better determination of cone positions. It is also to be noticed that a better estimate of one parameter, i.e., mean NND, does not necessarily correspond to an improvement in other parameters such as regularity.

As in the case of cone density, the percentage of hexagonal Voronoi cells is underestimated in every case, as the undetected cones cause a greater deviation from the hexagonal arrangement. Compared with density and NND, regularity shows no significant improvement with resizing from double to triple. Together with this, it is also the parameter with the largest uncertainty. These reflections suggest that the Voronoi analysis results are less stable than other metrics, and so their reliability needs to be thoroughly considered when used clinically, as noticed also in recent works [18].

It is noticed that, while doubling the size of the images provides a major improvement in the parameter estimates, resizing by a factor of three leads to further improvement in only a limited number of cases. Moreover, the best performance for all three parameters is achieved using the resize factor of two, the DAOPHOT algorithm for cone density, and the mean NND and Chiu *et al.* for the regularity. This suggests that, to achieve a significant improvement in the parameter accuracy, an excessive increase of the sampling, which would require more computational time as well as computer memory, is not needed. Chiu *et al.* is the only algorithm that detects all the cones if the threshold is the most relaxed. It is to be noted, though, that this is possible at the expense of the speed of the detection process, as this algorithm is the most complex of those analyzed.

In Figure 6, it can be seen that the addition of noise affects significantly only the results of the Chiu *et al.* algorithm. Li and Roorda use a low-pass filter to remove the high-frequency noise, and this step proves to be effective since its results remain substantially constant as the noise increases. For this reason, we believe that the dependence of the performance of Chiu *et al.* on the noise can be stabilized in a similar way by using low-pass filtering as the first step in the detection process. Even if the two other algorithms show a small decline in their performance, too, a preliminary low-pass filtering can, in principle, be added to both of them to further limit the effect of noise.

By contrast, the deterioration because of the blurring notably worsens the performance of the algorithms. All of the algorithms are affected in a similar way by blurring. Xue *et al.*, Chiu *et al.*, and DAOPHOT seem to produce inconsistent results, with an improvement in the NND measurement, while density and regularity worsen. This could be caused by a significant number of FP.

In the case of the Li and Roorda algorithm, the dependence of the performance on the level of blur in the image could explain why, in our study, the percentage of detections never exceeds 90%, while in the original work the agreement between the manual and the automated labelling is between 93% and 96% [10]. It is likely that this difference is because of the quality of the images used. Our images were simulated using as reference images acquired with a commercial AO fundus camera. Li and Roorda, on the other hand, used images acquired in a university laboratory, both with flood-illuminated and scanning laser ophthalmoscope AO systems, which generally achieve better contrast [2]. Therefore, we can say that the quality of an image data set, which can depend both on the condition of the subject's eye and on the imaging system used, has a significant impact on the performance of the cone detection algorithms.

Finally, it is to be noted that Li and Roorda and Chiu *et al.* are the only algorithms that do not have a parameter that accounts for the size of the cones. Because of this, they can, in principle, be used without modifications for images of cones acquired at different distances from the fovea. On the other hand, Xue *et al.* and DAOPHOT have size dependent parameters, respectively the size of the mask that excludes the detected cones and the radius of the Gaussian fitting function, that would need to be optimized every time.

7. CONCLUSIONS

We have developed a method for the simulation of retinal images of cones in the parafoveal region, and we used it to reproduce images acquired with a commercial AO-assisted fundus camera. The simulation data were used to test and compare the performance of three automated cone detection algorithms. We introduced the use of FROC analysis to optimize the algorithm parameters and to determine the operating point for each algorithm. The performance of the algorithms was then compared considering both the TP and FP detections and the estimates of the cone parameters (density, packing regularity, and mean NND).

We found that the spatial sampling of the images, even using resizing of the recorded images, has a significant impact on the performance of the algorithms, but also that an excessive upsizing does not improve substantially the measurements. It is suggested that the image sampling should always be provided when presenting results obtained using these algorithms.

We saw that the percentage of hexagonal Voronoi cells is the parameter which is most affected by errors in cone detection and, for this reason, the combined measurements of more parameters could be a better choice to characterize different retinal regions and the retinas of different subjects [37].

We studied, moreover, how the performance was affected by the introduction of a variable quantity of noise or blur, finding that the level of blur significantly affects the detections and the derived parameters.

As the algorithms were tested when used automatically, we believe that the results of this paper can be taken as reference for their reliability and accuracy for clinicians who want to perform cone detection without further manual supervision. The detection of cones in diseased eyes or in low-quality images, on the other hand, still requires accurate supervision, especially when the difference with healthy eyes is subtle [37], and needs to be addressed in future studies.

ACKNOWLEDGMENTS

The authors would like to thank the Irish Research Council (IRC) (GOIPG/2013/775) for financial support. We thank also Dr. Marco Lombardo (Rome, Italy) for providing the image data set and for his valuable comments and revision of the manuscript.

REFERENCES

1. J. Liang, D. R. Williams, and D. T. Miller, "Supernormal vision and high-resolution retinal imaging through adaptive optics," *J. Opt. Soc. Am. A* **14**, 2884–2892 (1997).
2. K. M. Hampson, "Adaptive optics and vision," *J. Mod. Opt.* **55**, 3423–3424 (2008).
3. J. Carroll, D. Kay, D. Scoles, A. Dubra, and M. Lombardo, "Adaptive optics retinal imaging—clinical opportunities and challenges," *Curr. Eye Res.* **38**, 709–721 (2013).
4. D. Williams and R. Collier, "Consequences of spatial sampling by a human photoreceptor mosaic," *Science* **221**, 385–387 (1983).
5. D. R. Williams and N. J. Coletta, "Cone spacing and the visual resolution limit," *J. Opt. Soc. Am. A* **4**, 1514–1523 (1987).
6. J. I. Yellott, "Spectral consequences of photoreceptor sampling in the rhesus retina," *Science* **221**, 382–385 (1983).
7. N. M. Putnam, H. J. Hofer, N. Doble, L. Chen, J. Carroll, and D. R. Williams, "The locus of fixation and the foveal cone mosaic," *J. Vision* **5**(7), 632–639 (2005).
8. R. Garrioch, C. Langlo, A. M. Dubis, R. F. Cooper, A. Dubra, and J. Carroll, "Repeatability of in vivo parafoveal cone density and spacing measurements," *Ophthalmol. Vis. Sci.* **89**, 632–643 (2012).
9. Y. Kitaguchi, K. Bessho, T. Yamaguchi, N. Nakazawa, T. Mihashi, and T. Fujikado, "In vivo measurements of cone photoreceptor spacing in myopic eyes from images obtained by an adaptive optics fundus camera," *Jpn. J. Ophthalmol.* **51**, 456–461 (2007).
10. K. Y. Li and A. Roorda, "Automated identification of cone photoreceptors in adaptive optics retinal images," *J. Opt. Soc. Am. A* **24**, 1358–1363 (2007).
11. B. Xue, S. S. Choi, N. Doble, and J. S. Werner, "Photoreceptor counting and montaging of en-face retinal images from an adaptive optics fundus camera," *J. Opt. Soc. Am. A* **24**, 1364–1372 (2007).
12. S. J. Chiu, Y. Likhnygina, A. M. Dubis, A. Dubra, J. Carroll, J. A. Izatt, and S. Farsiu, "Automatic cone photoreceptor segmentation using graph theory and dynamic programming," *Biomed. Opt. Express* **4**, 924–937 (2013).
13. A. Turpin, P. Morrow, B. Scotney, R. Anderson, and C. Wolsley, "Automated identification of photoreceptor cones using multi-scale modelling and normalized cross-correlation," *Lect. Notes Comput. Sci.* **6978**, 494–503 (2011).
14. F. Mohammad, R. Ansari, J. Wanek, and M. Shahidi, "Photoreceptor cell counting in adaptive optics retinal images using content-adaptive filtering," *Proc. SPIE* **7626**, 762611 (2010).
15. K. Loquin, I. Bloch, K. Nakashima, F. Rossant, and M. Paques, "Photoreceptor detection in *in-vivo* adaptive optics images of the retina: Towards a simple interactive tool for the physicians," in *Proceedings—International Symposium on Biomedical Imaging* (IEEE, 2011), pp. 191–194.
16. R. F. Cooper, C. S. Langlo, A. Dubra, and J. Carroll, "Automatic detection of modal spacing (Yellott's ring) in adaptive optics scanning light ophthalmoscope images," *Ophthalmic Physiol. Opt.* **33**, 540–549 (2013).
17. C. A. Curcio, K. R. Sloan, R. E. Kalina, and A. E. Hendrickson, "Human photoreceptor topography," *J. Comp. Neurol.* **292**, 497–523 (1990).
18. M. Lombardo, S. Serrao, and G. Lombardo, "Technical factors influencing cone packing density estimates in adaptive optics flood illuminated retinal images," *PLoS One* **9**, e107402 (2014).
19. S. J. Chiu, C. A. Toth, C. B. Rickman, J. A. Izatt, and S. Farsiu, "Automatic segmentation of closed-contour features in ophthalmic images using graph theory and dynamic programming," *Biomed. Opt. Express* **3**, 1127–1140 (2012).
20. C. Harris and M. Stephens, "A combined corner and edge detector," in *Proceedings of the Fourth Alvey Vision Conference*, C. J. Taylor, ed. (AVC, 1988), Vol. **15**, pp. 147–151.
21. D. G. Lowe, "Distinctive image features from scale-invariant keypoints," *Int. J. Comput. Vision* **60**, 91–110 (2004).
22. L. E. Davis, "A reference guide to the IRAF/DAOPHOT package," IRAF Programming Group, NOAO, Tucson (1994).
23. M. Lombardo, G. Lombardo, P. Ducoli, and S. Serrao, "Adaptive optics photoreceptor imaging," *Ophthalmol. Annu.* **119**, 1498 (2012).
24. G. Ramaswamy and N. Devaney, "Pre-processing, registration and selection of adaptive optics corrected retinal images," *Ophthalmic Physiol. Opt.* **33**, 527–539 (2013).
25. R. M. Mersereau, "The processing of hexagonally sampled two-dimensional signals," *Proc. IEEE* **67**, 930–949 (1979).
26. S. P. Park, J. K. Chung, V. Greenstein, S. H. Tsang, and S. Chang, "A study of factors affecting the human cone photoreceptor density measured by adaptive optics scanning laser ophthalmoscope," *Exp. Eye Res.* **108**, 1–9 (2013).
27. M. Lombardo, S. Serrao, P. Ducoli, and G. Lombardo, "Eccentricity dependent changes of density, spacing and packing arrangement of parafoveal cones," *Ophthalmic Physiol. Opt.* **33**, 516–526 (2013).
28. L. Blanco, L. Mugnier, and M. Glanc, "Myopic deconvolution of adaptive optics retina images," *Proc. SPIE* **7904**, 790412 (2011).
29. Y. Rubner, C. Tomasi, and L. J. Guibas, "Earth mover's distance as a metric for image retrieval," *Int. J. Comput. Vision* **40**, 99–121 (2000).
30. J. Lee and K. Hoppel, "Noise modeling and estimation of remotely-sensed images," in *Digest—International Geoscience and Remote Sensing Symposium (IGARSS)* (IEEE, 1989), Vol. **2**, pp. 1005–1008.
31. H. Barrett and K. Myers, *Foundations of Image Science*, Wiley series in pure and applied optics (Wiley, 2004).
32. P. C. Bunch, J. F. Hamilton, G. K. Sanderson, and A. H. Simmons, "A free response approach to the measurement and characterization of radiographic observer performance," in *Application of Optical Instrumentation in Medicine VI* (International Society for Optics and Photonics, 1977), pp. 124–135.
33. A. I. Bados, H. E. Rockette, T. Song, and D. Gur, "Area under the free-response ROC curve (FROC) and a related summary index," *Biometrics* **65**, 247–256 (2009).
34. R. N. Strickland, *Image-Processing Techniques for Tumor Detection* (CRC Press, 2002).
35. D. P. Chakraborty, E. S. Breatnach, M. V. Yester, B. Soto, G. Barnes, and R. Fraser, "Digital and conventional chest imaging: a modified ROC study of observer performance using simulated nodules," *Radiology* **158**, 35–39 (1986).
36. M. Lombardo, S. Serrao, N. Devaney, M. Parravano, and G. Lombardo, "Adaptive optics technology for high-resolution retinal imaging," *Sensors* **13**, 334–366 (2013).
37. M. Lombardo, M. Parravano, G. Lombardo, M. Varano, B. Boccassini, M. Stirpe, and S. Serrao, "Adaptive optics imaging of parafoveal cones in type 1 diabetes," *Retina* **34**, 546–557 (2014).

CONFERENCE PAPER

Mariotti, L. & Devaney, N.

Cone detection and blood vessel segmentation
on AO retinal images

*IRISH MACHINE VISION & IMAGE PROCESSING Conference
proceedings 2015*, Dahyot, R.; Lacey, G.; Dawson-Howe, K.; Pitié,
F. & Moloney, D. (Eds.), 126-128 (2015)

3.1 CONTRIBUTIONS

In the study of the photoreceptors, it is common practice to select small windows (e.g. $200\ \mu\text{m} \times 200\ \mu\text{m}$ or smaller) on the images of the cone mosaic. This procedure ensures that the cone density can be considered constant inside the window. Even if the AO images acquired with the rtx1 camera have a narrow field of view ($4^\circ \times 4^\circ$), it is usually big enough to include the shadows projected by the retinal blood vessels on the photoreceptor layer. As the vessel areas are always excluded from the analysis process, this implies that the position of the small windows needs to be selected manually.

Regarding this issue, I thought that the segmentation of the vessel shadows could lead to a significant reduction of the manual intervention. There are many methods that have been proposed to automatically segment the blood vessels in retinal images, but they all have been developed for low-resolution images and work poorly in AO retinal images [123].

I then decided to develop an algorithm for the segmentation of blood vessel shadows in this particular type of images that would require minimum manual intervention. In the final version of the procedure, only two parameters needed to be set manually and their values are expected to be similar between different images acquired with the same instrument, greatly increasing the automation of the whole window selection process (a visualization of the advantage of the use of this approach can be seen in

Appendix A). The procedure was peer-reviewed and published as a short paper in the proceedings of the Irish Machine Vision and Image Processing conference 2015.

Cone detection and blood vessel segmentation on AO retinal images

L. Mariotti & N.Devaney

*Applied Optics Group, School of Physics
National University of Ireland, Galway*

Abstract

With the advent of Adaptive Optics (AO) for the high-resolution imaging of the retina, it is possible to study the individual photoreceptors and their spatial distribution *in vivo*. The presence of the blood vessels affects negatively the detections, and for this reason clinicians select manually the regions devoid from the vessels to be analysed. We present here a method that we developed for the segmentation of blood vessels in AO retinal images. With the choice of a suitable cone detection algorithm, we are now able to automatically analyse the images acquired by an AO fundus camera in their entirety.

Keywords: image processing, ophthalmology, Adaptive Optics, segmentation

1 Introduction

Thanks to the advent of Adaptive Optics (AO) in vision science, it has become possible for clinicians to study the human retina *in vivo* with high-resolution images. The detection of cone photoreceptors is important, as their spatial distribution is strongly related to the quality of the subject's vision and can indicate the presence of clinical conditions (Figure 1). In previous work [Mariotti and Devaney, 2015] we implemented and compared the most commonly used cone detection algorithms.

It is common practice for clinicians to select small rectangular windows on the image in which to perform cone detection and to analyse the metrics related to cone spacing. The windows are selected in order to exclude the shadow projected by blood vessels on the photoreceptor layer, as the resulting detections would be unreliable. There are already algorithms in the literature proposed for the segmentation of retinal vessels, but they are developed for low-resolution retinal images, and did not perform well on our high-resolution images.

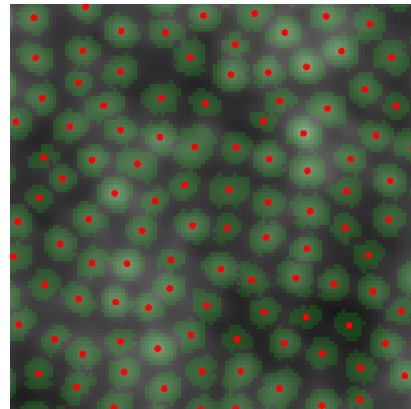


Figure 1: Example of cone detection with segmentation

2 Method

The two cone detection algorithms that we use in our analysis were developed by [Li and Roorda, 2007] and [Chiu et al., 2013]. The Li and Roorda algorithm detects the cones as the local maxima in the image. The Chiu

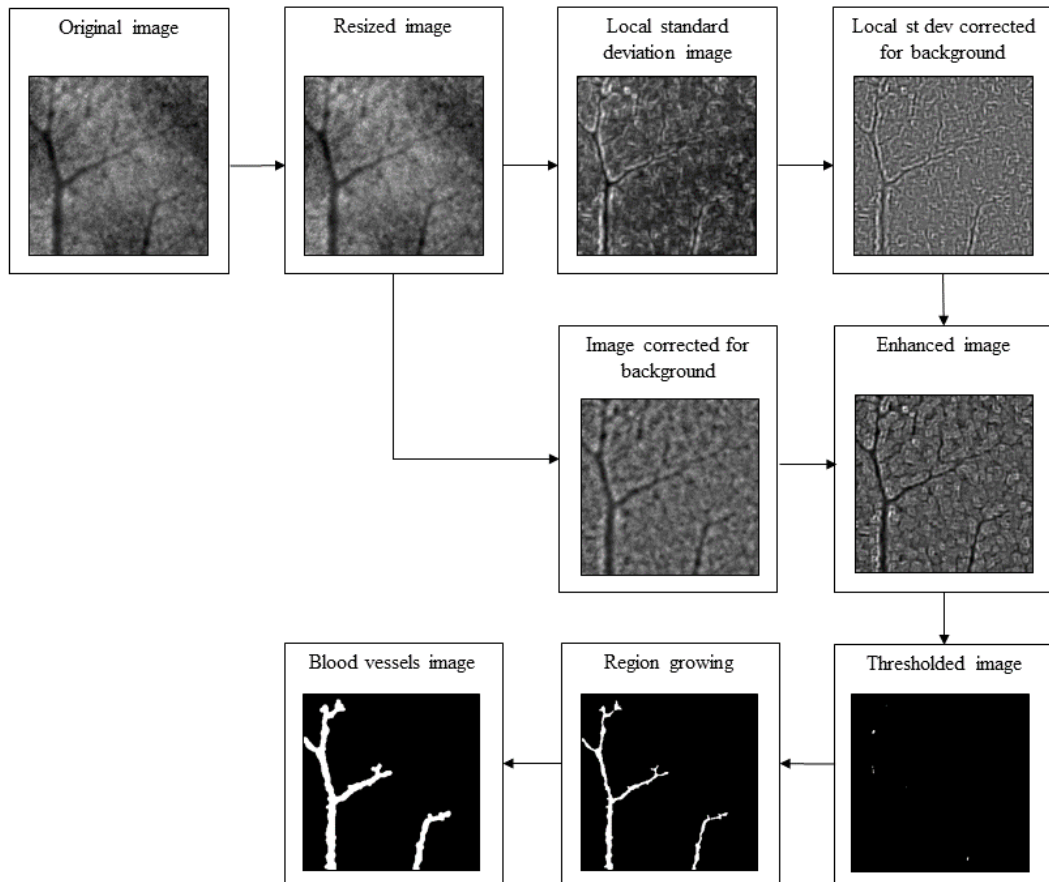


Figure 2: Diagram showing the selection of the blood vessels from the original image

et al. algorithm extends the detection by segmenting the cone profiles around the local maxima (Figure 1). A portion of the image surrounding each maximum is transformed into quasi-polar coordinates, then the contour of the cone is segmented as a layer using graph theory and dynamic programming.

In order to segment the blood vessels from the rest of the image, we examine the local standard deviation of the images, as this will be reduced where there are the vessel shadows. We downsize the images by a factor of four, in order to discard the high-frequency spatial information given by the cones. The local standard deviation of the images is calculated, and multiplied by the original image to enhance the blood vessels, after correcting both images for low-frequency background variations.

The vessel profiles were then found using region growing around the minimum intensity pixels of the enhanced image. The threshold for selecting the seed points and the parameter that regulates the extension of the region growing are chosen manually after visual inspection of the results (however, when using the same instrument it does not vary significantly between patients). A diagram of the procedure is shown in Figure 2.

3 Conclusions

The segmentation of the vessels allows us to perform a complete analysis on the cone mosaic, increasing the area and the number of cones that can be included in the study (Figure 3) and removing the necessity to manually select windows. This simplification will facilitate clinical use, resulting in an increased number of patients that can be examined.

We thank Marco Lombardo for acquiring the images (with *rtx1* camera of Imagine Eyes, Orsay, France) and the Irish Research Council for financial support.

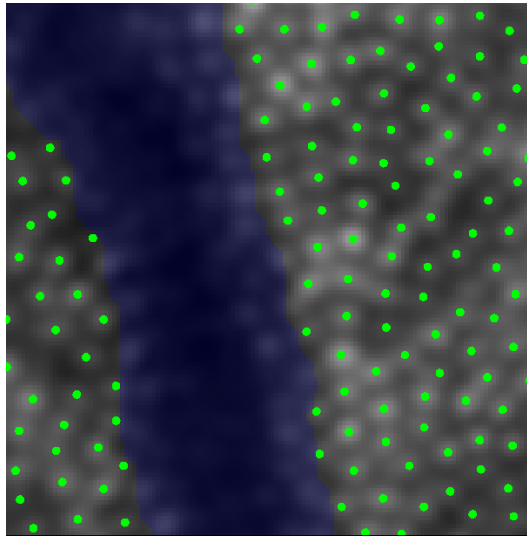


Figure 3: Detail of cone detections (green dots) with the exclusion of the blood vessel profile (blue)

References

- [Chiu et al., 2013] Chiu, S. J., Lokhnygina, Y., Dubis, A. M., Dubra, A., Carroll, J., Izatt, J. A., and Farsiu, S. (2013). Automatic cone photoreceptor segmentation using graph theory and dynamic programming. *Biomed. Opt. Express*, 4(6):924–937.
- [Li and Roorda, 2007] Li, K. Y. and Roorda, A. (2007). Automated identification of cone photoreceptors in adaptive optics retinal images. *JOSA A*, 24(5):1358–1363.
- [Mariotti and Devaney, 2015] Mariotti, L. and Devaney, N. (2015). Performance analysis of cone detection algorithms. *J. Opt. Soc. Am. A*, 32(4):497–506.

Mariotti, L.; Devaney, N.; Lombardo, G. & Lombardo, M.

Understanding the changes of cone reflectance in adaptive optics flood illumination retinal images over three years

Biomedical Optics Express, 7, 2807-2822 (2016)

4.1 CONTRIBUTIONS

After the work on the cone detection algorithms, we decided to move towards the analysis of real images. Our collaborator Marco Lombardo (Fondazione G. B. Bietti IRCCS, Rome, Italy) provided us a set of images acquired in his research center in Rome. The data set consisted of a series of images acquired at the same retinal locations of a healthy subject at different times, with difference between the acquisition times ranging from minutes to years.

In a clinical environment, the monitoring of a subject is usually carried out with observation sessions separated by months or years. For this reason, we thought it was important to see how the time separation affects the cone mosaic analysis in healthy subjects before anything significant about diseased subjects can be said. In addition to time separation, the position of the light source used by the operator of the rtx1 camera could also be a source of differences observed in the cone mosaic. In fact, the viewer interface of the rtx1 shows the four Purkinje points that are used as reference points for collecting high-quality images, but between the center and the edges of the Purkinje points the illumination is displaced by 0.35 mm. For this reason, on the side of the analysis of cone mosaic over time, I also carried out a quantitative comparison of pairs of images acquired close in time with the light source positioned on-center and off-center (0.35 mm temporal) in order to verify how much this displacement can affect the analysis and so determine if images acquired without precise specification of the illumination position can still be used.

I refined a procedure for the pre-processing (flat-fielding and registration) that could work on images of the same cone mosaic acquired at different times, i.e. with variations in cone reflectance. This included also the procedure for the segmentation of the blood vessels previously described in the Irish Machine Vision and Image Processing conference paper (Chapter 3), in order to maximise the extension of the area to be analysed and to reduce manual intervention. Among the different aspects of the cone mosaic that we could have analysed in the post-processing, we decided to focus on the reflectance of the cones rather than their spatial distribution, which has received more attention in the literature, and on the identification of the individual cones. Our collaborators Marco and Giuseppe Lombardo helped us in the redaction of the manuscript and in the discussion of the clinical aspects of the results.

This work was submitted to Biomedical Optics Express and accepted for publication.

Understanding the changes of cone reflectance in adaptive optics flood illumination retinal images over three years

Letizia Mariotti,¹ Nicholas Devaney,^{1,*} Giuseppe Lombardo,^{2,3} and Marco Lombardo⁴

¹*Applied Optics Group, School of Physics, National University of Ireland, Galway, Ireland*

²*Istituto per i Processi Chimico-Fisici, Consiglio Nazionale delle Ricerche, Viale F. Stagno D'Alcontres 37, 98158, Messina, Italy*

³*Vision Engineering Italy srl, Via Adda 7, 00198 Rome, Italy*

⁴*Fondazione G.B. Bietti IRCCS, Via Livenza 3, 00198 Rome, Italy*

[*nicholas.devaney@nuigalway.ie](mailto:nicholas.devaney@nuigalway.ie)

Abstract: Although there is increasing interest in the investigation of cone reflectance variability, little is understood about its characteristics over long time scales. Cone detection and its automation is now becoming a fundamental step in the assessment and monitoring of the health of the retina and in the understanding of the photoreceptor physiology. In this work we provide an insight into the cone reflectance variability over time scales ranging from minutes to three years on the same eye, and for large areas of the retina ($\geq 2.0 \times 2.0$ degrees) at two different retinal eccentricities using a commercial adaptive optics (AO) flood illumination retinal camera. We observed that the difference in reflectance observed in the cones increases with the time separation between the data acquisitions and this may have a negative impact on algorithms attempting to track cones over time. In addition, we determined that displacements of the light source within 0.35 mm of the pupil center, which is the farthest location from the pupil center used by operators of the AO camera to acquire high-quality images of the cone mosaic in clinical studies, does not significantly affect the cone detection and density estimation.

© 2016 Optical Society of America

OCIS codes: (110.1080) Adaptive optics; (330.7331) Visual optics, receptor optics; (170.3880) Medical and biological imaging.

References and links

1. K. Y. Li and A. Roorda, "Automated identification of cone photoreceptors in adaptive optics retinal images," *J. Opt. Soc. Am. A* **24**, 1358–1363 (2007).
2. B. Xue, S. S. Choi, N. Doble, and J. S. Werner, "Photoreceptor counting and montaging of en-face retinal images from an adaptive optics fundus camera," *J. Opt. Soc. Am. A* **24**, 1364–1372 (2007).
3. M. Lombardo, S. Serrao, P. Ducoli, and G. Lombardo, "Eccentricity dependent changes of density, spacing and packing arrangement of parafoveal cones," *Ophthalmic Physiol. Opt.* **33**, 516–526 (2013).
4. M. Lombardo, S. Serrao, and G. Lombardo, "Technical factors influencing cone packing density estimates in adaptive optics flood illuminated retinal images," *PLoS ONE* **9**, 7402 (2014).
5. S. S. Choi, N. Doble, J. L. Hardy, S. M. Jones, J. L. Keltner, S. S. Olivier, and J. S. Werner, "In vivo imaging of the photoreceptor mosaic in retinal dystrophies and correlations with visual function," *Invest. Ophthalmol. Vis. Sci.* **47**, 2080–2092 (2006).

6. J. L. Duncan, Y. Zhang, J. Gandhi, C. Nakanishi, M. Othman, K. E. Branham, A. Swaroop, and A. Roorda, "High-resolution imaging with adaptive optics in patients with inherited retinal degeneration," *Invest. Ophthalmol. Vis. Sci.* **48**, 3283–3291 (2007).
7. D. Merino, J. L. Duncan, P. Tiruveedhula, and A. Roorda, "Observation of cone and rod photoreceptors in normal subjects and patients using a new generation adaptive optics scanning laser ophthalmoscope," *Biomed. Opt. Express* **2**, 2189–2201 (2011).
8. M. Lombardo, M. Parravano, G. Lombardo, M. Varano, B. Boccassini, M. Stirpe, and S. Serrao, "Adaptive optics imaging of parafoveal cones in type 1 diabetes," *Retina* **34**, 546–557 (2014).
9. A. Pallikaris, D. R. Williams, and H. Hofer, "The reflectance of single cones in the living human eye," *Invest. Ophthalmol. Vis. Sci.* **44**, 4580–4592 (2003).
10. R. S. Jonnal, J. Rha, Y. Zhang, W. Gao and D. T. Miller, "In vivo functional imaging of human cone photoreceptors", *Opt. Express* **15**, 16141–16160 (2007).
11. J. Rha, B. Schroeder, P. Godara, and J. Carroll, "Variable optical activation of human cone photoreceptors visualized using a short coherence light source," *Opt. Lett.* **34**, 3782–3784 (2009).
12. R. Jonnal, J. Besecker, J. Derby, O. Kocaoglu, B. Cense, W. Gao, Q. Wang, and D. Miller, "Imaging outer segment renewal in living human cone photoreceptors," *Opt. Express* **18**, 5257–5270 (2010).
13. R. F. Cooper, A. M. Dubis, A. Pavaskar, J. Rha, A. Dubra, and J. Carroll, "Spatial and temporal variation of rod photoreceptor reflectance in the human retina," *Biomed. Opt. Express* **2**, 2577–2589 (2011).
14. M. Pircher, J. Kroisamer, F. Felberer, H. Sattmann, E. Götzinger, and C. Hitzenberger, "Temporal changes of human cone photoreceptors observed in vivo with SLO/OCT," *Biomed. Opt. Express* **2**, 100–112 (2011).
15. D. Rativa and B. Vohnsen, "Analysis of individual cone-photoreceptor directionality using scanning laser ophthalmoscopy," *Biomed. Opt. Express* **2**, 1423–1431 (2011).
16. P. Bedggood and A. Metha, "Variability in bleach kinetics and amount of photopigment between individual foveal cones," *Invest. Ophthalmol. Vis. Sci.* **53**, 3673–3681 (2012).
17. P. Bedggood and A. Metha, "Optical imaging of human cone photoreceptors directly following the capture of light", *PLoS ONE* **8**, e79251 (2013).
18. K. S. Bruce, W. M. Harmening, B. R. Langston, W. S. Tuten, A. Roorda, and L. C. Sincich, "Normal perceptual sensitivity arising from weakly reflective cone photoreceptors normal perceptual sensitivity of weakly reflective cones," *Invest. Ophthalmol. Vis. Sci.* **56**, 4431–4438 (2015).
19. P. Godara, R. F. Cooper, P. I. Sergouniotis, M. A. Diederichs, M. R. Streb, M. A. Genead, J. J. McAnany, A. R. Webster, A. T. Moore, A. M. Dubis, M. Neitz, A. Dubra, E. M. Stone, G. A. Fishman, D. P. Han, M. Michaelides, and J. Carroll, "Assessing retinal structure in complete congenital stationary night blindness and oguchi disease," *Am. J. Ophthalmol.* **154**, 987–1001 (2012).
20. J. T. McAllister, A. M. Dubis, D. M. Tait, S. Ostler, J. Rha, K. E. Stepien, C. Gail Summers, and J. Carroll, "Arrested development: High-resolution imaging of foveal morphology in albinism," *Vision Research* **50**, 810–817 (2010).
21. M. Land, R. Cooper, J. Young, E. Berg, T. Kitchner, Q. Xiang, A. Szabo, L. Ivacic, K. Stepien, C. Page, J. Carroll, T. Connor, and M. Brilliant, "Cone structure in subjects with known genetic relative risk for amd," *Optom. Vis. Sci.* **91**, 939–949 (2014).
22. B. Vohnsen, "Photoreceptor waveguides and effective retinal image quality," *J. Opt. Soc. Am. A* **24**, 597–607 (2007).
23. L. Ziccardi, D. Giannini, G. Lombardo, S. Serrao, R. Dell’Omo, A. Nicoletti, M. Bertelli, and M. Lombardo, "Multimodal approach to monitoring and investigating cone structure and function in an inherited macular dystrophy," *Am. J. Ophthalmol.* **160**, 301–312 (2015).
24. C. Miloudi, F. Rossant, I. Bloch, C. Chaumette, A. Leseigneur, J. A. Sahel, S. Meimon, S. Mrejen, and M. Paques, "The negative cone mosaic: A new manifestation of the optical stiles-crawford effect in normal eyes," *Invest. Ophthalmol. Vis. Sci.* **56**, 7043–7050 (2015).
25. R. S. Jonnal, O. P. Kocaoglu, Q. Wang, S. Lee and D. T. Miller, "Phase-sensitive imaging of the outer retina using optical coherence tomography and adaptive optics," *Biomed. Opt. Express* **3**, 104–124 (2012).
26. J. Jacob, M. Paques, V. Krivosic, B. Dupas, A. Couturier, C. Kulcsar, R. Tadayoni, P. Massin, and A. Gaudric, "Meaning of visualizing retinal cone mosaic on adaptive optics images," *Am. J. Ophthalmol.* **159**, 118–123 (2015).
27. S. A. Burns, S. Wu, F. Delori and A. E. Elsner, "Direct measurement of human-cone-photoreceptor alignment," *J. Opt. Soc. Am. A*, **12**, 2329–2338 (1995).
28. A. Roorda and D. R. Williams, "Optical fiber properties of individual human cones," *J. Vis.*, **2**, 404–412 (2002).
29. W. Gao, B. Cense, Y. Zhang, R. S. Jonnal and D. T. Miller, "Measuring retinal contributions to the optical Stiles-Crawford effect with optical coherence tomography", *Opt. Express*, **16**, 6486–6501 (2008).
30. B. Vohnsen, "Directional sensitivity of the retina: A layered scattering model of outer-segment photoreceptor pigments," *Biomed. Opt. Express* **5**, 1569–1587 (2014).
31. L. Mariotti and N. Devaney, "Performance analysis of cone detection algorithms," *J. Opt. Soc. Am. A* **32**, 497–506 (2015).
32. M. N. Muthiah, C. Gias, F. K. Chen, J. Zhong, Z. McClelland, F. B. Sallo, T. Peto, P. J. Coffey and L. da Cruz,

- “Cone photoreceptor definition on adaptive optics retinal imaging”, *Br J Ophthalmol*, **98**(8), 1073–1079 (2014)
33. G. Ramaswamy and N. Devaney, “Pre-processing, registration and selection of adaptive optics corrected retinal images,” *Ophthalmic Physiol. Opt.* **33**, 527–539 (2013).
 34. S. J. Chiu, Y. Likhnygina, A. M. Dubis, A. Dubra, J. Carroll, J. A. Izatt, and S. Farsiu, “Automatic cone photoreceptor segmentation using graph theory and dynamic programming,” *Biomed. Opt. Express* **4**, 924–937 (2013).
 35. G. Wolberg and S. Zokai, “Robust image registration using log-polar transform,” in *2000 International Conference on Image Processing*, (IEEE, 2000), vol. 1, pp. 493–496.
 36. L. Mariotti and N. Devaney, “Cone detection and blood vessel segmentation on AO retinal images,” in *IRISH MACHINE VISION & IMAGE PROCESSING Conference proceedings 2015*, R. Dahyot, G. Lacey, K. Dawson-Howe, F. Pitié, and D. Moloney, eds. (Irish Pattern Recognition & Classification Society, 2015), pp. 126–128.
 37. H. W. Babcock, “The possibility of compensating astronomical seeing,” *Publications of the Astronomical Society of the Pacific* **65**, 229–236 (1953).
 38. S. Panda-Jonas, J. B. Jonas, and M. Jakobczyk-Zmija, “Retinal photoreceptor density decreases with age,” *Ophthalmology* **102**, 1853–1859 (1995).
 39. P. Godara, A. M. Dubis, A. Roorda, J. L. Duncan, and J. Carroll, “Adaptive optics retinal imaging: emerging clinical applications,” *Optom. Vis. Sci.* **87**, 930 (2010).
 40. M. Lombardo, S. Serrao, N. Devaney, M. Parravano, and G. Lombardo, “Adaptive optics technology for high-resolution retinal imaging,” *Sensors (Switzerland)* **13**, 334–366 (2013).
-

1. Introduction

Since the introduction of adaptive optics (AO) into the field of retinal imaging, the photoreceptor mosaic can be imaged at a resolution high enough to resolve individual photoreceptors in patients. Most studies have focused on the analysis of the spatial distribution of the cones [1–4], showing how the characteristics of the cone mosaic can vary between subjects, who are either healthy or who present retinal disease [5–8].

In addition to their number and position, one of the most noticeable features of the photoreceptors is the spatial variability of their reflectance, which has been clearly detected with all AO imaging modalities [9–18]. From early observations, it has been shown that the cones change their reflectance with time even in healthy retinas [9]. As recently highlighted, in some clinical cases the cone reflectance is the only apparent feature of the cones that distinguishes a healthy cone mosaic from a mosaic with altered functionality, but unaltered spatial organization [19]. Nevertheless, the investigation of differences in cone reflectance between pathological and healthy retinas is still limited to a few isolated studies [20,21]. In addition, studies have demonstrated that cones in the central retina may vary their sensitivity or pointing direction in order to compensate for the eye’s internal aberrations [22] or deterioration in the nearby cone’s functionality [23] and that cones in the peripheral retina may vary their pointing direction depending on the position of the center of the illumination pupil [24]. The use of AO Optical Coherence Tomography (OCT) has also provided information on the dependence of the reflectance on depth in the inner cone interfaces, leading for the first time to a 3D characterisation of the cone reflectance [14]. Phase-sensitive implementations of spectral-domain OCT were also developed, leading to a further improvement in OCT axial resolution [25].

For the above reasons, understanding of the cone reflectance variability could provide a unique insight into the physiology or pathophysiology of these cells and give functional information that is complementary to the structural mosaic organization described by spatial metrics [19,26]. At the same time, it is necessary to investigate whether the temporal variability of cone reflectance may influence the study of mosaic spatial metrics.

The variability of cone reflectance can be analysed in two ways: between different cones or on each cone at different times. It has been shown that the changes in reflectance occur independently between the cones [9] and that the cones change their brightness on time scales ranging from milliseconds [10, 17] and seconds [11, 15, 16] to hours [9, 12, 13], days [14], months or years [18].

Using an AO-Scanning Laser Ophthalmoscope (SLO)-OCT [14], it was possible to deter-

mine that the fluctuations in brightness due to the outer segment renewal are the sum of the reflectance fluctuations in the cone inner interfaces, and that they are independent of each other. A common aspect of previous studies is that the cone reflectance has been analyzed for short time periods, usually not exceeding one day, with high-frequency time observations. Another characteristic of the previous studies is that the windows within which the cones have been analysed were small (with maximum size being 0.94×0.70 degrees in [14]), and so the results may have been limited with regards to both the number of cones and the low-frequency spatial variations. The only long-term study [18] used an AO-SLO system and was specifically focused on the functionality of ten poorly reflective cones and therefore was not intended to be a survey of cone reflectance in AO-SLO images of the cone mosaic. Investigation of the cone reflectance in different retinal areas and over long time periods using an AO flood illumination camera is therefore lacking in the literature.

It has already been observed that the position of the light source in an AO flood illumination system has an influence on the reflectance of the cone mosaic [9,24,27–29], and this property has been used to study the angular tuning of single cones [15,28,30]. As the performance of the most commonly used cone detection algorithms depends on the quality of the images to which they are applied [31], it is also possible that the position of the light source itself affects not only the reflectance of the cones but also their detection and the subsequent estimation of the mosaic metrics. From a technical point of view, it would be useful for the operators of commercial AO flood illumination systems to know if there is a substantial difference in the detection results when changing the position of the light source within the central pupil area, which is the area commonly used for collecting high-quality AO images of the cone mosaic. Based on a thorough literature search, we are not aware of studies that examine the influence of the light source position on automated cone detection as a separate topic from the reflectance and angular tuning of the cones.

The aim of this work is to develop an automated approach for investigating the cone reflectance variability of a single eye. The reflectance of the cones was evaluated over time scales ranging from minutes to years, and for large areas of the retina ($\geq 2.0 \times 2.0$ degrees) at two different retinal eccentricities using an AO flood illumination retinal camera. Our purpose is to understand and create a baseline for the comparison of data acquired on the same subject over long time scales. The ability to identify the same cones on different images over time could prove very useful in the analysis of retinal pathologies where the deterioration of individual cones can be observed [23], in which case an estimation of the performance of an automated method to identify and match the cones in a healthy eye is needed. We test here if the cone detection and identification in multiple images is affected by their time separation. In addition, we determine whether the displacement of the light source within 0.35 mm off the pupil center in a commercial AO camera, which is the farthest location from the pupil center used by clinical operators to acquire high-quality images of the cone mosaic, affects the automatic identification and matching of the cones. If this proves true then restrictive requirements on the data acquisition would be necessary during the follow-up of a patient.

2. Methods

2.1. Image acquisition

The research procedure described in this work adhered to the tenets of the Declaration of Helsinki. It is part of a study protocol approved by the local ethics committee (Azienda Sanitaria Locale Roma A, Roma, Italy), in which all the subjects recruited gave written informed consent after a full explanation of the procedure. The present data set consists of 61 images acquired with a commercial AO retinal camera (rtx1, Imagine Eyes, Orsay, France) on a healthy subject (female, 27 years old in 2015, -3.75 dioptres, axial length 24.38 mm) over a time span

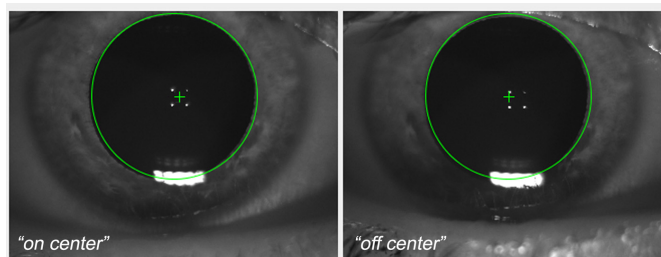


Fig. 1. Screen shot of the anterior segment image of the viewer interface of the AO flood illuminated retinal camera showing the placement of the entry beam (green cross) in the right eye of the subject. The four white dots are the first Purkinje images of the cornea, which are taken by the AO camera operators as reference points for collecting high-quality images of the photoreceptor mosaic. The “on-center” represents the illumination position passing through the center of the pupil; in the “off-center” position, the illumination is 0.35 mm temporal from the pupil center. The corneal reflections allow images of the retina to be captured using the same illumination position over time.

of three years, from 2012 to 2015. Each imaging session was conducted after dilating the pupil with one drop of 1% tropicamide. During imaging, fixation was maintained by instructing the subject to fixate on the internal target of the instrument moved by the investigator. A sequence of 40 frames was acquired by illuminating a retinal area subtending 4 degrees visual angle in the right eye of the subject with an illumination source of $\lambda = 850$ nm, $\Delta\lambda = 35$ nm that covered the whole pupil. The images were acquired at 2.5 degrees and 4.0 degrees temporal from the fovea of the right eye. The two eccentricities were chosen to be a compromise between the resolution limit of the instrument, which does not allow cones to be resolved too close to the fovea (i.e. closer than 1 degree), and the presence of rods, which alter the cone relative spacing enough to be detectable by the rtx1 when further than 5 degrees [32].

The time between the images ranged from 45 minutes to 3 years at 2.5 degrees and from 45 minutes to 4 months at 4.0 degrees. The images were divided into sub-sets according to their time separation. The final division allowed us to analyse the changes in the cone reflectance over time ranges of minutes, hours, days, months and years. All images (with the exception of the 24 May 2012, 30 June 2013 and 26 May 2015), were acquired focusing the light source at two different positions, on the pupil centre (“on center” illumination) and 0.35 mm temporal (“off center” illumination) from the pupil center (Fig. 1). No difference in image quality was found between the temporal and other meridians (data not shown). The data set and the sub-set division is available in [Data File 1](#) of the supplementary materials.

2.2. Image pre-processing and processing

Each image was obtained by processing 40 raw 16-bit frames acquired by the AO camera with the procedure described in Ramaswamy and Devaney [33]. A new approach was used for background correction; as one of the objectives of this study was to analyse the cone reflectance, we corrected for the background using the same flat-field image for all the raw frames. The background correction is necessary in order to correct for non-uniform illumination of the retina. In this case, the use of the same flat-field ensured that the intensity values between all the images could be compared and that the intensity distribution of the images, and therefore of the cones, is not altered by non-uniform illumination. A preliminary analysis was performed on the low-frequency profile of the raw unregistered frames, which confirmed that the non-uniform illumination profile did not depend on the eccentricities or the time and the difference between the images and the flat field used was less than $\pm 7\%$ in all cases. After this analysis, the flat-

field image was obtained by averaging a total of 240 raw frames acquired at 1.0, 2.5 and 4.0 degrees eccentricities from the fovea. Additional frames were acquired at 1.0 degree only for the flat-field estimation as this eccentricity would not have been suitable for the cone analysis (section 2.1). The frames were averaged unregistered, so that the major retinal structures, such as blood vessels, are averaged out, as in previous works [12, 16]. All the raw frames were divided by the same flat-field image and then registered in order to produce the final images. The method used for background correction does not have any impact on the cone detection performance, as the first step of the cone detection algorithm that we used [34; section 2.3] is based on the localization of regional maxima in the images and the presence of the maxima is not influenced by low-frequency spatial variation (Fig. 2).

The final images were registered for each retinal location in order to analyse and compare the same area of the retina over time. This registration process was performed in two steps; coarse registration and fine registration. Firstly, the images were coarsely corrected for rotation using Log-Polar transformation followed by Normalized Cross Correlation [35] and for translation using Normalized Cross Correlation only. Images were finely registered for rotation and translation by identifying and tracking a limited selection of the cones that remain detectable across all the images, as in [33]. The use of bright cones assured the maximum possible accuracy of the process. The use of peak tracking assured that the registration was not affected by retinal features other than the local cone peaks, which change their intensity but retain their relative position along the time series.

The registration process returned two series of registered images with areas of 2.0×2.8 degrees (0.61×0.83 mm) and 2.3×2.6 degrees (0.70×0.78 mm) at 2.5 and 4.0 degrees eccentricity from the fovea respectively, which were acquired at different times and with two different light source positions (Fig. 3 and 4), except for three images obtained at 2.5 degrees, which were obtained with on-center illumination only.

The area at each eccentricity was the maximum area common to all images after registration.

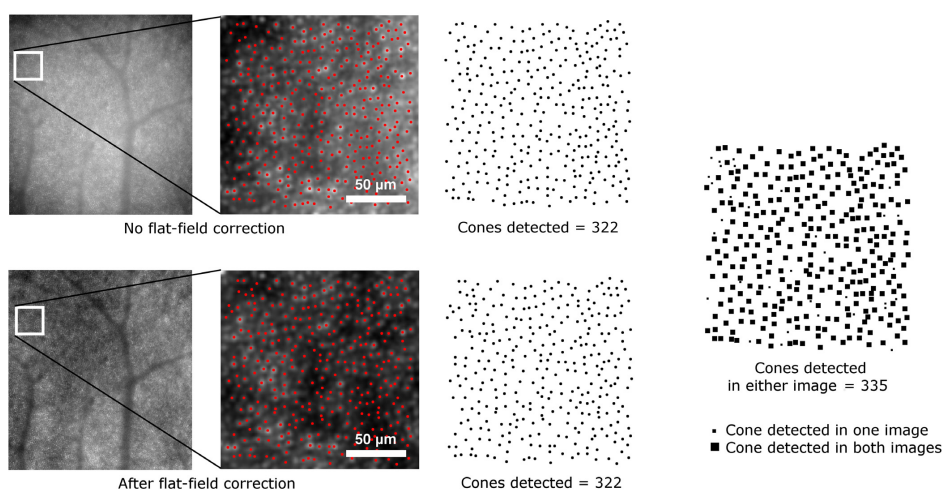


Fig. 2. Example of detection on the same portion of two images obtained from the same frame series. In the upper image, the frames were not corrected for the flat-field prior to registration, in the image below the frames were divided by the flat-field image and then registered. The cone map on the right is the sum of the two cone maps resulting from the separate detections on the two images. The difference between the combined cone map and the two individual cone maps is less than 4% of the cones.

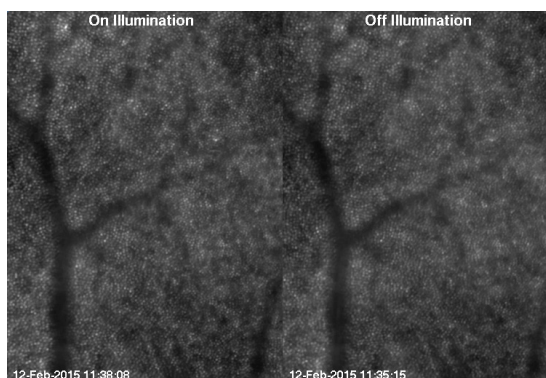


Fig. 3. One frame of the time series at 2.5 degrees after registration and normalization (Visualization 1). An overview of the data set and the sub-set division is available in Data File 1.

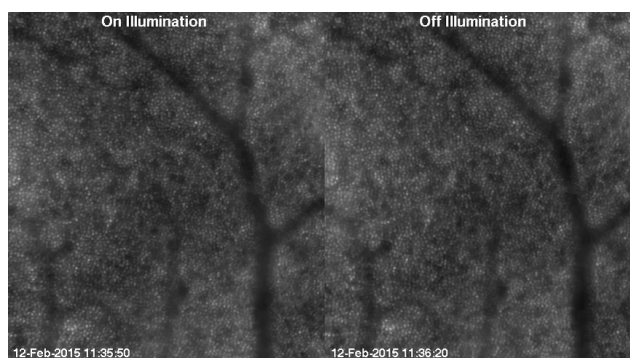


Fig. 4. First frame of the time series at 4.0 degrees after registration and normalization (Visualization 2). An overview of the data set and the sub-set division is available in Data File 1.

The right side of the series at 4.0 degrees and the left side of the series at 2.5 degrees can be seen to overlap. However, we chose to analyse them separately in their entirety in order to test our method for the analysis of large retinal patches. Before proceeding with the reflectance analysis (section 2.4), all the images were normalized so that images collected at the same eccentricity had the same total intensity, i.e., the sum of all the pixel intensities. This was carried out by dividing each 16-bit image by its total intensity and then multiplying by the total number of pixels:

$$I_{norm} = \frac{I}{\sum_{x=1}^M \sum_{y=1}^N I(x,y)} \cdot MN \quad (1)$$

where M is the number of pixels on the horizontal axis and N is the number on the vertical axis. In this way, all the images had a total intensity that is proportional to their area and the intensity values between the two eccentricities and the different time scales images could be compared. Furthermore, this normalization can be useful to investigate if the image intensity or the cone intensity histograms have means that are displaced with respect to the mean value of the pixels, which with this normalization is 1.

Before applying the detection algorithm, we selected the area to be analysed. A vessel segmentation process was performed to exclude the region on which the retinal blood vessel shad-

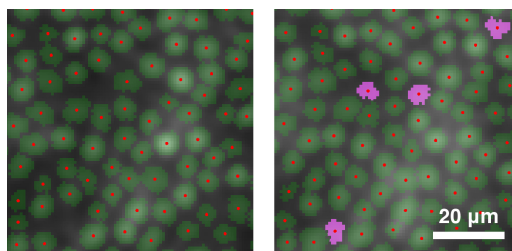


Fig. 5. Detail of detection and segmentation of cones at the same location of a single image (left) and the average image (right). The cones that are detected and segmented on the average image but not on the single image are shown in pink.

ows are projected [18]. As cone size and density change as a function of distance from the fovea, cone density has to be measured as a local value and it is common practice to select small windows, which do not include blood vessels, on the image of the cone mosaic. The purpose of segmenting the blood vessels is not to skip the selection of windows on the image, which is necessary, but to allow for both an automatic division of the image into windows and to increase the area that can be analysed. In fact, by automatically excluding the area occupied by the blood vessels, all the remaining area of the image can be analysed without further manual intervention.

We have used here a custom method developed for the segmentation of blood vessels on high resolution photoreceptor layer images, which has been described in a previous work [36]. The vessel segmentation was performed only once for each retinal location, using the average of all the registered images at that location. In this way, the area to be analysed was the same for all the images at each location.

2.3. Cone detection

Before starting the detection process, we doubled the size of the images using bicubic interpolation in order to improve the final detection performance [31]. The size on the retina of the upsampled pixels was $0.8\mu\text{m}$ on an emmetropic eye. We averaged all the images registered at each retinal location in order to have two images of the cone mosaic that can be taken as references. The detection was performed using the Chiu et al. algorithm [34], which detects the cones and segments their shape, separating them from the background. It was carried out on all the images as well as on the average images. From previous work [31], we know that the typical mean percentage of cones correctly detected by the Chiu et al. algorithm on a single image at the same eccentricities is 97%. Since the average images have more cones than any single image of the series, the algorithm performed notably better, detecting also the cones that were missed in the images because they were too faint (Fig. 5) and 97% can therefore be taken as a lower limit for the accuracy. Because of this, we considered the results on the average images as the closest estimate of the “ground truth” data available for the cone coordinates. Two masks excluding the vessels were applied to the detections, both on the images and on the average images, so that only the cones outside the vessels were analysed.

We calculated cone density (cones/ mm^2) in non-overlapping sampling windows of 200×200 pixels, which corresponds to approximately 0.16×0.16 mm on the retina, covering the whole image area. When detecting the cones and segmenting their shape, we excluded the cells for which the segmentation was not entirely inside the window borders or for which the central cone coordinates fell inside the segmented vessels. We compared density estimates for the two different illuminations with Bland-Altman plots in order to determine if the position of the light source significantly affects the identification of cones. In addition, the estimates of cone density

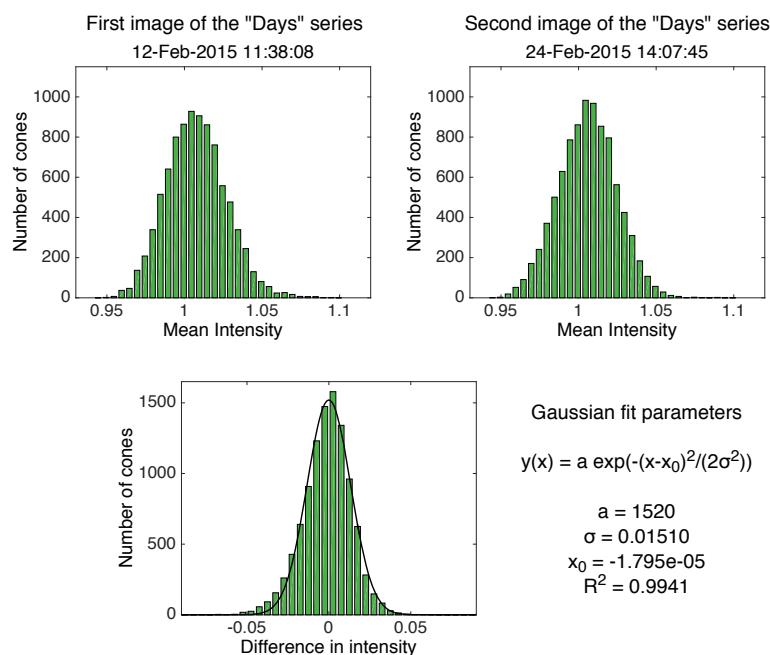


Fig. 6. Top row: histograms of the cone intensity in the first and second image of the “Days” series at 2.5 degrees. Bottom: histogram of the difference between the intensity of the cones in the second and the first image fitted with a Gaussian distribution, for which the parameters are shown on the right. These histograms are shown as representative of the results on all the images.

on the single images were compared to the results on the average images.

2.4. Cone matching

In order to track the individual cones on multiple images over time, we performed a “cone matching” procedure. Two cone detections on two different images are taken to correspond to the same cone if they are closer than a defined tolerance distance. If more than one cone is inside the tolerance distance in the second image, then that which is closest to the cone in the first image is taken as the match. Since the physical size of the cones varies as a function of the distance from the fovea, using the same tolerance distance for the whole image would lead to inaccurate matching. For this reason, the tolerance distance was defined individually for each cone as half of its equivalent diameter (i.e., the diameter of a circle with the same area as its segmentation) on the reference image. The cone matching was performed between the images from the two series at 2.5 and 4.0 degree eccentricities and the average image.

2.5. Cone reflectance

The reflectance of the cones was investigated after image normalization, as described in section 2.2. The segmentation of the cones given by the algorithm on the average images was used to study how the reflectance of the cones changes with time. In general, the cone intensity can be measured either as the maximum or the mean intensity value inside the segmentation profile for each cone. After a preliminary comparison that showed minimal differences between the two methods (data not shown), we preferred to use the mean value (i.e., the sum of the intensity pixel values divided by the number of pixels). In all the images we used the segmentation profiles of the average images, insuring that cones with low intensity values (Fig. 5) are also included in

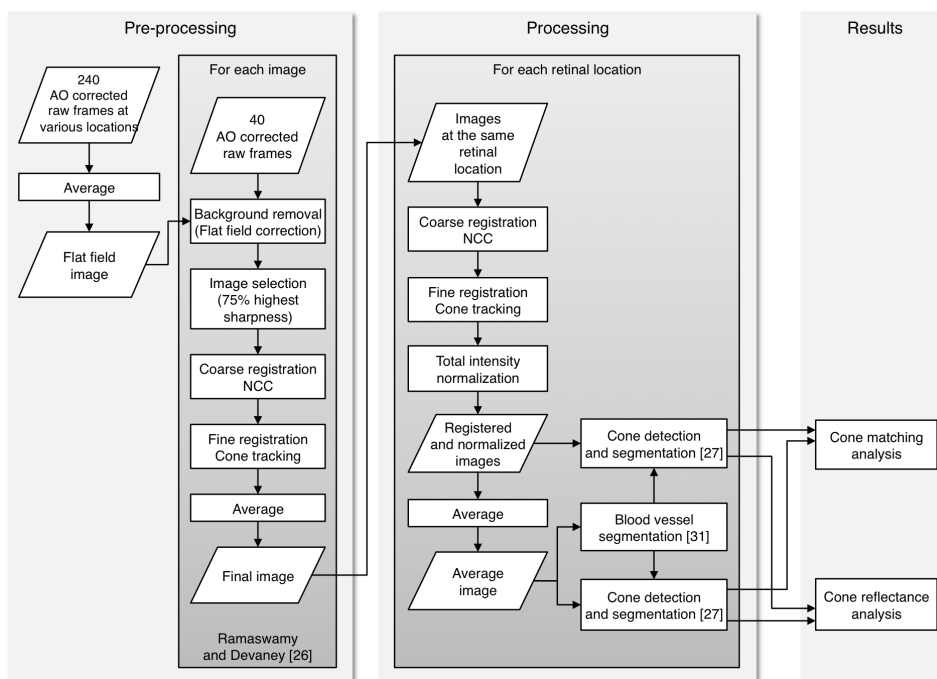


Fig. 7. Flow chart of the entire analysis process. The processing algorithms enclosed in the left and right grey boxes were performed for all the images and for the two series of images at the two retinal locations respectively.

the analysis.

In order to determine if there is any pattern in cone reflectance with time, we calculated for each image the difference in intensity of the cones with respect to the intensity of the same cones in the first image of each time series (e.g., the intensity of each cone in the images of the “Days” series was subtracted from its intensity in the first “Days” image, see Fig. 6). The differences in intensities for each image presented a normal distribution, and we fitted the data with Gaussian curves. For the purpose of clarity, a flow chart of the entire analysis process is shown in Fig. 7.

3. Methodological validation

In this section we provide a validation of the presented analysis methodology. Cone detection and matching are performed on pairs of images acquired with different positions of the light source, and the results are compared to the average images at the corresponding retinal locations.

3.1. Cone detection

The agreement of cone density estimates between the single and average images of the cone mosaic was measured using 5 sampling windows of the grid at each retinal eccentricity (Fig. 8). We selected a number of windows that are distributed over the images and include regions both with and without vessel shadows (the shadowed areas were excluded automatically from analysis, as described in section 2.2).

The two different illumination methods were compared in the estimation of the cone density with a Bland-Altman plot (Fig. 9). The analysis was carried out on the same 5 windows at

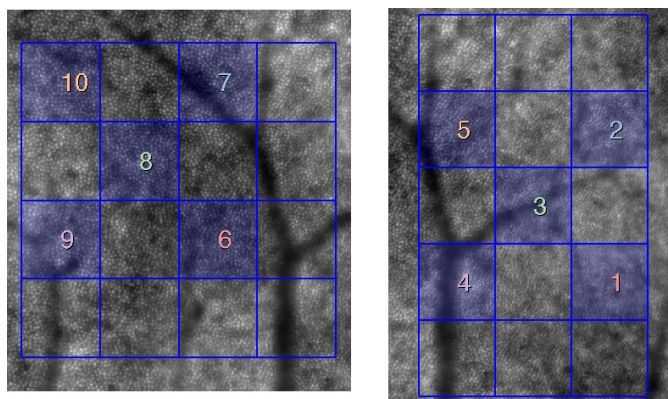


Fig. 8. Average images at 4.0 degrees (left) and 2.5 degrees (right) with the grid of 200×200 pixel ($160 \times 160 \mu\text{m}$) windows in the image series in which the parameters were calculated. The selected windows are highlighted and marked with numbers. The same numbers are used in the plot legend in Fig. 9.

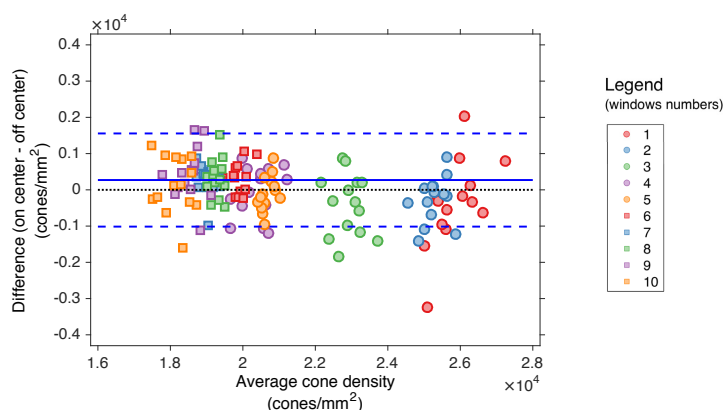


Fig. 9. Bland-Altman plot of the cone density at 2.5 (circles) and 4.0 degrees (squares) in selected windows. The plot shows the mean of the differences (continuous lines) and ± 1.96 SD (dashed lines) of the cone density between the two illumination positions. The numbers represent the sampling windows shown in Fig. 8.

each eccentricity, as described above. The points on the plot represent the comparison of the measurements between 14 pairs of “on-center”-“off-center” images acquired close together in time.

The average of the cone density as measured on “on-center” and “off-center” images was also compared to the “ground truth” values on the average images at the two retinal locations. The differences in cone density between all single images and the average images were within $\leq 9\%$ in all sampling windows. The fact that the detection performed equally in all the sampling windows across the image positively confirms that the analysis of large retinal patches can be performed. If the isoplanatic area was smaller than the field of view then this would have resulted in the cone detection performance decreasing as a function of distance from the center of the images. This might be expected from previous studies of the isoplanatic angle [37], but was not evidenced in this work.

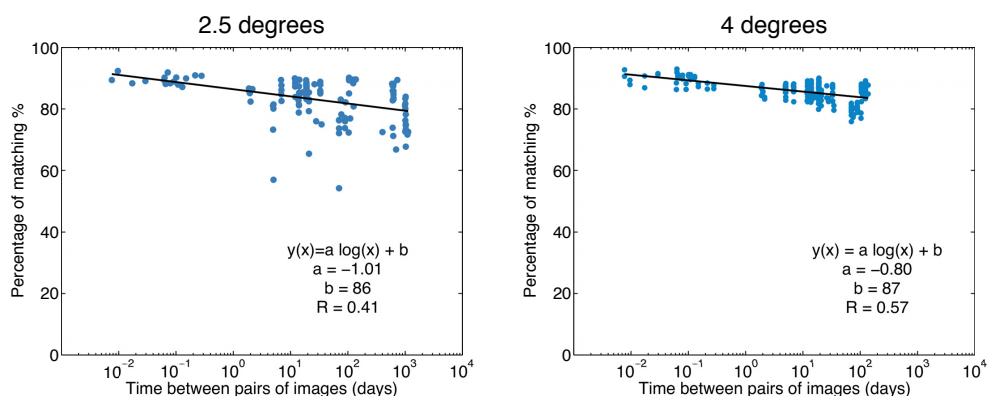


Fig. 10. Matching of cones performed on pairs of images as a function of the time between the two images, at 2.5 degrees and at 4.0 degrees. The x-axis is in logarithmic scale. The plots show how the percentage of matching decreases as the time increases with a logarithmic trend (linear fits on logarithmic scale).

3.2. Cone matching - “on center” / “off center” images

The percentage of the cones on the average image that were matched with cones in the single images ranged between 81% and 94% at 2.5 degrees and between 89% and 97% at 4.0 degrees, in both cases compatible with the detection performance of the algorithm. The mean and standard deviation of cones successfully matched was $89.8\% \pm 2.8\%$ at 2.5 degrees with on-center illumination, while at the same eccentricity the off-center percentages were $91.7\% \pm 1.3\%$. At 4.0 degrees, the on-center percentages were $94.6\% \pm 1.3\%$ on-center and the off-center percentages were $95.5\% \pm 0.4\%$ (the values for all the images are available in [Data File 2](#) of the supplementary materials).

The matching percentages improved as the distance from the fovea increased, due to the increased relative diameter of the cones and the increased distance between the neighbours. We performed the Student’s t-test on paired “on center” and “off center” illumination observations in order to establish if the matching performance between the two illumination methods is significantly different. The result is that there is evidence of a difference between the two methods ($p=0.04$ at 2.5 degrees and $p=0.02$ at 4.0 degrees), with off-center illumination performance being 2% better on average at 2.5 degrees and 1% better at 4 degrees. Even if the mean difference between the two illumination methods is significant, their absolute value is not clinically relevant.

4. Results

4.1. Cone matching - time scales

The matching analysis presented in the following paragraphs was performed only on the images with on-center illumination in order to analyse the matching percentages over all the possible time ranges. We determined how many cones on the average image could be successfully found in a sequence of images. The percentage of cones on the average image that can be successfully detected and tracked over 3 years and on all the 17 images drops to 40% at 2.5 degrees. At 4.0 degrees, the percentage over 4 months and on all 15 images drops to 64%. The percentage decreases as the time separation and accordingly the number of images analysed increases.

Figure 10 shows the results of matching cones performed on pairs of images as a function of the time separation between the two images. In this case, the matching was not performed with the average image but only considering two images at a time, in order to reproduce the case of

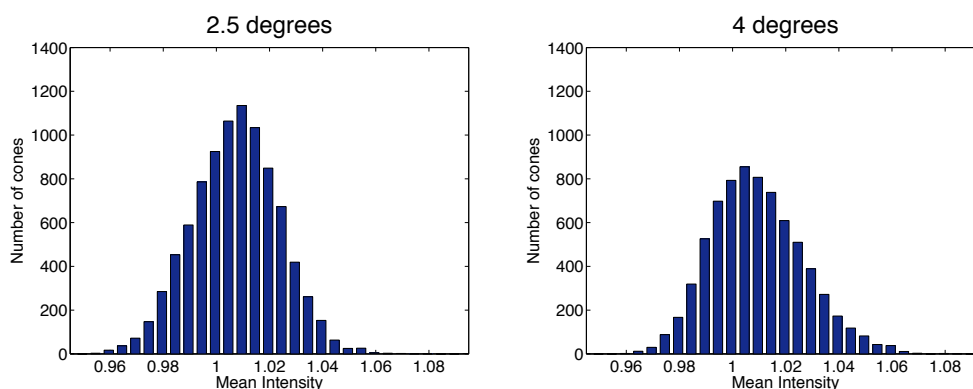


Fig. 11. Histogram of the mean cone intensity (as measured inside the segmentations) on the average images at 2.5 degrees and 4.0 degrees. The intensity values are measured after the total intensity normalization.

a clinician with only two images available. All the possible combinations of image pairs have been tested. The plots show how the percentage of matching decreases as the time separation increases. When two images are acquired minutes or hours apart, on average 90% of the cones can be matched. As the time separation increases, the matching worsens on average to 80% when two images are 3 years apart.

The matching at 2.5 degrees presents a few low matching image pairs. The poor matching for these image pairs was found to be attributed to one specific image (26 May 2015), which showed signs of motion blur. The motion blur was responsible for a greater number of missed matches, as it altered the estimation of the cone positions.

4.2. Cone reflectance

The histograms of the measured cone intensities on all the images had an approximately Gaussian shape (goodness of fit $R^2 \geq 0.99$ for all images) slightly skewed towards higher intensity (skewness values between 0.01 and 0.64), showing a limited excess of bright cones over dim cones. The means of the cone intensities were 1.0072 ± 0.0001 at 2.5 degrees and 1.0093 ± 0.0001 at 4.0 degrees and in all cases greater than 1.0053. This is consistent with the mean cone intensity being greater than the average image intensity, which with our normalization is set to 1. The averages of the standard deviations of the distributions were 0.0192 ± 0.0001 at 2.5 degrees and 0.0201 ± 0.0001 at 4.0 degrees. Although the differences in mean intensities between the two retinal eccentricities were statistically significant ($p < 0.001$; ANOVA), all the values were within a small range, as can be seen by the small standard deviations. The cone intensity distributions are well represented by the histograms obtained on the average images (Fig. 11), showing the limited skewness of the distributions.

Histograms of the difference in intensity between cones on pairs of images were well fitted by Gaussian distributions. The centers of the distributions were all included in a range between -0.0021 and 0.0011, though their differences were statistically significant ($p < 0.001$; ANOVA). Nevertheless we can assume that the Gaussian distributions are centered on zero as their standard deviations were ten times greater than the difference from zero. Also, the displacement of the centers with respect to the zero are not dependent on time. The standard deviation of the difference in intensity as a function of time is plotted in Fig. 12, where it can be seen that the variation in cone reflectance increases logarithmically with time. This result is surprising as it implies long term correlation in the cone reflectance. We will consider the implications of this result in the following Discussion.

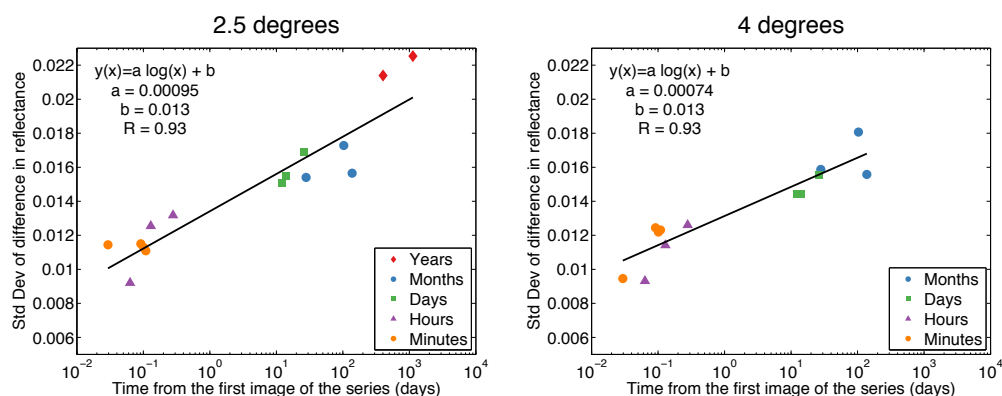


Fig. 12. Standard deviation of the difference in cone reflectance as a function of time at 2.5 degrees and 4.0 degrees. The x-axis is in logarithmic scale. The standard deviation is calculated from the Gaussian fit of the histograms of the intensity difference of all the cones with respect to their intensity value in the first image of the different time series. It can be seen that the variability of cone reflectance increases logarithmically with time (linear fits on logarithmic scale). The variation in cone reflectance between images acquired more than one year apart is more than the double the variation observed on the cone mosaic on the same day.

5. Discussion

Our results suggest that identification and tracking of cones over time is not altered significantly by the precise positioning of the light source, when this is closer than 0.35 mm from the pupil center (section 3.1 and section 3.2). This can be beneficial to clinicians who use commercial AO flood cameras if the purpose of an imaging session is cone detection and estimation of cone density, as the operator knows that he does not need to center the source exactly. We found that simple tracking of a single cone becomes harder as the number of images and the time separation increases (Fig. 10). This phenomenon could be related to several factors, including the presence of faint cones (or rods) in each image, some of them tended also to disappear completely and then reappear again over time, regardless of the time range between the images. Dim cones are more likely to be missed and the cones that are not detected are different in each image, making it harder to follow one cone through all the images. However, we cannot exclude that some cones may have died or lost their function over three years follow-up, thus directly influencing cone matching [38]. Another possible cause for a missed match was when the cones were detected farther apart than the tolerance distance. This type of missed match can be caused by image registration errors. Even if the registration was performed in order to correct for displacements smaller than the cone size, we acknowledge that residual translational or rotational errors might affect the matching. However, this should not be the cause of the time dependence of the matching, but rather cause isolated mismatches (e.g. the poor matchings at 2.5 degrees), and the same will be true for the differences in intensities.

In recent years, there have been several studies focused on observation of the reflectance of living cones [9, 11–16, 18], and on its modelling, suggesting how the cone reflectance could be due to constructive interference of scattered light which increases with penetration depth in the cone outer segment [30], but the origin of its variability is still not fully understood. The reflectance studies have been performed with all AO imaging modalities, including AO-SLO [11–13, 16], AO-OCT [14] and flood-illuminated AO cameras [9, 17, 24]. The most common explanation so far for the cone reflectance variability of the order of an hour is the disc renewal process [9], which is thought to be the cause of both change in the outer segment length,

observable through interference produced with a long-coherence light source AO-SLO [12], and in the refractive index at the interface between the inner and the outer segment, observable also with a short-coherence light source AO-SLO-OCT [14].

From our results, there is no evident pattern that regulates the time variation of cone reflectance in AO flood illumination images of the cones in the central retina. Over the short as well as the long time periods, the majority of cones showed little change in reflectance while others greatly increased or decreased their reflectance, resulting in an approximately normal distribution of the difference in reflectance. From the plots in Fig. 12 we see that the variation in cone reflectance that can be expected to be seen in the same cones increases with time, and as a result their identification in two images becomes more difficult as the time separation increases (Fig. 10). The variation in cone reflectance was found to increase logarithmically with time; this indicates that the intensity fluctuations are strongly correlated on timescales shorter than a day, becoming less correlated with time, but do not appear to be completely independent even on the longest timescales. This suggests the presence of some long-term trends in the cone reflectance could be related to changes in cone directionality or other cellular sources, as discussed previously [14]. The fact that the intensity fluctuations after hours are more pronounced than minutes was already observed by Pircher et al. [14], and here we extend the result to months and years separation. Since the coherence length for our light source was $L_c = (2 \ln 2 \lambda^2) / (n \pi \Delta \lambda) = 6.37 \mu\text{m}$ (calculated as in [10]) and the cone outer segment length is greater than $20 \mu\text{m}$, we can exclude that the outer segment length is the source of the variability observed by us, as well as in [14]. The change in the refractive index at the inner segment-outer segment interface caused by the generation of new discs, a possible explanation for the reflectance variability that was pointed out in the cited study, could therefore be the source of the variability observed by us as well. Changes in the composition of the outer segments-RPE interface due to the migration of melanosomes or melanogenesis during disc shedding have been also considered to explain the changes in reflectance [9].

Nonetheless, the physiological processes that cause the changes in reflectance to increase with time separation still needs to be identified. Either waveguiding or cone pointing may change over time [9, 18]; for example, the reflections within a properly waveguiding cone may be reduced because the reflective interfaces within the cone (either between inner and outer segments or between the posterior tips of the outer segments and RPE) change in some way. In addition, the light coupled into a single cone can be either transmitted or absorbed differently over time and some cones may point at different points on the pupil over long time scales. Specifically related to imaging of the cones with an AO flood-illuminated camera, spatial variations may arise also in the inner retina, such as those caused by blood vessels, which influence the reflectance of cones. However, we automatically excluded the area of the cone mosaic occupied by the blood vessels, reducing the effects of stray light on cone reflectance and making it easier to study the reflectance changes that are intrinsic to cones.

The two representative entry pupil positions used in this work have been chosen in order to understand the influence of the illumination positions commonly used to acquire high-quality images of the cone mosaic in clinic. Since oblique incidence of light increases the amount of light which traverses more than one outer segment before being absorbed, this could affect the overall image quality of the cones and hence their identification with automated algorithms. However, Vohnsen [30] has previously shown that this can only have an impact when the angle of incidence on the retina is greater than 7 degrees corresponding to a pupil entrance displacement of 2.7 mm. In previous work [24], the reflectance of the cones in AO flood-illuminated images of the retinal periphery has been shown to be greatly influenced by large displacements of the entry pupil. It is well known that the cones have relatively narrow angular reflectance functions, returning much more of the incident light towards a point near the center of the pupil

than towards points farther away from the center. This phenomenon is closely related to the Stiles-Crawford effect [9, 27–29], which describes the variation in the visual effectiveness of light entering through different locations in the pupil.

In this study, we used a commercial AO flood-illuminated camera; with the method developed for processing of these images, which is largely automated, it is possible to establish an analysis routine that can be applied in clinics as part of a research procedure for assessing the health of the cone mosaic in patients. Changes in cone reflectance have already been associated with retinal conditions [39, 40] and with this work we are moving towards the identification of additional properties of the cones, which are complementary to their spatial organization.

Limitations of the current work include the lack of a measure of the absolute reflectance of cones since processing of flood-illuminated AO images included normalization in order to compare images acquired at different times and under different conditions, which unavoidably altered photoreceptor reflectance. In addition, we only studied one subject. Another limitation could be the automatic detection of the cones. Even if we used the algorithm with the best performance and that best suited our needs, the detection process cannot be regarded as perfect [31]. Nonetheless, we note here that the analysis of such a large amount of data would not have been possible using manual cone detection only, and one of our purposes is to move towards the automation of the analysis process.

With the methodology developed for the cone detection and area selection, we plan to extend the analysis of the changes over time in the cone mosaic to the metrics related to the cone spatial distribution (density, regularity metric and nearest neighbour distance). Moreover, we plan to carry out this analysis procedure on healthy and diseased eyes, in order to identify suitable markers for the identification of retinal conditions. Future work will also include further development of image processing techniques that will help us to determine the causes of changes in cone reflectance, especially over long time scales. An example includes the separation of the light reflected by the background, visible as low-frequency spatial intensity, and the individual cones, and determine if and how the two are related.

6. Conclusions

We developed a largely automated procedure for the analysis of a cone mosaic and its monitoring over time, which can be used also in clinical environments. We assessed that for the purpose of cone detection there is no significant difference in the images acquired with a light source that is within 0.35 mm off from the pupil center, which is the farthest location from the pupil center used by operators of the AO flood camera to acquire high-quality images of the cone mosaic in the clinic. In addition, the light position does not affect the ability to identify and track individual cones on a series of images. On the other hand, the time separation between two or more images makes the identification of the same cone more difficult. We determined that important changes in cone reflectance also occur on long time scales (days, months and years) and that these changes increase logarithmically with time.

Acknowledgments

Research for this work was supported by the Irish Research Council (GOIPG/2013/775), the National Framework Program for Research and Innovation PON (grant n. 01_00110), the Italian Ministry of Health (grant 5×1000) and Fondazione Roma.

Data file 1. Overview of the image data set and of the sub-set divisions

Date	Time	Eccentricity (degrees temporal)	Illumination (On = pupil centre Off = 0.35mm temporal from pupil centre)
YEARS Series			
24 May 2012	16h43min	2.5 deg	On
30 June 2013	15h03min	2.5 deg	On
30 June 2015	10h48min	2.5 deg	On
MONTHS Series			
12 February 2015	11h38min	2.5 deg	On
	11h35min		Off
	11h35min	4 deg	On
	11h36min		Off
12 March 2015	12h01min	2.5 deg	On
	12h01min		Off
	12h02min	4 deg	On
	12h03min		Off
26 May 2015	16h11min	2.5 deg	On
	16h12min	4 deg	On
30 June 2015	10h48min	2.5 deg	On
	10h49min		Off
	10h50min	4 deg	On
	10h51min		Off
DAYS Series			
12 February 2015	11h38min	2.5 deg	On
	11h35min		Off
	11h35min	4 deg	On
	11h36min		Off
24 February 2015	14h07min	2.5 deg	On
	14h09min		Off
	14h11min	4 deg	On
	14h12min		Off
26 February 2015	12h41min	2.5 deg	On
	12h42min		Off
	12h43min	4 deg	On
	12h44min		Off
10 March 2015	14h32min	2.5 deg	On
	14h33min		Off
	14h34min	4 deg	On
	14h34min		Off
12 March 2015	12h01min	2.5 deg	On
	12h01min		Off
	12h02min	4 deg	On
	12h03min		Off

HOURS Series			
26 February 2015	11h10min	2.5 deg	On
	11h11min		Off
	11h12min	4 deg	On
	11h12min		Off
	12h41min	2.5 deg	On
	12h42min		Off
	12h43min	4 deg	On
	12h44min		Off
	14h16min	2.5 deg	On
	14h17min		Off
	14h18min	4 deg	On
	14h18min		Off
	17h52min	2.5 deg	On
	17h53min		Off
	17h53min	4 deg	On
	17h54min		Off
MINUTES Series			
17 March 2015	10h30min	2.5 deg	On
	10h31min		Off
	10h31min	4 deg	On
	10h32min		Off
	11h12min	2.5 deg	On
	11h13min		Off
	11h14min	4 deg	On
	11h14min		Off
	12h42min	2.5 deg	On
	12h42min		Off
	12h43min	4 deg	On
	12h44min		Off
	12h56min	2.5 deg	On
	12h57min		Off
	12h57min	4 deg	On
	12h58min		Off
	13h07min	2.5 deg	On
	13h07min		Off
	13h08min	4 deg	On
	13h09min		Off

Data file 2. Cone matching percentages for all the single images compared to the average image at their eccentricity.

Date and time	Matching percentage with the average image at 2.5 degrees		Matching percentage with the average image at 4 degrees	
	On	Off	On	Off
YEARS Series				
24 May 2012 16h43min	88 %			
30 June 2013 15h03min	91 %			
30 June 2015 10h48min	93 %	93 %		
MONTHS Series				
12 February 2015 11h38min	83 %	90 %	95 %	95 %
12 March 2015 12h01min	87 %	93 %	94 %	96 %
26 May 2015 16h11min	81 %		89 %	
30 June 2015 10h48min	93 %	93 %	95 %	96 %
DAYS Series				
12 February 2015 11h38min	83 %	90 %	95 %	95 %
24 February 2015 14h07min	89 %	91 %	93 %	96 %
26 February 2015 12h41min	90 %	91 %	96 %	96 %
10 March 2015 14h32min	92 %	90 %	94 %	95 %
12 March 2015 12h01min	87 %	93 %	94 %	96 %
HOURS Series				
26 February 2015 11h10min	93 %	93 %	97 %	96 %
26 February 2015 12h41min	90 %	91 %	96 %	96 %
26 February 2015 14h16min	88 %	92 %	95 %	96 %
26 February 2015 17h52min	92 %	91 %	92 %	95 %
MINUTES Series				
17 March 2015 10h30min	93 %	91 %	96 %	95 %
17 March 2015 11h12min	89 %	94 %	95 %	96 %
17 March 2015 12h42min	89 %	93 %	93 %	95 %
17 March 2015 12h56min	91 %	92 %	96 %	95 %
17 March 2015 13h07min	89 %	91 %	95 %	96 %

PAPER III

Mariotti, L.; Devaney, N.; Lombardo, G. & Lombardo, M.

Analysis of cone mosaic reflectance properties in healthy eyes and in eyes with non-proliferative diabetic retinopathy over time

Investigative Ophthalmology & Visual Science, 2017

5.1 CONTRIBUTIONS

After the conclusion of the analysis of images of a healthy eye, we decided to move towards the analysis of the cone mosaic in subjects with retinopathies. For this purpose Marco Lombardo gave us another data set, constituted by images acquired over years both of healthy and diseased subjects. The subjects that are under observation in the Fondazione Bietti in Rome span through different stages of DR and genetic retinal dystrophies.

We decided to focus on the analysis of DR cases for two reasons. First, the extent of the data available with the same retinal dystrophies was limited, in some cases to only one subject per dystrophy. In order to achieve more significant results on one particular retinopathy, we focused on DR, for which we had 6 cases of the mild non-proliferative type monitored over years. Second, mild NPDR has the advantage that it is not expected to produce severe modifications in the cone mosaic, such as in the position of the individual cones. This allowed us to use the same automated method used in the previous paper and verify its effectiveness on a greater number of images.

As in previous work, we decided to focus on the analysis of cone reflectance, since the spatial metrics in NPDR had already been addressed in previous studies. As we were not aware of other studies with quantitative comparison of the cone intensities, we had to choose which parameters of cone reflectance we were going to use, having in mind that they could pos-

sibly be used as biomarkers for the detection of early changes in the NPDR photoreceptor layer. I decided to use the parameters of the histogram distributions of cone reflectances and image quality from Ramaswamy's work [118].

Visual inspection of the images suggested a difference between healthy and NPDR images, notably in the spatial distribution of the cone intensities and in the intensity of the space between the cone apertures. After some research, I found that for the analysis of the spatial distribution of cone reflectance we could introduce a metric, called semivariance, that is used in geostatistics. To evaluate the difference in the intensity values of the pixels "surrounding" the cones, I proposed the ratio of the mean value of the pixels inside and outside the cone apertures as a metric. For the statistical analysis of the cone reflectance metrics, I used a linear mixed model. A thorough description of the linear mixed model and of the reasons behind its choice are presented in Appendix B.

Our collaborators Marco and Giuseppe Lombardo helped us in the redaction of the manuscript presenting these results, particularly in the clarity of the text from the point of view of a clinical audience. We submitted the manuscript for publication to the journal *Investigative Ophthalmology & Visual Science* and it was accepted for publication.

Analysis of Cone Mosaic Reflectance Properties in Healthy Eyes and in Eyes With Nonproliferative Diabetic Retinopathy Over Time

Letizia Mariotti,¹ Nicholas Devaney,¹ Giuseppe Lombardo,^{2,3} and Marco Lombardo⁴

¹Applied Optics Group, School of Physics, National University of Ireland, Galway, Ireland

²Istituto per i Processi Chimico-Fisici, Consiglio Nazionale delle Ricerche, Messina, Italy

³Vision Engineering Italy srl, Rome, Italy

⁴Fondazione G.B. Bietti IRCCS, Rome, Italy

Correspondence: Nicholas Devaney, Applied Optics Group, School of Physics, National University of Ireland, Galway, Ireland; nicholas.devaney@nuigalway.ie.

Submitted: March 25, 2017

Accepted: July 11, 2017

Citation: Mariotti L, Devaney N, Lombardo G, Lombardo M. Analysis of cone mosaic reflectance properties in healthy eyes and in eyes with non-proliferative diabetic retinopathy over time. *Invest Ophthalmol Vis Sci*. 2017;58:4057–4067. DOI:10.1167/iov.17-21932

PURPOSE. We investigate the reflectance properties of the cone mosaic in adaptive optics (AO) images of healthy subjects and subjects with nonproliferative diabetic retinopathy (NPDR) over time.

METHODS. We acquired images of the parafoveal cone mosaic over 5 years in 12 healthy subjects and in six patients with mild NPDR. We analyzed the parameters of the cone intensity histogram distribution (mean, SD, and skewness), two metrics of the cone mosaic texture (sharpness and entropy), and two novel metrics (cone/intercone intensity and slope of the variogram). Each metric was calculated on the same four retinal locations (200 × 200 μm areas, 2° from the fovea along the four meridians) over time for each subject.

RESULTS. The histogram distributions of cone intensities were similar between the two study groups. However, the cone/intercone intensity, slope of the variograms and entropy showed a significant difference between healthy and NPDR subjects ($P = 0.036$, $P = 0.002$, $P = 0.014$, respectively). All parameters, except for mean cone intensity, did not change with time in this study.

CONCLUSIONS. We observed significant differences in cone mosaic reflectance properties between healthy eyes and eyes with NPDR, in its spatial organization and in its intensity, especially between directional and nondirectional backscattering. We introduced a novel method for the study of the spatial distribution of cone reflectance, the variogram, which was able to quantify differences of the spatial dependence of cone intensities over a short range between NPDR and healthy eyes.

Keywords: cone reflectance, cones, photoreceptors, diabetic retinopathy, adaptive optics

Diabetic retinopathy (DR) is a frequently occurring complication of diabetes mellitus and is one of the leading causes of visual impairment among adults globally.^{1–3} It is a multifactorial disease apparently involving the retinal neuronal cells early in the course of disease onset and progression (i.e., neurodegenerative theory).^{4–10} The neurodegenerative changes are apoptosis of several populations of retinal cells, including photoreceptors, bipolar and ganglion cells, and astrocytes. Structural and functional impairments of the neural tissue also have been supposed to contribute to the earliest alterations of the vascular structures.^{11–13}

Recent clinical studies have focused on the investigation of the photoreceptor layer showing abnormalities of the cone packing density arrangement in the parafoveal region of subjects affected by diabetes, even before any sign of retinopathy was detected.^{14–16} Thanks to recent advances in high-resolution retinal imaging it also has been shown how a 'missing' cone photoreceptor as seen in an image acquired with conventional fundus illumination or AOSLO imaging systems cannot be attributed directly to the death of the cell itself, but rather to a disruption of its wave-guiding and light-reflecting ability.^{17,18}

While the spatial arrangement of the cones still is the most studied property of the cone mosaic,^{19–20} their light-reflecting properties recently have become the subject of an increasingly number of studies.^{21–29} Nonetheless, the investigation of the light-reflecting properties of cones in retinal diseases still is limited,^{30–34} even if in some clinical cases the cone reflectance has been the only apparent feature of the cones that distinguished a healthy cone mosaic from a mosaic with altered functionality.^{35,36}

The study of cone reflectance deserves attention, as it potentially could lead to a deeper understanding of the cone cell physiology or pathophysiology, which cannot be inferred by their spatial distribution alone.^{35–37} In this view, the development of quantitative metrics, which can be automated for extending the benefits of high-resolution retinal imaging to large populations, is expected for capturing clinically valuable information.³⁸

We tested a method for evaluating possible differences in the reflectance properties of the parafoveal cone mosaic in adults with DR compared to age-matched healthy subjects. Furthermore, we tracked these properties over 2 to 5 years. The scope was to carry out a preliminary evaluation of the

feasibility of using adaptive optics (AO) imaging biomarkers based on cone intensity for clinical purposes.

METHODS

Subjects

All research procedures described adhered to the tenets of the Declaration of Helsinki. The protocol was approved by the local ethical committee (Azienda Sanitaria Locale Roma A, Rome, Italy) and all subjects recruited gave written informed consent after a full explanation of the procedure.

Patients with a diagnosis of type 1 diabetes mellitus and age-matched healthy volunteers participated in this study. Inclusion criteria were at least 18 years of age and, for patients with diabetes, mild signs of nonproliferative DR (NPDR) according to the Early Treatment of Diabetic Retinopathy Study (ETDRS) severity scale.³⁹ 20/20 or better uncorrected or corrected distance visual acuity (UDVA or CDVA). Mild NPDR was defined as the presence of at least one microaneurysm and/or mild hemorrhages. Exclusion criteria were astigmatism higher than 2.50 diopters (D), the presence or a history of maculopathy (macular edema) or any other ocular disease, including lens opacity, or previous eye surgery (including laser treatments). Control subjects were recruited as healthy volunteers who had no history of systemic diseases. We will refer to the two groups as NPDR and controls, respectively. All subjects received a complete eye examination, including retinal imaging using a Spectralis SD-OCT (Heidelberg Engineering GmbH, Heidelberg, Germany) to exclude the presence of macular edema.

A total of 18 subjects were involved in the study, with a minimum of 2 years to a maximum of 5 years of separation between the baseline images and the last images. Of these subjects, 12 were healthy volunteers (mean age, 33 ± 7 years at baseline; sex, 5 M-7 F) and 6 were patients with mild NPDR (mean age, 40 ± 10 years at baseline; sex, 4 M-2 F). The diabetes duration at baseline was 16 ± 4 years.

Image Acquisition and Processing

A flood-illuminated AO retinal camera (rtx1; Imagine Eyes, Orsay, France) was used to acquire images of the cone mosaic. All imaging sessions were conducted after dilating the pupil with one drop of 1% tropicamide. During imaging, fixation was maintained by instructing the patient to fixate on the internal target of the instrument moved by the investigator. At each retinal location, a sequence of 40 frames was acquired by illuminating a retinal area subtending 4° of visual angle in the right eye of each subject; images were acquired at several locations in the central retina covering an area of at least $5^\circ \times 4^\circ$ centered on the preferred locus of fixation (coordinates $x = 0^\circ$ and $y = 0^\circ$). All images were acquired focusing the light source at the center of the pupil, that is, inside the first four Purkinje images of the cornea, as described previously.⁴⁰ All subjects had several images taken at different time intervals, with a minimum of 1 year separation between the imaging sessions.

Using the method described in Mariotti et al.,⁴⁰ the flat-field was calculated by averaging all unregistered frames for each subject; then, the individual frames were divided by the flat-field and registered. All image processing operations were performed using Matlab (version 9.1, R2016b; The Mathworks, Inc., Natick, MA, USA). The final images subtending 4° were montaged using the montage tool in i2k Retina Pro (DualAlign LLC, Clifton Park, NY, USA) with the aim of producing wide-field images to be used as reference to determine the position of the sample areas.

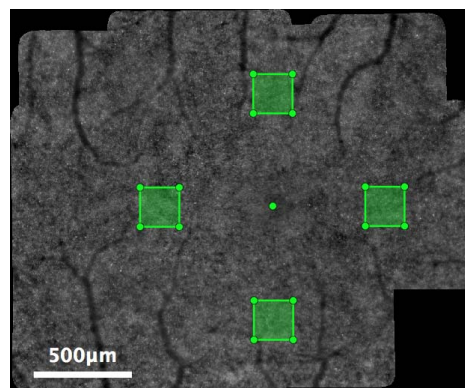


FIGURE 1. Example of montage image produced with the i2K Retina software on a control subject. The montage images were used to determine the position of the center of the fovea (green dot) and of the four selected retinal locations (green boxes), which were subsequently selected on the $4^\circ \times 4^\circ$ images. The distance from the fovea of the four sample areas is 2° and the size is $200 \times 200 \mu\text{m}$.

For each eye, four areas of the cone mosaic were analyzed. The sample areas were chosen to have a size of $200 \times 200 \mu\text{m}$ and to be located at 2° from the foveal center along the main retinal meridians (Fig. 1). The distance of 2° was chosen as a compromise between the ability of the instrument to resolve cones (not too close to the fovea) and the presence of rods, which at greater eccentricities start to be detectable and disrupt the cone mosaic.⁴¹ The corrected magnification factor (RMF_{corr}) was calculated for each eye to correct for the differences in optical magnification and, thus, retinal image size between eyes.⁴²⁻⁴⁴

The processed images subtending 4° were registered through a two-step registration process. While the first step (coarse registration) involved normalized cross correlation and used all the structures present in the images (i.e., the cones and blood vessels), the second step refined the alignment by looking at cones only; it divided the whole images in a 3×3 grid and aligned them by tracking the cones that are on average the brightest over time in each grid sector. This approach permitted us to look at the same exact location of the cone mosaic over time.⁴⁰ From these registered images, the sample areas were selected at the locations determined from the montages. The sample images were normalized by dividing them with their total intensity, i.e., the sum of all the pixel intensities, and multiplying them by the total number of pixels in the area, which gave a mean pixel intensity value equal to 1.⁴⁰ No further contrast corrections were applied.

The final data set consisted of a total of 53 observation sessions, with a total of 212 final images selected for analysis. Figure 2 shows a selection of sample images (for an overview of the study population and data set, see Supplementary Table S1).

In addition, for each subject one image focused at the inner retina (i.e., the blood vessel layer) was acquired, to compare the low frequency spatial changes in the image intensity between the inner retina and the photoreceptor layers. This was done to investigate the origin of the variable spatial pattern of cone intensities in AO flood illumination images of the photoreceptor mosaic. To achieve this, the images of the inner retina and photoreceptor layers were registered; therefore, for each pair of images, sample areas of 200×200

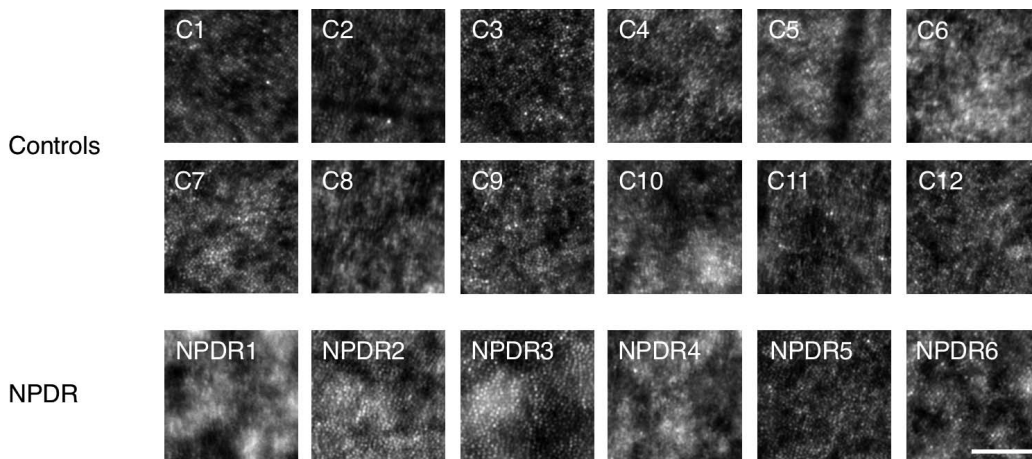


FIGURE 2. A selection of images used in the study. All images in this Figure were acquired at 2° temporal from the fovea at the baseline time. Scale bar: 100 μm.

μm on the same retinal location of the two layers were selected. The inner retinal images then were low pass filtered using a mask on the Fourier spectrum that kept only the frequencies smaller than the frequency of cone packing, that is, 145 cycles per degree (Yellott's ring).⁴⁵ The low pass filtered sample areas of the inner retina then were subtracted from the photoreceptor layer sample areas (Fig. 3).

Cone Detection

We used the same method for analysis of the cone mosaic and reflectance presented previously.⁴⁰ Here, we give a brief summary for the purpose of clarity.

The sample areas at the same location were averaged over time for each subject. Cones were detected and segmented on the average images with the entirely automated algorithm presented by Chiu et al.⁴⁶ We used the segmentations of the cone apertures on the images averaged over time based on previous work.^{26,40} Previous studies have shown that in eyes with DR a fraction of cones presents a loss of reflectivity.^{14,19}

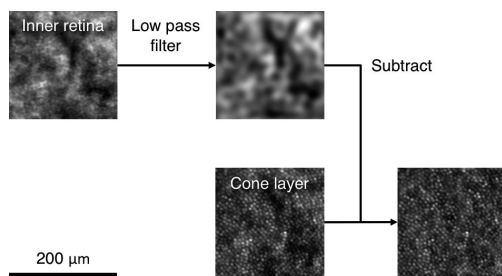


FIGURE 3. Illustration of the method used for the evaluation of the contribution of the inner retina on the cone mosaic intensity. Sample areas of the cone mosaic and of the image focused on the inner retina (200 × 200 μm) are selected on the same retinal location. The image of the inner retina is low pass filtered, to exclude all frequencies that correspond to the cones (Yellott's ring) or smaller features. The low pass filtered image then is subtracted from the cone layer image.

If a cone hypothetically loses its ability to reflect light (because of cone death or other causes), the use of the coordinates on the average of different times allows us to monitor the reflectance of that point on the cone mosaic even if in one or more images in the series that cone was not reflecting. In this way, we aimed at approaching the best case scenario where cones are not detected only if they are consistently dark throughout time, in which case the only way to determine if they still are structurally intact would be a localized function analysis on the individual cones.¹⁸ Therefore, the performance of the detection is increased over a single image not only on diseased but also on healthy subjects, and the skewness towards bright cones is limited as much as possible (Fig. 4). In our particular case, the averaging over time was justified by the fact that mild NPDR is not known to affect the position of the individual cones directly. The presence of more severe

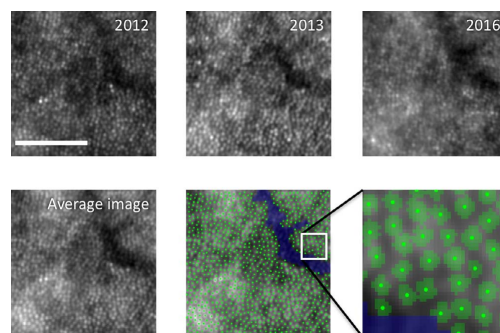


FIGURE 4. Visualization of image processing procedure, as performed on one sample area of a control subject. The images acquired at three different years at the same retinal location were averaged (bottom left), and the blood vessel (blue) and cones (in green) were segmented on the average image (bottom center). A detail (bottom right) shows the cone centers (green dots), the segmentation of the cone apertures (green masks) and part of the vessel segmentation (blue mask). Scale bar: 100 μm.

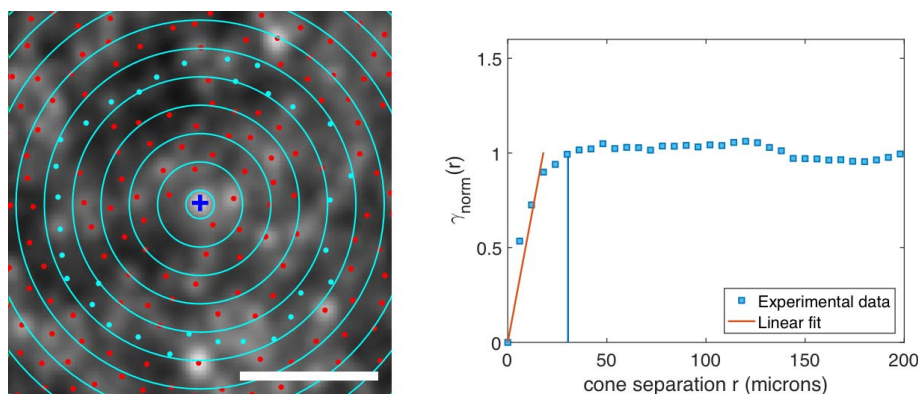


FIGURE 5. Visualization of the calculation and meaning of a variogram of intensities on a cone mosaic. On the *left*, a detail of a sample area with cones divided in rings of increasing radius, which correspond to increasing distances, from the cone in the center (*blue cross*; *Scale bar*: 30 μm). The squared difference of the intensities of all the cones that are separated by distance r is averaged for different distances, producing a variogram curve (on the *right*, the variogram calculated on the whole sample area shown on the *left*). In this variogram, $\gamma_{\text{norm}}(r)$ flattens at 1 at approximately 30 μm (*vertical blue line*), which means that the reflectance of cones separated by distances greater than 30 μm is not correlated (i.e., on the *left*, cones that are in clusters smaller than the ring highlighted in cyan have similar reflectances, while in bigger clusters the reflectance of the cones is not correlated anymore). The variogram curve is fitted linearly at short separation distances ($r < 20 \mu\text{m}$) and the slope of the linear fit is taken as a parameter.

conditions (e.g., advanced stages of retinal dystrophies) that can cause the migration of cones to different positions presumably would not allow the use of the same averaging process.

Where present, blood vessel shadows were excluded using the semiautomated method from previous studies⁴⁷ and only the cones detected in the areas devoid of vessels were analyzed (Fig. 4). The use of the average images for the segmentation of the blood vessels allowed the exclusion of vessel profiles that might have developed later in the imaging process, but that still would have appeared in the average images. This can be called a “conservative approach,” in the sense that cones are excluded from analysis even if they were obscured by the vessels only at one time point. If microaneurysms were present, they would have appeared as dark spots on the cone mosaic.^{14,48} We did not observe such features at our designated locations, but we want to point out that they would have been equally segmented and excluded on the base of their dark appearance with the same procedure that excludes the blood vessels.

As the area occupied by the vessels is excluded, the analysis could be performed at the exactly defined retinal locations with clearly detectable cones, without the need to move the selection areas to a more suitable location.¹⁴

Parameters

Cone Intensity. All sample images were normalized to have a mean intensity value of 1 and cone intensity was measured as the mean value of the pixels inside the segmentations of the cone apertures. Parameters of the cone intensity histogram, such as the mean value, standard deviation, and skewness, were calculated for each sample area.

The cone detection algorithm detects and separates the cone apertures from the surrounding pixels by assigning weights to the intensity gradients (light-to-dark and dark-to-light) and finding the shortest path around the local maximum.⁴⁶ We introduced a parameter to estimate the ratio of light backscattered from the cone apertures to that scattered by the remaining space, which we refer to here as “intercone

space.” For each image, this parameter was defined as the ratio of the mean intensity value of the pixels inside all the cone segmentations and the mean intensity value of all the pixels outside the cone segmentations (i.e., the area not covered by colored masks in Fig. 4) and gives a single numerical value for each sample area.

In addition, we introduced a new methodology for evaluation of the spatial correlation of cone reflectance by introducing the use of variograms, which is a technique already used in geostatistics.⁴⁹ We defined here the semivariance of cone reflectances as

$$\gamma(r) = \frac{1}{2N} \sum_{i,j=1}^N (I_i - I_j)^2$$

where N is the number of cone pairs in one sample image separated by distance r , I_i and I_j are the intensities of two cones separated by distance r . For each image, the semivariance $\gamma(r)$ was calculated for a set of separation distances r from 0 to 200 μm (the size of the sample area) using bins centered at multiples of 6 μm , which is the mean cone separation at 2° from the fovea.⁴² The semivariance, $\gamma(r)$, then was normalized by the total variance of the cone reflectance in the image to give $\gamma_{\text{norm}}(r)$, which was plotted against cone separation in micrometers. The plot of $\gamma_{\text{norm}}(r)$ against the separation is called the variogram. The variogram gives a measure of the degree of spatial dependence of the cone reflectance within the sample area (Fig. 5).

If the variogram assumes values lower than 1, it means that the cones intensity, separated by the corresponding distance is spatial dependent; otherwise, if the variogram assumes values close to 1, the cones reflectances are not correlated. Accordingly, the changes in the shape of the curve, that is, the presence or absence of minima or maxima, give valuable information on the spatial pattern of cone reflectance (more comprehensive description of the meaning of the curve is given in the Supplementary Material).

There are many functions based on theoretical models that have been proposed in the literature to fit experimental

variograms. As the process of choosing a fitting model for experimental variograms still does not follow a universally agreed method,⁴⁹ we focused on the analysis of the portion of the curve close to the origin. This approach allowed us to retrieve information on the degree of correlation of reflectance between cones at short range distance. We performed a linear fit on the normalized semivariance for short separation distances, that is $r < 20 \mu\text{m}$ for all images and all subjects (full methodology is described in the Supplementary Materials). Therefore, the slope of the linear portion of the variograms was chosen as a metric and calculated for all the sample images (Fig. 5b).

In addition, where available, we calculated the variograms of cone intensities after subtraction of the contribution of the low pass filtered inner retina image.

Cone Mosaic Texture. In addition to the parameters related to the intensity of the cones, we also evaluated the textural characteristics of the cone mosaic as a whole using all the pixels of the images, that is, without segmenting between cone apertures and intercone space. Two metrics, such as sharpness and entropy, commonly used to assess image quality,⁵⁰ were used for this scope. Sharpness was defined as originally proposed by Muller and Buffington,⁵¹ as

$$S_{\Gamma} = \sum_{x,y} \Gamma_{D1}[I(x,y)]$$

where

$$\Gamma_{D1}(I) = \frac{1}{12} (I - \bar{I})^{\beta}$$

where I is the intensity of the pixels in the image and \bar{I} is the mean pixel intensity. For the numerical parameters we used the values $\gamma = 0.98$ and $\beta = 2$, retrieved as optimized values in previous work.⁵⁰ Entropy, which is a statistical measure of randomness that can be used to characterize the texture of images, was defined as:

$$E = - \sum_i p_i \log_2(p_i)$$

where p_i is the probability of the i^{th} pixel intensity value (e.g., $i = 0, 1, \dots, 255$ for 8-bit images). The probabilities were approximated by the histogram of the image. A more comprehensive description of these texture parameters and of their application on cone mosaic images can be found in our previous work.⁵⁰

The pixels marked as vessel shadows were excluded from the analysis, to consider only the properties of the cone mosaic.

Statistical Analysis

To determine the effect of different factors on the parameters, we performed a linear mixed model analysis. This type of analysis was chosen to be able to deal with missing observations and to introduce random effects given by the intersubject variability.^{19,42,52,53}

The parameters calculated on all the sample images were processed in two ways to determine if there was a significant interaction between the parameters and either the condition of the subject (control or NPDR), time (year), or the retinal location (2° temporal, superior, nasal, and inferior). They were analyzed either considering the four retinal locations separately for each subject or the average of the parameters over the four retinal locations for each subject at each time point. This approach allowed us to determine if it was possible to use only one global "clinically useful value" for the parafoveal cone

mosaic reflectance that would allow discrimination between healthy and diabetic retinas.¹⁵

Data were tested for normality with the Shapiro-Wilk test. The 95% confidence intervals (95% CI) were calculated as $\pm 1.96\sigma/\sqrt{n}$, where n is the number of observations and σ the standard deviation. Statistical analysis of the results was performed with SPSS software (version 23; SPSS, Inc., Chicago, IL, USA). In both cases, all possible interactions between the factors were tested. The different mixed models for all parameters were compared using the Bayesian Information Criterion (BIC) for the penalized likelihood, and the model that minimized it was chosen as the best fitting one.

Based on the results from previous work describing the average changes of the mean cone intensity over a period of 3 years,⁴⁰ sample size calculation was performed to detect a difference of 0.002 between the average cone intensity for the control and NPDR groups, at a significance level of 5% and a power of 98%, assuming a standard deviation of 0.001. The sample size of the study was 18 cases (allocation ratio of 2:1).

RESULTS

Figure 6 shows a selection of cone intensity histograms (calculated on the same sample images shown in Fig. 2). For all the parameters, the best fit linear mixed model (minimum BIC) was shown always to be the model with only the main effects, no interactions of the fixed effects and with random intercept with respect to time only (data not shown). All P values for these models are reported in Tables 1 and 2.

Table 3 reports the estimates from the linear mixed model of the average of the parameters at the four retinal locations. For visual assessment of the differences between the groups, Figure 7 shows boxplots of the parameter estimates for the average of the locations at all time values.

Cone Intensity

From Table 1, we see that time and retinal location had no significant effect on the parameters related to cone intensity ($P > 0.05$), except for mean cone intensity ($P = 0.038$ for time) and cone/intercone intensity ($P = 0.005$ for location) considering all the values at different retinal locations. Retinal location was not a significant factor (apart from one parameter), justifying the use of the mean of the parameters at the four locations as a global estimate of the parafoveal cone reflectance properties for each subject.

Considering the global estimates of the parameters (Table 2), time was not significant for all parameters ($P > 0.05$), while the condition had a significant effect for mean cone intensity ($P = 0.047$), cone/intercone intensity ($P = 0.036$), and the slope of the variograms ($P = 0.002$).

The mean cone intensity was significantly higher in controls (1.0033 ± 0.0003) than in NPDR eyes (-0.0010 ± 0.0005 lower than controls, Table 3) if the four locations were averaged ($P = 0.047$), but not if the four locations are considered separately ($P = 0.068$). The other parameters describing the shape of the cone intensity distributions, standard deviation, and skewness, were not significantly different between the two study groups ($P > 0.05$, with separate locations and average of locations). The ratio of cone to intercone intensity was significantly higher in controls than NPDR eyes, both considering all locations ($P = 0.031$) or the average of locations ($P = 0.036$, NPDR being -0.004 ± 0.002 lower than controls 1.002 ± 0.001 , Table 3).

The linear slope of the variograms was significantly steeper in controls than in NPDR eyes, both considering the values at the four retinal locations separately ($P = 0.002$) and averaged

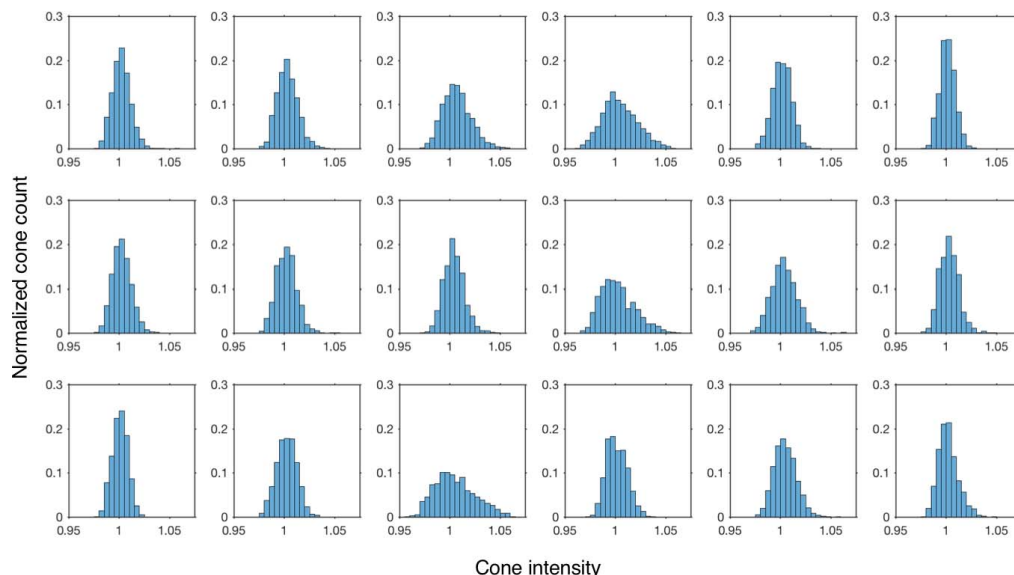


FIGURE 6. Histograms of cone intensity on the selection of images shown in Figure 2. The y-axis represents the fraction of cones over the total number in the image, on the x-axis the values of cone intensity.

($P = 0.002$), with global estimates 0.039 ± 0.002 for controls and NPDR being -0.011 ± 0.003 lower than controls (Table 3). The average variogram curves for controls and NPDR eyes are shown in Figure 8. For most of the curves, the slope at the origin and shape of the curve were constant over time, confirming the lack of effect given by time ($P = 0.331$ for average of locations, Table 2).

Most parameters also showed a significant contribution from the random deviation of the intercept for each individual around the respective group means (Wald Z test for random intercept; see the last column in Tables 1, 2).

The subtraction of the inner retinal layer variations in intensity affected the shape of the histograms. In particular, after subtraction, the variograms showed a steeper slope at the

origin and a leveled curve with the suppression of the peaks, which means that the low-frequency intensity variation was largely removed. Figure 9 shows two representative curves (one healthy and one NPDR), before and after the subtraction process.

Cone Mosaic Texture

The mosaic texture metrics, sharpness, and entropy, were not influenced by retinal location or the acquisition time ($P > 0.05$). On the other hand, a significant difference due to the patient's condition was found; the difference between controls and NPDR was statistically significant only for entropy ($P = 0.014$ all locations, $P = 0.14$ average of locations), with NPDR being 0.16 ± 0.06 higher than controls at 5.54 ± 0.04 at the average of locations. Sharpness, on the other hand, was comparable between groups ($P = 0.410$ all locations, $P = 0.408$

TABLE 1. P Values for Main Effects Condition (Between-Groups), Time (Within-Subjects), Retinal Location (Within-Subjects), and Random Intercept for the Data at All Retinal Locations Considered Separately

Parameter (All Retinal Locations)	Retinal			Wald Z Test for Random Intercept
	Condition (Between-Groups)	Location (Within-Subject)	Time (Within-Subject)	
Mean cone intensity	0.067	0.599	0.038*	0.010*
St dev cone intensity	0.348	0.950	0.411	<0.001*
Skewness cone intensity	0.107	0.415	0.975	0.066
Cone/intercone intensity	0.031*	0.005*	0.825	0.061
Variogram slope	0.002*	0.244	0.828	0.009*
Sharpness	0.410	0.462	0.549	0.010*
Entropy	0.014*	0.930	0.628	0.074

Last column shows the P value for the significance of the intercept for the individual subjects.
* Significant P values ($P < 0.05$).

TABLE 2. P Values for Main Effects Condition (Between-Groups) and Time (Within-Subjects) and Random Intercept for the Average of the Data Between the Retinal Locations

Parameter (Average of Retinal Locations)	Condition (Between-Groups)	Time (Within-Subject)	Wald Z Test for Random Intercept
Mean cone intensity	0.047*	0.084	<0.001*
St dev cone intensity	0.732	0.160	0.006*
Skewness cone intensity	0.103	0.304	0.031*
Cone/intercone intensity	0.036*	0.841	0.151
Variogram slope	0.002*	0.331	0.014*
Sharpness	0.408	0.284	0.007*
Entropy	0.014*	0.879	0.107

Last column shows the P value for the significance of the intercept for the individual subjects.
* Significant P values ($P < 0.05$).

TABLE 3. Mean ± SD Values and 95% CI of the Average Between Locations Parameters as Estimated From the Linear Mixed Model for the Condition Effect Only

	Control			NPDR (Variations With Respect to Control)			P Values Between Groups
	Mean	SD	95% CI	Mean	SD	95% CI	
Mean cone intensity	1.0033*	0.0003*	1.0027 to 1.0039*	-0.0010*	0.0005*	-0.0019 to -0.0000*	0.047*
Cone intensity st dev	0.0121	0.0007	0.0106 to 0.0136	0.0004	0.0012	-0.0021 to 0.0030	0.732
Cone intensity skewness	0.44	0.04	0.36 to 0.52	-0.11	0.06	-0.24 to 0.02	0.103
Cone/intercone intensity	1.002*	0.001*	1.000 to 1.005*	-0.004*	0.002*	-0.007 to -0.000*	0.036*
Variogram slope	0.039*	0.002*	0.035 to 0.042*	-0.011*	0.003*	-0.017 to -0.005*	0.002*
Sharpness	2.93	0.11	2.70 to 3.16	0.15	0.19	-0.24 to 0.55	0.410
Entropy	5.54*	0.04*	5.46 to 5.62*	0.16*	0.06*	0.04 to 0.28*	0.014*

The values of the NPDR are expressed as variations with respect to the control group.
 * The parameters that have a significant difference between the two study groups.

average of locations) and had a significant contribution of the random intercept ($P=0.010$ all locations, $P=0.007$ average of locations). The random intercept term for entropy was not significant (see the Wald Z test for random intercept in Tables 1, 2).

DISCUSSION

The mean cone intensity was significantly different between healthy and NPDR eyes, but only if the average between the retinal locations was considered (Tables 1, 2). In addition, if all data at different locations were taken into account, there was a dependence on time, and this was the only parameter for which this was the case. This dependence on retinal location, together with the lack of significant differences in standard deviations and skewness between groups, indicated that the histograms of cone intensities are not good candidates to

investigate differences in cone reflectance caused by diabetes mellitus.

Under the assumption that the intensity of the pixels inside the segmentations is primarily directional light backscattered from the outer/inner segment (IS/OS) junction and pixel intensity outside the cone segmentations corresponds to nondirectional backscattered light,⁵⁴⁻⁵⁶ in healthy subjects there was a significantly higher fraction of directional backscattered light than in those with NPDR, given by the higher ratio of cone/intercone intensity. A significant difference in cone intensity in areas where the cones still were detectable, although with abnormal packing density arrangement, has been found previously.^{14-16,19} A possible explanation could be the alteration of the wave-guiding properties due to the pathology of the individual cones.¹⁶ The significance of the retinal location for this factor could suggest that this variation of cone intensity, even if important enough at all locations so that its average still is significantly different between groups,

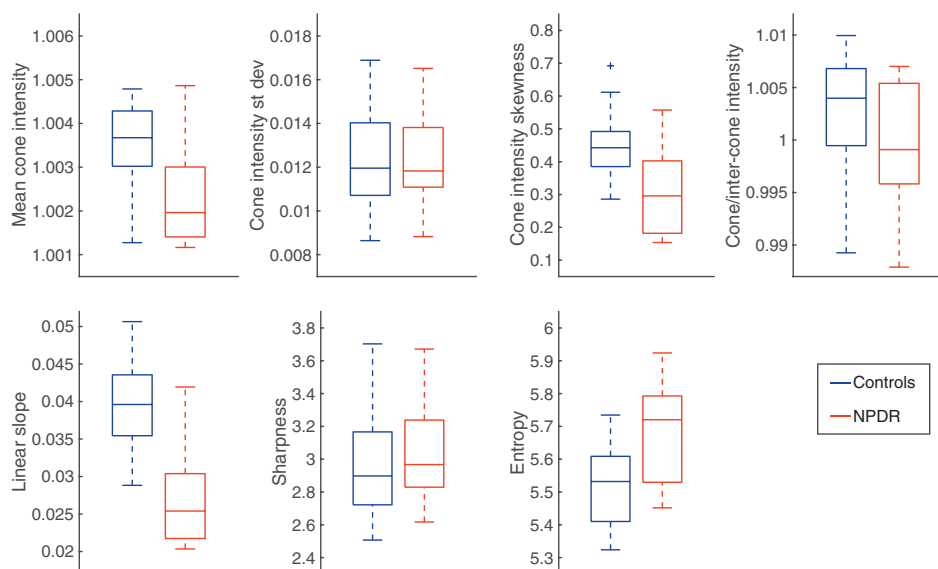


FIGURE 7. Boxplots of marginal data at all time levels for the results averaged between the four retinal locations. The plots show the median of the parameter estimates of the two study groups with the boxes representing the interquartile range, that is, the 25th and 75th percentile of the group values. Whiskers extend to the most extreme data values that are not outliers. Outliers (plus signs) are defined as values that are further than 1.5 times the interquartile range from the median.

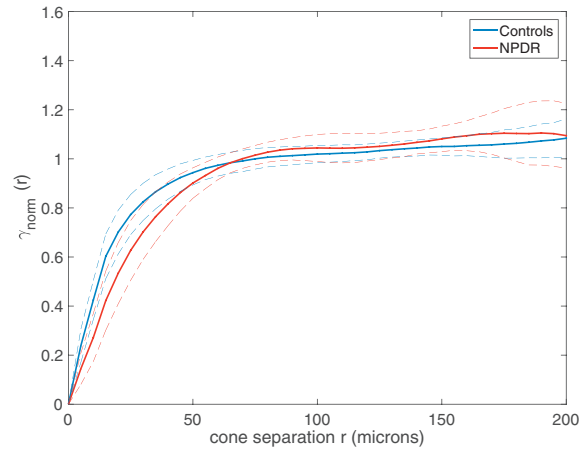


FIGURE 8. Marginal mean variogram curves for the study (red curve) and control (blue curve) groups with ± 1 SD (dashed curves). The mean curves were calculated averaging all the curves for all the retinal locations of the subjects according to their group. The study group had a shallower slope than controls at the origin of the variogram curve ($< 20 \mu\text{m}$), indicating a more pronounced correlation between cone intensities separated by short distances than the control group. Most of the NPDR cases showed variogram curves having a shape not leveling to a maximum value, but rather some showed a peak and then decreased again, while others showed two peaks (see Supplementary Material).

might not be constant across the central retina (e.g., caused by variable effect of intraretinal scattering, and so forth). Another possible explanation could be given by the rods, which are not resolved in these images but may be present sporadically in between the cones at these eccentricities. In this case, the difference in the ratio would indicate a change in the rod reflectance, or a combination of changes in rods and cones. Even if significant, the difference between the ratio in the two groups had a small numerical value (Table 3), as in the case of the mean intensity, which could make the use of this parameter for clinical applications hard to achieve. Further investigation

of the ratio of cone/intercone intensity at different illumination angles could improve the understanding of how this phenomenon is correlated with cone function and if it eventually also is related to cone spatial properties, such as spatial density or packing arrangement.

We chose to use a sample area of $200 \mu\text{m}$ side, which was bigger than what has been used in similar studies,^{14,15} to have an area big enough to evaluate the reflectance property of several clusters of cones in all subjects. From the analysis of the spatial distribution of cone reflectance through the variograms, we were able to infer a significant difference between the two

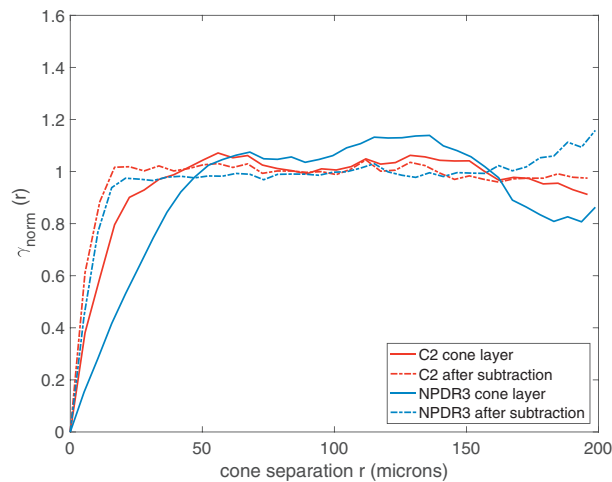


FIGURE 9. Variograms of cone intensities for two subjects (C2 and NPDR3), before and after the subtraction of the low frequency intensities as measured from the inner retina images. The subtraction process causes a flattening of the curves and a steepening of the slope at the origin. Where present, the peaks also are suppressed.

groups and this result was consistent between the average of the locations and for all locations considered. The NPDR curves showed a shallower slope at short distances ($<20 \mu\text{m}$), reflecting the fact that the cones appear to be clustered in bright and dark patches more than in healthy subjects. In addition, the average variogram curves in NPDR eyes showed peaks at long distances ($>50 \mu\text{m}$), which were not found in healthy subjects. These peaks corresponded to the distance at which there was a greater difference in the observed cone intensity. In NPDR eyes, it is likely that the position of the peaks reveals the size of the bright and dark intensity patches present in the images (see Supplementary Materials). The intersubject variability in the shapes would make challenging the definition of a characteristic "standard" variogram shape in an adult population at this moment. For this reason, we analyzed the initial slope of the variograms, which showed potential as a straightforward method to quantify the degree of spatial dependence of cone intensities over a short range. The clustering of cone reflectances did not show a significant dependence on the retinal location, implying that difference in these two aspects of cone reflectance between healthy and NPDR eyes might have different causes. This dependence can be caused by the physiology/pathophysiology of the photoreceptor layer itself or of other layers. Further work is needed to investigate suitable models to fit experimental data and develop a more complete procedure to compare curves from different subjects or retinal locations. In addition, more work could be done to understand how this approach can be extended to other retinal diseases. Strictly related to the multiple humped shape of the variogram found in NPDR eyes, clustering of the cone reflectivity has been qualitatively observed in DR^{14,19} and inherited retinal diseases. For example, in albinism, clustering has been related to the melanin distribution in the retina;⁵⁰ in choroideremia, hyper-reflective clusters of cones have been related to alteration in the RPE.³³ Degeneration of the RPE also has been indicated as a cause of disruption of cone reflectivity in age-related macular degeneration, possibly before the formation of drusen.³⁴

The inner retina has been shown to influence the low frequency pattern of cone intensity in AO flood illumination images of the cone mosaic (Fig. 9). The presence of subclinical or clinically visible abnormalities located in the inner layers of the retina (e.g., microaneurysms, microvascular abnormalities, subtle retinal edema) might further explain the greater clumping found in NPDR eyes than controls.¹⁶ A thickening of the inner retinal layers, which could not be considered as macular edema, has been found previously in diabetic eyes.^{14,19} Further work is ensured to correlate the changes in the cone reflectance properties with the abnormalities in spectral domain-optical coherence tomography (SD-OCT) cross-section images of the same subject. Another possible explanation could be a high degree of alignment between neighboring cones, with clusters of cones pointing towards the pupil center appearing here brighter than clusters of cones pointing away from the center. This hypothesis could be investigated again, as in the case of nondirectional backscattered light, with observations at different illumination angles.^{27,54}

In any case, even if the source of the modifications in cone reflectance was the result of shadowing artifacts and not of abnormalities in the cones, their quantification still can be used as an indicator of the disease.

We also analyzed the texture of the parafoveal cone mosaic with two metrics originally used for the assessment of image quality. The reason behind the choice of only these two metrics, sharpness and entropy, from the cited study⁵⁰ is that these investigators found other quality metrics, such as variance, contrast, and kurtosis, to be highly correlated with

sharpness, while entropy was not. In this way, we were able to explore different aspects on the images, such as the definition of bright features over the background (sharpness) and the textural properties of the image (entropy). Entropy was significantly higher in the AO images of the cone mosaic in NPDR eyes than controls, while sharpness was very similar between the two groups. A possible explanation could be that sharpness measures the definition of the cone apertures as bright dots over a darker background. In this sense, this characteristic seems not to depend on the condition of the retina. Entropy, on the other hand, relies on the histogram distribution (Fig. 6). The fact that entropy involves taking the logarithm of the histogram makes it more sensitive to extreme intensity values, and so it is able to detect a difference in images with apparently similar histograms (in a previous study, sharpness was highly correlated with the image variance, while entropy was not).⁵⁰

We did not observe the characteristics of cone reflectance or mosaic texture of the same areas in AO flood illuminated retinal images to change significantly with time. In a previous study,⁴⁰ we found that although the cones individually change reflectance over time in a random way, the distribution of the cone intensities maintains the same shape over time, and this result was confirmed here. This also was true for the retinas affected by NPDR, as we also observed no significant interaction between time and condition. A possible explanation for the lack of change, especially for the NPDR group, is that the time range considered was too short compared to the development time of the disease. Furthermore, the retinal location proved not to be a significant factor influencing the cone reflectance in AO flood retinal images, meaning that the cone mosaic has similar intensity and textural characteristics at different locations at the same distance from the fovea. This result confirmed the validity of using the average of the values of the four locations as one global parameter with potential to be translated to clinical studies.

An important aspect of this work is the automation of the analysis. We used our previously described method⁴⁰ for the analysis of large retinal patches ($\geq 2 \times 2^\circ$ or $\geq 0.61 \times 0.61 \text{ mm}$), showing how performing the detection on time averaged images further improved the performance of the automated cone detection algorithm, which is 97% of cones correctly detected using only one image. The improvement in the automated detection performance using more images taken at different times also can be justified for the NPDR images, which can present a decrease in cone density but no major deterioration that would require manual supervision. On similar images, the investigators in a different study¹⁴ have used an automated algorithm with poorer performance³⁷ and the percentage of cones that had to be corrected manually was not greater than 9% also for NPDR cases, which is compatible with the performance of the same algorithm on healthy retinas.⁵⁷

Limitations of this study included the small sample size (especially the NPDR cases), though it had enough power to verify the hypothesis of the study, and the incomplete number of observations with time in all cases. Future work could include a more consistent number of subjects at different stages of the disease and a longer time range, which could lead to observation of change on the same retina with time. Another improvement could be achieved using complementary observation modalities, such as AO-scanning laser ophthalmoscopy (AO-SLO) and/or AO-OCT, as well as using different illumination angles, which could provide a better resolution closer to the fovea ($<2^\circ$) and insights into the causes of differences in cone reflectance. Finally, analysis of the function of the retina in the selected regions also could be performed, to determine

the clinical significance of the differences between healthy and NPDR eyes.

In conclusion, we observed significant differences in cone mosaic reflectance properties between healthy eyes and eyes with mild NPDR, in its spatial organization and in its intensity, especially between directional and nondirectional backscattering. We did not observe significant changes of the parameters with time in any group. We performed a largely automated analysis of cone reflectance and introduced a novel method for the study of the spatial distribution of intensity, the variogram, which was able to quantify differences of the spatial dependence of intensity values of the cone layer at a short range between NPDR and control eyes and a tendency of cones in NPDR to appear clustered in clumps of similar intensities.

Acknowledgments

Supported by the National Framework Program for Research and Innovation PON (grant no. 01_00110), the Italian Ministry of Health (5x1000 funding), Fondazione Roma, and the Irish Research Council (GOIPG/2013/775).

Disclosure: L. Mariotti, None; N. Devaney, None; G. Lombardo, None; M. Lombardo, None

References

- Pascolini D, Mariotti SP. Global estimates of visual impairment. 2010. *Br J Ophthalmol*. 2012;96:614–618.
- Lee R, Wong TY, Sabanayagam C. Epidemiology of diabetic retinopathy, diabetic macular edema and related vision loss. *Eye Vision*. 2015;2:17.
- Martín-Merino E, Fortuny J, Rivero-Ferrer E, García-Rodríguez LA. Incidence of retinal complications in a cohort of newly diagnosed diabetic patients. *PLoS One*. 2014;9:1–6.
- Barber AJ. A new view of diabetic retinopathy: a neurodegenerative disease of the eye. *Prog Neuro-psychopharmacol Biol Psychiatry*. 2003;27:283–290.
- Fletcher EL, Phipps JA, Wilkinson-Berka JL. Dysfunction of retinal neurons and glia during diabetes. *Clin Exp Optometry*. 2005;88:132–145.
- Verma A, Rani PK, Raman R, et al. Is neuronal dysfunction an early sign of diabetic retinopathy? Microperimetry and spectral domain optical coherence tomography (SD-OCT) study in individuals with diabetes, but no diabetic retinopathy. *Eye*. 2009;23:1824–1830.
- van Dijk HW, Verbraak FD, Kok PHB, et al. Early neurodegeneration in the retina of type 2 diabetic patients. *Invest Ophthalmol Vis Sci*. 2012;53:2715–2719.
- Stem MS, Gardner TW. Neurodegeneration in the pathogenesis of diabetic retinopathy: molecular mechanisms and therapeutic implications. *Curr Med Chem*. 2013;20:3241–3250.
- Ola MS, Nawaz MI, Khan HA, Alhomida AS. Neurodegeneration and neuroprotection in diabetic retinopathy. *Int J Mol Sci*. 2013;14:2559–2572.
- Simó R, Hernández C. Neurodegeneration in the diabetic eye: new insights and therapeutic perspectives. *Trends Endocrinol Metab*. 2014;25:23–33.
- Lieth E, Gardner TW, Barber AJ, Antonetti DA. Retinal neurodegeneration: early pathology in diabetes. *Clin Exp Ophthalmol*. 2000;28:3–8.
- van Dijk HW, Kok PHB, Garvin M, et al. Selective loss of inner retinal layer thickness in type 1 diabetic patients with minimal diabetic retinopathy. *Invest Ophthalmol Vis Sci*. 2009;50:3404–3409.
- Sohn EH, van Dijk HW, Jiao C, et al. Retinal neurodegeneration may precede microvascular changes characteristic of diabetic retinopathy in diabetes mellitus. *Proc Natl Acad Sci USA*. 2016;113:E2655–E2664.
- Lombardo M, Parravano M, Lombardo G, et al. Adaptive optics imaging of parafoveal cones in type 1 diabetes. *Retina*. 2014;34:546–557.
- Lombardo M, Parravano M, Serrao S, Ziccardi L, Giannini D, Lombardo G. Investigation of adaptive optics imaging biomarkers for detecting pathological changes of the cone mosaic in patients with type 1 diabetes mellitus. *PLoS One*. 2016;11:e0151380.
- Lammer J, Prager SG, Cheney MC, et al. Cone Photoreceptor irregularity on adaptive optics scanning laser ophthalmoscopy correlates with severity of diabetic retinopathy and macular edema cone mosaic irregularity in diabetic eyes on AOSLO. *Invest Ophthalmol Vis Sci*. 2016;57:6624–6632.
- Scoles D, Sulai YN, Langlo CS, et al. In vivo imaging of human cone photoreceptor inner segments. *Invest Ophthalmol Vis Sci*. 2014;55:4244–4251.
- Bruce KS, Harmening WM, Langston BR, Tuten WS, Roorda A, Sincich LC. Normal perceptual sensitivity arising from weakly reflective cone photoreceptors normal perceptual sensitivity of weakly reflective cones. *Invest Ophthalmol Vis Sci*. 2015;56:4431–4438.
- Lombardo M, Serrao S, Devaney N, Parravano M, Lombardo G. Adaptive optics technology for high-resolution retinal imaging. *Sensors*. 2013;13:334–366.
- Cooper RF, Wilk MA, Tarima S, Carroll J. Evaluating descriptive metrics of the human cone mosaic descriptive metrics of the human cone mosaic. *Invest Ophthalmol Vis Sci*. 2016;57:2992–3001.
- Pallikaris A, Williams DR, Hofer H. The reflectance of single cones in the living human eye. *Invest Ophthalmol Vis Sci*. 2003;44:4580–4592.
- Jonnal RS, Rha J, Zhang Y, Cense B, Gao W, Miller DT. In vivo functional imaging of human cone photoreceptors. *Opt Express*. 2007;15:16141–16160.
- Rha J, Schroeder B, Godara P, Carroll J. Variable optical activation of human cone photoreceptors visualized using a short coherence light source. *Opt Lett*. 2009;34:3782–3784.
- Jonnal RS, Besecker JR, Derby JC, et al. Imaging outer segment renewal in living human cone photoreceptors. *Opt Express*. 2010;18:5257–5270.
- Cooper RF, Dubis AM, Pavaskar A, Rha J, Dubra A, Carroll J. Spatial and temporal variation of rod photoreceptor reflectance in the human retina. *Biomed Opt Express*. 2011;2:2577–2589.
- Pircher M, Kroisamer JS, Felberer F, Sattmann H, Götzinger E, Hitzengerger CK. Temporal changes of human cone photoreceptors observed in vivo with SLO/OCT. *Biomed Opt Express*. 2011;2:100–112.
- Rativa D, Vohnsen B. Analysis of individual cone-photoreceptor directionality using scanning laser ophthalmoscopy. *Biomed Opt Express*. 2011;2:1423–1431.
- Bedgood P, Metha A. Variability in bleach kinetics and amount of photopigment between individual foveal cones. *Invest Ophthalmol Vis Sci*. 2012;53:3673–3681.
- Bedgood P, Metha A. Optical imaging of human cone photoreceptors directly following the capture of light. *PLoS One*. 2013;8:e79251.
- McAllister JT, Dubis AM, Tait DM, et al. Arrested development: high-resolution imaging of foveal morphology in albinism. *Vision Res*. 2010;50:810–817.
- Genead MA, Fishman GA, Rha J, et al. Photoreceptor structure and function in patients with congenital achromatopsia. *Invest Ophthalmol Vis Sci*. 2011;52:7298–7308.
- Dubis AM, Cooper RF, Aboshiha J, et al. Genotype-dependent variability in residual cone structure in achromatopsia:

- toward developing metrics for assessing cone health/assessing residual photoreceptor integrity in ACHM. *Invest Ophthalmol Vis Sci.* 2014;55:7303-7311.
33. Morgan JIW, Han G, Klinman E, et al. High-resolution adaptive optics retinal imaging of cellular structure in choroideremia. *Invest Ophthalmol Vis Sci.* 2014;55:6381-6397.
 34. Land ME, Cooper RF, Young J, et al. Cone structure in subjects with known genetic relative risk for AMD. *Optom Vis Sci.* 2014;91:939-949.
 35. Godara P, Wagner-Schuman M, Rha J, Connor TB Jr, Stepien KE, Carroll J. Imaging the photoreceptor mosaic with adaptive optics: beyond counting cones. In: LaVail MM, Ash JD, Anderson RE, Hollyfield JG, Grimm C, eds. *Retinal Degenerative Diseases*. New York: Springer; 2012:451-458.
 36. Godara P, Siebe C, Rha J, Michaelides M, Carroll J. Assessing the photoreceptor mosaic over drusen using adaptive optics and SD-OCT. *Ophthalmic Surg Lasers Imaging.* 2010;41: S104-S108.
 37. Jacob J, Paques M, Krivosic V, et al. Meaning of visualizing retinal cone mosaic on adaptive optics images. *Am J Ophthalmol.* 2015;159:118-123.
 38. Agurto C, Barriga ES, Murray V, et al. Automatic detection of diabetic retinopathy and age-related macular degeneration in digital fundus images. *Invest Ophthalmol Vis Sci.* 2011;52: 5862-5871.
 39. Early Treatment Diabetic Retinopathy Study Research Group. Fundus photographic risk factors for progression of diabetic retinopathy. *Ophthalmology.* 1991;98:823-833.
 40. Mariotti L, Devaney N, Lombardo G, Lombardo M. Understanding the changes of cone reflectance in adaptive optics flood illumination retinal images over three years. *Biomed Opt Express.* 2016;7:2807-2822.
 41. Muthiah MN, Gias C, Chen FK, et al. Cone photoreceptor definition on adaptive optics retinal imaging. *Br J Ophthalmology.* 2014;98:1073-1079.
 42. Lombardo M, Serrao S, Ducoli P, Lombardo G. Eccentricity dependent changes of density, spacing and packing arrangement of parafoveal cones. *Ophthalmic Physiol Opt.* 2013;33: 516-526.
 43. Lombardo M, Serrao S, Ducoli P, Lombardo G. Influence of sampling window size and orientation on parafoveal cone packing density. *Biomed Opt Express.* 2013;4:1318-1331.
 44. Lombardo M, Serrao S, Lombardo G. Technical factors influencing cone packing density estimates in adaptive optics flood illuminated retinal images. *PLoS One.* 2014;9:e107402.
 45. Yellott JJ. Spectral consequences of photoreceptor sampling in the rhesus retina. *Science.* 1983;221:382-385.
 46. Chiu SJ, Likhnygina Y, Dubis AM, et al. Automatic cone photoreceptor segmentation using graph theory and dynamic programming. *Biomed Opt Express.* 2013;4:924-937.
 47. Mariotti L, Devaney N. Cone detection and blood vessel segmentation on AO retinal images. In: Dahyot R, Lacey G, Dawson-Howe K, Pitić F, Moloney D, eds. *Iris Machine Vision & Image Processing Conference Proceedings*. 2015: 126-128.
 48. Lombardo M, Parravano M, Serrao S, Ducoli P, Stirpe M, Lombardo G. Analysis of retinal capillaries in patients with type 1 diabetes and nonproliferative diabetic retinopathy using adaptive optics imaging. *Retina.* 2013;33:1630-1639.
 49. Oliver MA, Webster R. *Basic Steps in Geostatistics: The Variogram and Kriging*. New York: Springer; 2015.
 50. Ramaswamy G, Devaney N. Pre-processing, registration and selection of adaptive optics corrected retinal images. *Ophthalmic Physiol Opt.* 2013;33:527-539.
 51. Richard A, Muller AB. Real-time correction of atmospherically degraded telescope images through image sharpening. *J Opt Soc Am.* 1974;64:1200-1210.
 52. Lombardo M, Serrao S, Ducoli P, Lombardo G. Variations in image optical quality of the eye and the sampling limit of resolution of the cone mosaic with axial length in young adults. *J Cataract Refract Surg.* 2012;38:1147-1155.
 53. Park SP, Chung JK, Greenstein V, Tsang SH, Chang S. A study of factors affecting the human cone photoreceptor density measured by adaptive optics scanning laser ophthalmoscope. *Exp Eye Res.* 2013;108:1-9.
 54. Roorda A, Williams DR. Optical fiber properties of individual human cones. *J Vis.* 2002;2:404-412.
 55. Vohnsen B. Photoreceptor waveguides and effective retinal image quality. *J Opt Soc Am A.* 2007;24:597-607.
 56. Vohnsen B. Directional sensitivity of the retina: a layered scattering model of outer-segment photoreceptor pigments. *Biomed Opt Express.* 2014;5:1569-1587.
 57. Mariotti L, Devaney N. Performance analysis of cone detection algorithms. *J Opt Soc Am A.* 2015;32:497-506.

TABLE S1. Overview of the subjects and of the acquisition dates

Subject code	Gender	Condition	Age at baseline	Duration of diabetes at baseline	Acquisition dates (years)
C1	F	Control	26	-	2012, 2013, 2016
C2	F	Control	24	-	2012, 2013, 2016
C3	M	Control	32	-	2012, 2013, 2016
C4	F	Control	28	-	2013, 2016
C5	F	Control	33	-	2014, 2016
C6	M	Control	37	-	2012, 2013, 2016
C7	F	Control	36	-	2012, 2013, 2016
C8	M	Control	39	-	2012, 2013, 2016
C9	F	Control	24	-	2012, 2013, 2016
C10	M	Control	45	-	2011, 2013, 2016
C11	M	Control	32	-	2012, 2012, 2016
C12	F	Control	35	-	2012, 2013, 2016
NPDR1	M	Mild NPDR	27	12	2014, 2016
NPDR2	F	Mild NPDR	39	21	2013, 2014, 2015, 2016
NPDR3	F	Mild NPDR	38	17	2013, 2014, 2016
NPDR4	M	Mild NPDR	53	18	2013, 2014, 2015, 2016
NPDR5	M	Mild NPDR	35	16	2013, 2014, 2015
NPDR6	M	Mild NPDR	50	11	2013, 2015, 2016

Supplementary material: Variograms

The variogram is a technique usually used in geostatistics for the characterization of spatial processes. From the empirical variogram given by the data, the aim is to find the continuous function that represents the regional variation. Without going into much detail (for which we remand to the specialized literature^{1,2}), the most common fitting models for the variograms are the bounded models. In these models, the variance has a maximum, known as the *sill variance*, which may be reached either at a finite distance, known as the *range*, or asymptotically.

One of the most commonly used bounded models is the exponential model, which is described by the equation

$$\gamma(r) = c \left\{ 1 - \exp\left(-\frac{r}{R}\right) \right\}$$

with sill c , distance between the pair of points r and a distance parameter, R , that defines the spatial extent of the model. Since this model approaches the sill asymptotically, an *effective range* is defined for practical purposes as the distance at which γ equals 95% of the sill variance. This effective range is approximately $3R$ and the slope at the origin is c/R . This function is the representation of random processes, such as first-order autoregressive and Markov processes, and it has been the subject of many theoretical studies of the efficiency of sampling design.³⁻⁶

Since in this work we calculated a variogram for every image, we had a total of 212 curves. A generally accepted procedure for fitting a theoretical model to an experimental variogram is still the object of debate. Some authors have suggested using an approach that includes both visual inspection and statistical fitting.^{1,2} Since the amount of data we analysed was considerable, we decided to analyse the linear fit of the variograms at short distances, which can be easily replicated and makes no theoretical assumptions on the spatial distribution of cone reflectances.

In order to evaluate the overall trend of the semivariance in all study population, we inspected the variogram curve obtained taking the mean of all the curves (Figure S1). The resulting curve was well fitted by an exponential model, which can be explained by the fact that averaging the different features of all the subjects can be described by a random process. The exponential fit on the mean curve has as a distance parameter $R = 22\mu\text{m}$. Considering that this distance represents the average spatial extent of the individual variogram curves, we decided to use $R = 20\mu\text{m}$ as the maximum distance for all the linear fits.

We included in this appendix some experimental variograms, which we chose to be representative of the variety of spatial distributions that we encountered in our study population (Figures S2 and S3). The variograms are beside the corresponding images, to allow a visual comparison between the distribution of cone intensities and the shape of the curves. In all cases, the shape of the curves was constant with time. This allowed us to determine that the process at the basis of the spatial distribution of the intensity values in the cone layer remained the same through time, even if the reflectance of the individual cones changed.

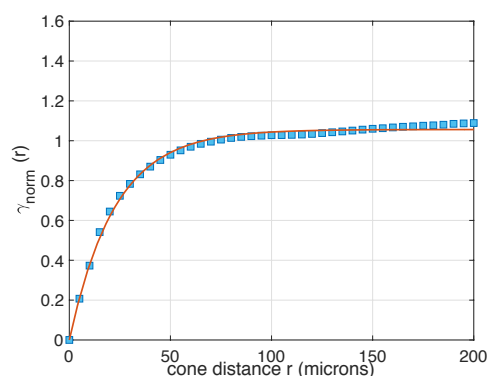


FIGURE S1. Mean of all the experimental variogram curves calculated in this study. The blue squares are the experimental data, the orange line is the exponential fitting function

References (Supplementary material)

1. Webster R, Oliver MA. Geostatistics for environmental scientists: John Wiley & Sons, Ltd; 2008.
2. Oliver MAaWR. Basic steps in geostatistics: the variogram and kriging: Springer; 2015.
3. Cochran WG. Relative accuracy of systematic and stratified random samples for a certain class of populations. The Annals of Mathematical Statistics. 1946; 164-177.
4. Yates F. Systematic sampling. Philosophical Transactions of the Royal Society of London A: Mathematical, Physical and Engineering Sciences. 1948; 241(834): 345-377.
5. Quenouille MH. Problems in plane sampling. The Annals of Mathematical Statistics. 1949; 355-375.
6. Matérn B. Spatial variation: Stochastic models and their applications to problems in forest surveys and other sampling invstigations: Meddelanden fran Statens Skogforskningnsinstitut; 1960.

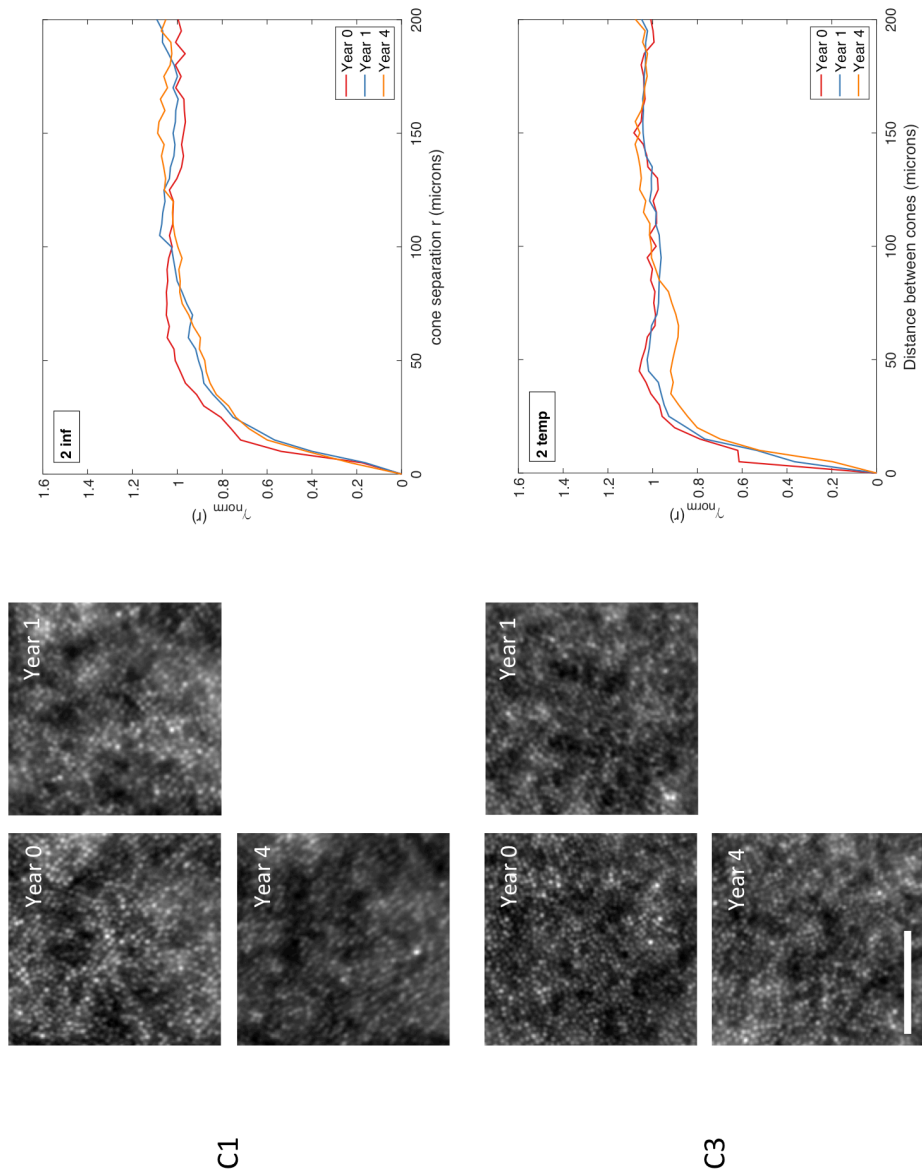


FIGURE S2. Variograms of two control subjects. The cones in the images show no apparent pattern and this is confirmed by the variograms, which reach the maximum variance at short distances and then remain flat, showing no long-distance correlation. Size bar is $100\mu\text{m}$

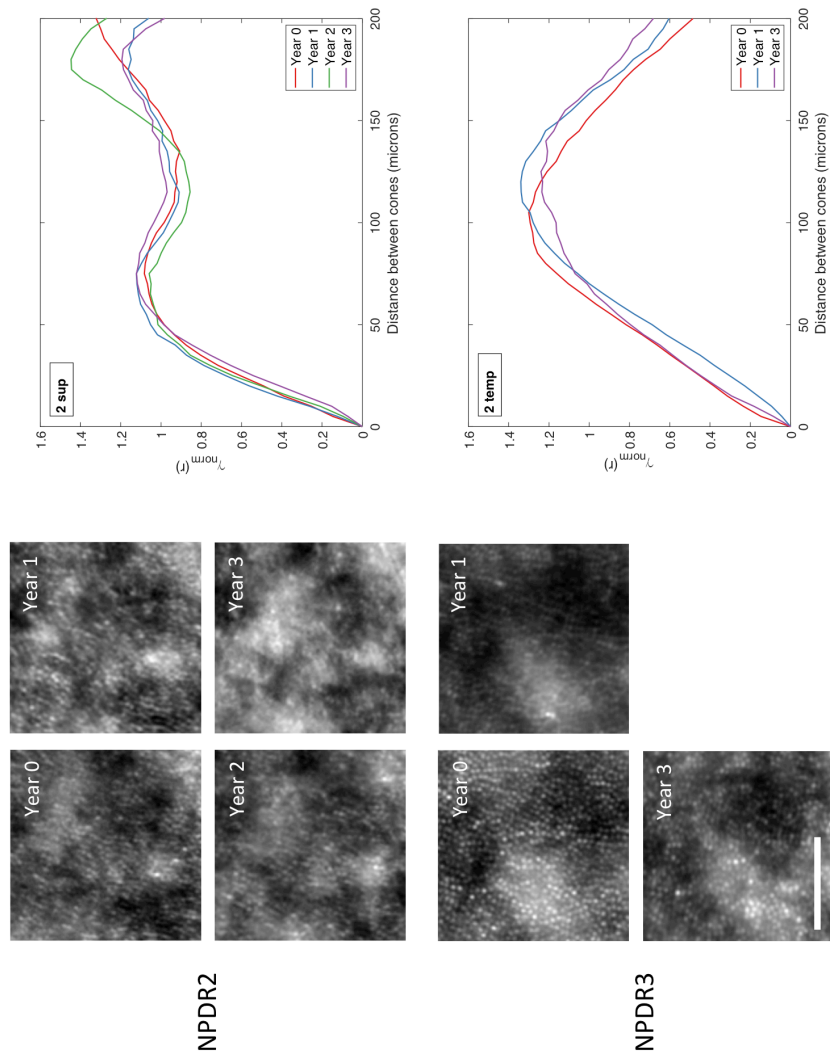


FIGURE S3. Variograms of two NPDR subjects. The shape of the curves allowed us to quantify what was only suggested by visual inspection, i.e. the presence of bright and dark patches in the images. The presence of peaks and valleys shows how cone reflectances are not independent from each other. NPDR2 shows a first peak around $60\mu\text{m}$, while NPDR3 shows a large peak approximately at $100\mu\text{m}$, which reflects the size of the bright clusters in the images. Especially in the latter case, the visual assessment is made easier by the comparison between the size of the bright cluster and the size bar ($100\mu\text{m}$), which are approximately the same.

CONCLUSIONS

In this thesis, we presented a study of processing techniques for the analysis of AO cone photoreceptor images and their application to the observation of spatial and intensity properties of cones over time. These techniques were then applied to images of healthy retinas and retinas with mild NPDR, in order to characterise the reflectance properties of the cone mosaic with the disease and to investigate biomarkers for its early detection. These studies are presented as three separate research articles in *Journal of the Optical Society of America A*, *Biomedical Optics Express* and *Investigative Ophthalmology & Visual Science* and one short article in the *Irish Machine Vision and Image Processing conference proceedings*. This chapter summarises the findings of the work and how it could be potentially extended with further research.

6.1 SUMMARY OF THESIS WORK

6.1.1 *Processing of the cone mosaic*

The work in Paper I addresses the issue of the reliability of automated cone detection by objectively quantifying the performance of cone detection algorithms from the literature. The objectivity in the evaluation of the performance was achieved first through the development of a method for the simulation of realistic cone mosaic images in the parafoveal region and then through the introduction of FROC analysis for the optimization of the algorithm parameters. We determined how the different features of the images (spatial sampling and image quality) affect the detection algorithms. We saw that the percentage of hexagonal Voronoi cells is the parameter that is most affected by errors in cone detection and, for this reason, the combined measurements of more parameters could be a better choice to characterize different retinal regions and the retinas of different subjects.

6.1.2 *Analysis of the cone mosaic over time*

We developed a largely automated procedure for the analysis of cone mosaic images, which includes image registration and flat-fielding as well as blood vessel segmentation and cone detection. We successfully applied the procedure for the monitoring of large retinal patches $\geq 2^\circ \times 2^\circ$ over short and long time scales, which are desirable features for use in clinical environments. We assessed that, for the purpose of cone detection, there is no significant difference in the images acquired with a light source that is within 0.35 mm off from the pupil center, which is the farthest location from the pupil center used by operators of the AO flood camera to acquire high-quality images of the cone mosaic in the clinic. In addition, the light position does not affect the ability to identify and track individual cones on a series of images. On the other hand, the time separation between two or more images makes the identification of the same cone more difficult. We determined that important changes in cone reflectance also occur on long time scales (days, months and years) and that these changes increase logarithmically with time.

6.1.3 *Cone mosaic reflectance in NPDR*

We applied the procedure for the analysis of the cone mosaic to perform a largely automated analysis of cone reflectance in eyes affected by mild NPDR as compared to a healthy population. We did not observe significant changes of the parameters related to reflectance with time in any group. We observed significant differences in cone mosaic reflectance properties between healthy eyes and eyes with mild NPDR, both in its spatial organization and in its intensity, especially between directional and non-directional backscattering. We introduced a novel method for the study of the spatial distribution of cone reflectance, the variogram. This method was able to quantify differences of the spatial dependence of cone intensities at a short range between NPDR and control eyes and a tendency of cones in NPDR to be clustered in clumps of similar intensities.

6.2 PROPOSAL FOR FUTURE WORK

6.2.1 *Reliability of automated cone detection*

In Paper I we gave an overview of the most used cone detection algorithms by comparing them side-by-side, specifying for each of them how they work, the number of parameters used and their behaviour in presence of different sources of image deterioration. We believe that with this study we created a useful baseline for us and future researchers that want to perform automated cone detection, as it is possible to choose the algorithm that not only performs the best, but that also best suits the specific needs of the researcher (e.g. if the segmentation of the cone aperture is required or if execution speed is preferred).

Further work can be carried out in this direction by improving the algorithm to simulate cone mosaics at different retinal eccentricities (consequently including rods in addition to cones only) and possibly with different retinal conditions. This last aspect can be of special importance, as the reliability of automated cone detection algorithms is questioned when the cone mosaic is not healthy or the image quality is poor [14]. The availability of a realistic simulation tool for the photoreceptor mosaic with different features could then be an essential tool for the development of accurate detection algorithms that can be relied upon, and so used on a large scale.

An interesting use of the simulation could be the production of a large number of synthetic photoreceptor layer images for those more advanced processing techniques that rely on a great amount of training data, such as machine learning [124]. Without a simulation method, in fact, the application of supervised machine learning or similar techniques to cone detection could be hard to achieve, as there is currently no large data set with “gold standard” manual detections available and it is plausible to believe that the realization of a large training data set of such characteristics would require a considerable amount of time and effort.

6.2.2 *Analysis of large retinal patches over time*

In Paper II we demonstrated that the analysis of large patches of the retina is possible. The exclusion of the blood vessel shadows allows the estima-

tion of cone mosaic parameters (e.g. density, regularity and spacing) at the exact designated retinal locations. One of the possible applications of this technique is the realization of maps of the parameters over extended areas, which could have potential in the monitoring of the retina especially in the identification of the onset of new areas of disruption in the cone mosaic. However, since new mosaic metrics are constantly being introduced and tested [53, 67], it will be important to understand which metrics would be the most suitable for this kind of analysis. In addition, an area of research could be understanding if the most efficient way to detect new mosaic disruption is the comparison with baseline measurements or the comparison with a theoretical model (e.g. randomly generated Poisson distribution).

6.2.3 *Biomarkers for diabetic retinopathy*

Some of the metrics that were explored in Paper III showed promising results as biomarkers for the early detection of changes in cone functionality in NPDR. An extension of this work should involve a greater number of subjects to assess if the difference in these metrics is still valid in a bigger population. Another aspect could be the application of the map-like approach (suggested in section Section 6.2.2) to the reflectance metrics and compare the map of the metrics over large retinal patches. In addition, the use of the variogram function could be further expanded. A direction of research could be the development of a standard analysis procedure, which would be able to retrieve information on the distribution of cone reflectance from the shape of the curves on scales larger than 20 μm .

BIBLIOGRAPHY

1. Artal, P., Benito, A. & Tabernero, J. The human eye is an example of robust optical design. *Journal of Vision* **6**, 1–7 (2006).
2. Lombardo, M., Serrao, S., Devaney, N., Parravano, M. & Lombardo, G. Adaptive optics technology for high-resolution retinal imaging. *Sensors (Switzerland)* **13**, 334–366 (2013).
3. Kolb, H. How the retina works. *American scientist* **91**, 28–35 (2003).
4. Kimbrel, E. A. & Lanza, R. Current status of pluripotent stem cells: moving the first therapies to the clinic. *Nature Reviews Drug Discovery* **14**, 681–692 (2015).
5. Kaufman, P., Alm, A. & Adler, F. *Adler's physiology of the eye: clinical application* (Mosby, 2003).
6. Atchison, D. & Smith, G. *Optics of the Human Eye* (Butterworth-Heinemann, 2000).
7. Mustafi, D., Engel, A. H. & Palczewski, K. Structure of cone photoreceptors. *Progress in Retinal and Eye Research* **28**, 289–302 (2009).
8. Porter, J., Queener, H., Lin, J., Thorn, K. & Awwal, A. *Adaptive Optics for Vision Science: Principles, Practices, Design and Applications* (Wiley, 2006).
9. Jonnal, R., Besecker, J., Derby, J., Kocaoglu, O., Cense, B., Gao, W., Wang, Q. & Miller, D. Imaging outer segment renewal in living human cone photoreceptors. *Optics Express* **18**, 5257–5270 (2010).
10. Pircher, M., Kroisamer, J. S., Felberer, F., Sattmann, H., Göttinger, E. & Hitzenberger, C. K. Temporal changes of human cone photoreceptors observed in vivo with SLO/OCT. *Biomedical Optics Express* **2**, 100–112 (2011).
11. Curcio, C. A., Sloan, K. R., Kalina, R. E. & Hendrickson, A. E. Human photoreceptor topography. *Journal of Comparative Neurology* **292**, 497–523 (1990).
12. Abramoff, M. D., Garvin, M. K. & Sonka, M. Retinal imaging and image analysis. *IEEE Reviews in Biomedical Engineering* **3**, 169–208 (2010).
13. Webb, R. H., Hughes, G. W. & Pomerantzef, O. Flying spot TV ophthalmoscope. *Applied Optics* **19**, 2991–2997 (1980).

14. Roorda, A. & Duncan, J. L. Adaptive optics ophthalmoscopy. *Annual review of vision science* **1**, 19–50 (2015).
15. Morgan, J. I. W. The fundus photo has met its match: optical coherence tomography and adaptive optics ophthalmoscopy are here to stay. *Ophthalmic and Physiological Optics* **36**, 218–239 (2016).
16. Saine, P. J. Landmarks in the historical development of fluorescein angiography. *The Journal of Ophthalmic Photography* **15**, 17–23 (1993).
17. Babcock, H. W. The possibility of compensating astronomical seeing. *Publications of the Astronomical Society of the Pacific* **65**, 229–236 (1953).
18. Liang, J., Williams, D. R. & Miller, D. T. Supernormal vision and high-resolution retinal imaging through adaptive optics. *Journal of the Optical Society of America A* **14**, 2884–2892 (1997).
19. Hampson, K. M. Adaptive optics and vision. *Journal of Modern Optics* **55**, 3423–3465 (2008).
20. Liang, J., Grimm, B., Goelz, S. & Bille, J. F. Objective measurement of wave aberrations of the human eye with the use of a Hartmann-Shack wave-front sensor. *Journal of the Optical Society of America A* **11**, 1949–1957 (1994).
21. Pircher, M. & Zawadzki, R. J. Review of adaptive optics OCT (AO-OCT): principles and applications for retinal imaging [Invited]. *Biomedical Optics Express* **8**, 2536–2562 (2017).
22. Roorda, A., Romero-Borja, F., Donnelly III, W. J., Queener, H., Hebert, T. J. & Campbell, M. C. Adaptive optics scanning laser ophthalmoscopy. *Optics Express* **10**, 405–412 (2002).
23. Miller, D. T., Qu, J., Jonnal, R. S. & Thorn, K. E. *Coherence gating and adaptive optics in the eye in Biomedical Optics* (2003), 65–72.
24. Putnam, N. M., Hammer, D. X., Zhang, Y., Merino, D. & Roorda, A. Modeling the foveal cone mosaic imaged with adaptive optics scanning laser ophthalmoscopy. *Optics Express* **18**, 24902–24916 (2010).
25. Carroll, J., Kay, D. B., Scoles, D., Dubra, A. & Lombardo, M. Adaptive Optics Retinal Imaging - Clinical Opportunities and Challenges. *Current Eye Research* **38**, 709–721 (2013).
26. Viard, C., Nakashima, K., Lamory, B., Pques, M., Levecq, X. & Chteau, N. *Imaging microscopic structures in pathological retinas using a flood-illumination adaptive optics retinal camera in SPIE BiOS (International Society for Optics and Photonics, 2011)*, 788509.

27. Salas, M., Drexler, W., Levecq, X., Lamory, B., Ritter, M., Prager, S., Hafner, J., Schmidt-Erfurth, U. & Pircher, M. Multi-modal adaptive optics system including fundus photography and optical coherence tomography for the clinical setting. *Biomedical Optics Express* **7**, 1783–1796 (2016).
28. Levecq, X. personal communication. Mar. 4, 2016.
29. Lombardo, M., Serrao, S., Ducoli, P. & Lombardo, G. Eccentricity dependent changes of density, spacing and packing arrangement of parafoveal cones. *Ophthalmic and Physiological Optics* **33**, 516–526 (2013).
30. Cornsweet, T. N. & Crane, H. D. Accurate two-dimensional eye tracker using first and fourth Purkinje images. *Journal of the Optical Society of America* **63**, 921–928 (1973).
31. Scoles, D., Sulai, Y. N. & Dubra, A. In vivo dark-field imaging of the retinal pigment epithelium cell mosaic. *Biomedical Optics Express* **4**, 1710–1723 (2013).
32. Chui, T. Y. P., Gast, T. J. & Burns, S. A. Imaging of Vascular Wall Fine Structure in the Human Retina Using Adaptive Optics Scanning Laser Ophthalmoscopy. *Investigative Ophthalmology & Visual Science* **54**, 7115–7124 (2013).
33. Sulai, Y. N., Scoles, D., Harvey, Z. & Dubra, A. Visualization of retinal vascular structure and perfusion with a nonconfocal adaptive optics scanning light ophthalmoscope. *Journal of the Optical Society of America A* **31**, 569–579 (2014).
34. Liu, Z., Kurokawa, K., Zhang, F. & Miller, D. T. In vivo imaging of human retinal ganglion cells with AO-OCT. *Investigative Ophthalmology & Visual Science* **58**, 3430–3430 (2017).
35. Liu, Z., Kocaoglu, O. P. & Miller, D. T. 3D Imaging of Retinal Pigment Epithelial Cells in the Living Human Retina 3D Imaging of RPE Cells in Living Human Retina. *Investigative ophthalmology & visual science* **57**, OCT533–OCT543 (2016).
36. Vohnsen, B. Photoreceptor waveguides and effective retinal image quality. *Journal of the Optical Society of America A* **24**, 597–607 (2007).
37. Rativa, D. & Vohnsen, B. Analysis of individual cone-photoreceptor directionality using scanning laser ophthalmoscopy. *Biomedical Optics Express* **2**, 1423–1431 (2011).
38. Vohnsen, B. Directional sensitivity of the retina: A layered scattering model of outer-segment photoreceptor pigments. *Biomedical Optics Express* **5**, 1569–1587 (2014).

39. Jacob, J., Paques, M., Krivosic, V., Dupas, B., Couturier, A., Kulcsar, C., Tadayoni, R., Massin, P. & Gaudric, A. Meaning of Visualizing Retinal Cone Mosaic on Adaptive Optics Images. *American Journal of Ophthalmology* **159**, 118–123 (2015).
40. Jonnal, R., Rha, J., Zhang, Y., Cense, B., Gao, W. & Miller, D. In vivo functional imaging of human cone photoreceptors. *Optics Express* **15**, 16141–16160 (2007).
41. Snyder, A. W. & Pask, C. The Stiles-Crawford effect—explanation and consequences. *Vision Research* **13**, 1115–1137 (1973).
42. Pallikaris, A., Williams, D. R. & Hofer, H. The reflectance of single cones in the living human eye. *Investigative Ophthalmology & Visual Science* **44**, 4580–4592 (2003).
43. Scoles, D., Sulai, Y. N., Langlo, C. S., Fishman, G. A., Curcio, C. A., Carroll, J. & Dubra, A. In vivo imaging of human cone photoreceptor inner segments. *Investigative Ophthalmology & Visual Science* **55**, 4244–4251 (2014).
44. Hunter, J. J., Masella, B., Dubra, A., Sharma, R., Yin, L., Merigan, W. H., Palczewska, G., Palczewski, K. & Williams, D. R. Images of photoreceptors in living primate eyes using adaptive optics two-photon ophthalmoscopy. *Biomedical Optics Express* **2**, 139–148 (2011).
45. Williams, D. & Collier, R. Consequences of spatial sampling by a human photoreceptor mosaic. *Science* **221**, 385–387 (1983).
46. Williams, D. R. & Coletta, N. J. Cone spacing and the visual resolution limit. *Journal of the Optical Society of America A* **4**, 1514–1523 (1987).
47. Yellott, J. I. Spectral consequences of photoreceptor sampling in the rhesus retina. *Science* **221**, 382–385 (1983).
48. Wolfing, J. I., Chung, M., Carroll, J., Roorda, A. & Williams, D. R. High-resolution retinal imaging of cone–rod dystrophy. *Ophthalmology* **113**, 1014–1019 (2006).
49. Choi, S. S., Doble, N., Hardy, J. L., Jones, S. M., Keltner, J. L., Olivier, S. S. & Werner, J. S. In vivo imaging of the photoreceptor mosaic in retinal dystrophies and correlations with visual function. *Investigative Ophthalmology & Visual Science* **47**, 2080–2092 (2006).
50. Duncan, J. L., Zhang, Y., Gandhi, J., Nakanishi, C., Othman, M., Branham, K. E., Swaroop, A. & Roorda, A. High-resolution imaging with adaptive optics in patients with inherited retinal degeneration. *Investigative Ophthalmology & Visual Science* **48**, 3283–3291 (2007).

51. Curcio, C. A., Medeiros, N. E. & Millican, C. L. Photoreceptor loss in age-related macular degeneration. *Investigative Ophthalmology & Visual Science* **37**, 1236–1249 (1996).
52. Chui, T. Y. P., Song, H. & Burns, S. A. Adaptive-optics imaging of human cone photoreceptor distribution. *Journal of the Optical Society of America A* **25**, 3021–3029 (2008).
53. Giannini, D., Lombardo, G., Mariotti, L., Devaney, N., Serrao, S. & Lombardo, M. Reliability and Agreement Between Metrics of Cone Spacing in Adaptive Optics Images of the Human Retinal Photoreceptor Mosaic. *Investigative Ophthalmology & Visual Science* **58**, 3127–3137 (2017).
54. Brostow, W., Dussault, J.-P. & Fox, B. L. Construction of Voronoi polyhedra. *Journal of Computational Physics* **29**, 81–92 (1978).
55. Li, K. Y. & Roorda, A. Automated identification of cone photoreceptors in adaptive optics retinal images. *Journal of the Optical Society of America A* **24**, 1358–1363 (2007).
56. Park, S. P., Chung, J. K., Greenstein, V., Tsang, S. H. & Chang, S. A study of factors affecting the human cone photoreceptor density measured by adaptive optics scanning laser ophthalmoscope. *Experimental Eye Research* **108**, 1–9 (2013).
57. Bidaut Garnier, M., Flores, M., Debellemanière, G., Puyraveau, M., Tumahai, P., Meillat, M., Schwartz, C., Montard, M., Delbosc, B. & Saleh, M. Reliability of cone counts using an adaptive optics retinal camera. *Clinical & Experimental Ophthalmology* **42**, 833–840 (2014).
58. Lombardo, M., Serrao, S., Ducoli, P. & Lombardo, G. Influence of sampling window size and orientation on parafoveal cone packing density. *Biomedical Optics Express* **4**, 1318–1331 (2013).
59. Lombardo, M., Serrao, S. & Lombardo, G. Technical factors influencing cone packing density estimates in adaptive optics flood illuminated retinal images. *PLoS ONE* **9**, e107402 (2014).
60. Muthiah, M. N., Gias, C., Chen, F. K., Zhong, J., McClelland, Z., Sallo, F. B., Peto, T., Coffey, P. J. & da Cruz, L. Cone photoreceptor definition on adaptive optics retinal imaging. *British Journal of Ophthalmology* **98**, 1073–1079 (2014).
61. Nesper, P. L., Scarinci, F. & Fawzi, A. A. Adaptive Optics Reveals Photoreceptor Abnormalities in Diabetic Macular Ischemia. *PLoS ONE* **12**, 1–16 (Jan. 2017).

62. Rodieck, R. The density recovery profile: a method for the analysis of points in the plane applicable to retinal studies. *Visual neuroscience* **6**, 95–111 (1991).
63. Garrioch, R., Langlo, C., Dubis, A. M., Cooper, R. F., Dubra, A. & Carroll, J. Repeatability of in vivo parafoveal cone density and spacing measurements. *Optometry and Vision Science* **89**, 632–643 (2012).
64. Chui, T. Y. P., Song, H. & Burns, S. A. Individual Variations in Human Cone Photoreceptor Packing Density: Variations with Refractive Error. *Investigative Ophthalmology & Visual Science* **49**, 4679–4687 (2008).
65. Roorda, A., Metha, A. B., Lennie, P. & Williams, D. R. Packing arrangement of the three cone classes in primate retina. *Vision Research* **41**, 1291–1306 (2001).
66. Sawides, L., de Castro, A. & Burns, S. A. The organization of the cone photoreceptor mosaic measured in the living human retina. *Vision Research* **132**, 34–44 (2017).
67. Cooper, R. F., Wilk, M. A., Tarima, S. & Carroll, J. Evaluating Descriptive Metrics of the Human Cone Mosaic. *Investigative Ophthalmology & Visual Science* **57**, 2992–3001 (2016).
68. Rha, J., Schroeder, B., Godara, P. & Carroll, J. Variable optical activation of human cone photoreceptors visualized using a short coherence light source. *Optics Letters* **34**, 3782–3784 (2009).
69. Cooper, R. F., Dubis, A. M., Pavaskar, A., Rha, J., Dubra, A. & Carroll, J. Spatial and temporal variation of rod photoreceptor reflectance in the human retina. *Biomedical Optics Express* **2**, 2577–2589 (2011).
70. Bedggood, P. & Metha, A. Variability in bleach kinetics and amount of photopigment between individual foveal cones. *Investigative Ophthalmology & Visual Science* **53**, 3673–3681 (2012).
71. Bedggood, P. & Metha, A. Optical imaging of human cone photoreceptors directly following the capture of light. *PLoS ONE* **8**, e79251 (2013).
72. Westheimer, G. Directional sensitivity of the retina: 75 years of Stiles–Crawford effect. *Proceedings of the Royal Society of London B: Biological Sciences* **275**, 2777–2786 (2008).
73. Burns, S., Wu, S., He, J. & Elsner, A. Variations in photoreceptor directionality across the central retina. *Journal of the Optical Society of America A* **14**, 2033–2040 (1997).
74. Roorda, A. & Williams, D. Optical fiber properties of individual human cones. *Journal of Vision* **2**, 404–412 (2002).

75. Miloudi, C., Rossant, F., Bloch, I., Chaumette, C., Leseigneur, A., Sahel, J.-A., Meimon, S., Mrejen, S. & Paques, M. The negative cone mosaic: A new manifestation of the optical stiles-crawford effect in normal eyes. *Investigative Ophthalmology & Visual Science* **56**, 7043–7050 (2015).
76. Langlo, C. S., Erker, L. R., Parker, M., Patterson, E. J., Higgins, B. P., Summerfelt, P., Razeen, M. M., Collison, F. T., Fishman, G. A., Kay, C. N., *et al.* Repeatability and longitudinal assessment of foveal cone structure in CNG83-associated achromatopsia. *Retina* (2017).
77. Talcott, K. E., Ratnam, K., Sundquist, S. M., Lucero, A. S., Lujan, B. J., Tao, W., Porco, T. C., Roorda, A. & Duncan, J. L. Longitudinal study of cone photoreceptors during retinal degeneration and in response to ciliary neurotrophic factor treatment. *Investigative Ophthalmology & Visual Science* **52**, 2219–2226 (2011).
78. Dubis, A. M., Cooper, R. F., Aboshiha, J., Langlo, C. S., Sundaram, V., Liu, B., Collison, F., Fishman, G. A., Moore, A. T., Webster, A. R., Dubra, A., Carroll, J. & Michaelides, M. Genotype-Dependent Variability in Residual Cone Structure in Achromatopsia: Toward Developing Metrics for Assessing Cone Health. *Investigative Ophthalmology & Visual Science* **55**, 7303–7311 (2014).
79. Kotecha, A., Fernandes, S., Bunce, C. & Franks, W. A. Avoidable sight loss from glaucoma: is it unavoidable? *British Journal of Ophthalmology* **96**, 816–820 (2012).
80. Alencar, L. M., Zangwill, L. M., Weinreb, R. N., Bowd, C., Sample, P. A., Girkin, C. A., Liebmann, J. M. & Medeiros, F. A. A comparison of rates of change in neuroretinal rim area and retinal nerve fiber layer thickness in progressive glaucoma. *Investigative Ophthalmology & Visual Science* **51**, 3531–3539 (2010).
81. Takayama, K., Ooto, S., Hangai, M., Arakawa, N., Oshima, S., Shibata, N., Hanebuchi, M., Inoue, T. & Yoshimura, N. High-resolution imaging of the retinal nerve fiber layer in normal eyes using adaptive optics scanning laser ophthalmoscopy. *PLoS ONE* **7**, e33158 (2012).
82. Kocaoglu, O. P., Cense, B., Jonnal, R. S., Wang, Q., Lee, S., Gao, W. & Miller, D. T. Imaging retinal nerve fiber bundles using optical coherence tomography with adaptive optics. *Vision Research* **51**, 1835–1844 (2011).

83. Chakravarthy, U., Wong, T. Y., Fletcher, A., Piauult, E., Evans, C., Zlateva, G., Buggage, R., Pleil, A. & Mitchell, P. Clinical risk factors for age-related macular degeneration: a systematic review and meta-analysis. *BMC ophthalmology* **10**, 31 (2010).
84. Lim, L. S., Mitchell, P., Seddon, J. M., Holz, F. G. & Wong, T. Y. Age-related macular degeneration. *The Lancet* **379**, 1728–1738 (2012).
85. Godara, P., Wagner-Schuman, M., Rha, J., Connor Jr, T. B., Stepien, K. E. & Carroll, J. in *Retinal Degenerative Diseases* 451–458 (Springer, 2012).
86. Cunha-Vaz, J. G. Pathophysiology of diabetic retinopathy. *British Journal of Ophthalmology* **62**, 351–355 (1978).
87. Kern, T. S. & Engerman, R. L. Vascular lesions in diabetes are distributed non-uniformly within the retina. *Experimental Eye Research* **60**, 545–549 (1995).
88. Moore, J., Bagley, S., Ireland, G., McLeod, D. & Boulton, M. Three dimensional analysis of microaneurysms in the human diabetic retina. *Journal of Anatomy* **194**, 89–100 (1999).
89. Early Treatment Diabetic Retinopathy Study Research Group. Fundus Photographic Risk Factors for Progression of Diabetic Retinopathy. *Ophthalmology* **98**, 823–833 (1991).
90. Steinle, N. C. & Ambati, J. in *The Retina and its Disorders* (eds Besharse, J. & Bok, D.) 781–789 (Academic Press, 2011).
91. Mookiah, M. R. K., Acharya, U. R., Chua, C. K., Lim, C. M., Ng, E. & Laude, A. Computer-aided diagnosis of diabetic retinopathy: A review. *Computers in Biology and Medicine* **43**, 2136–2155 (2013).
92. Barber, A. J. A new view of diabetic retinopathy: a neurodegenerative disease of the eye. *Progress in Neuro-Psychopharmacology and Biological Psychiatry* **27**, 283–290 (2003).
93. Fletcher, E. L., Phipps, J. A. & Wilkinson-Berka, J. L. Dysfunction of retinal neurons and glia during diabetes. *Clinical & Experimental Optometry* **88**, 132–145 (2005).
94. Verma, A., Rani, P. K., Raman, R., Pal, S. S., Laxmi, G., Gupta, M., Sahu, C., Vaitheeswaran, K. & Sharma, T. Is neuronal dysfunction an early sign of diabetic retinopathy? Microperimetry and Spectral Domain Optical Coherence Tomography (SD-OCT) Study in individuals with diabetes, but no diabetic retinopathy. *Eye* **23**, 1824–1830 (2009).

95. Van Dijk, H. W., Verbraak, F. D., Kok, P. H. B., Stehouwer, M., Garvin, M. K., Sonka, M., DeVries, J. H., Schlingemann, R. O. & Abràmoff, M. D. Early Neurodegeneration in the Retina of Type 2 Diabetic Patients. *Investigative Ophthalmology & Visual Science* **53**, 2715–2719 (2012).
96. Stem, M. S. & Gardner, T. W. Neurodegeneration in the Pathogenesis of Diabetic Retinopathy: Molecular Mechanisms and Therapeutic Implications. *Current Medicinal Chemistry* **20**, 3241–3250 (2013).
97. Ola, M. S., Nawaz, M. I., Khan, H. A. & Alhomida, A. S. Neurodegeneration and Neuroprotection in Diabetic Retinopathy. *International Journal of Molecular Sciences* **14**, 2559–2572 (2013).
98. Simó, R. & Hernández, C. Neurodegeneration in the diabetic eye: new insights and therapeutic perspectives. *Trends in Endocrinology & Metabolism* **25**, 23–33 (2014).
99. Lieth, E., Gardner, T. W., Barber, A. J. & Antonetti, D. A. Retinal neurodegeneration: early pathology in diabetes. *Clinical & Experimental Ophthalmology* **28**, 3–8 (2000).
100. Van Dijk, H. W., Kok, P. H., Garvin, M., Sonka, M., DeVries, J. H., Michels, R. P., van Velthoven, M. E., Schlingemann, R. O., Verbraak, F. D. & Abràmoff, M. D. Selective loss of inner retinal layer thickness in type 1 diabetic patients with minimal diabetic retinopathy. *Investigative Ophthalmology & Visual Science* **50**, 3404–3409 (2009).
101. Sohn, E. H., van Dijk, H. W., Jiao, C., Kok, P. H. B., Jeong, W., Demirkaya, N., Garmager, A., Wit, F., Kucukevcilioglu, M., van Velthoven, M. E. J., DeVries, J. H., Mullins, R. F., Kuehn, M. H., Schlingemann, R. O., Sonka, M., Verbraak, F. D. & Abràmoff, M. D. Retinal neurodegeneration may precede microvascular changes characteristic of diabetic retinopathy in diabetes mellitus. *Proceedings of the National Academy of Sciences* **113**, E2655–E2664 (2016).
102. Lombardo, M., Parravano, M., Lombardo, G., Varano, M., Boccassini, B., Stirpe, M. & Serrao, S. Adaptive optics imaging of parafoveal cones in type 1 diabetes. *Retina* **34**, 546–557 (2014).
103. Lombardo, M., Parravano, M., Serrao, S., Ziccardi, L., Giannini, D. & Lombardo, G. Investigation of Adaptive Optics Imaging Biomarkers for Detecting Pathological Changes of the Cone Mosaic in Patients with Type 1 Diabetes Mellitus. *PLoS ONE* **11**, e0151380 (2016).

104. Lammer, J., Prager, S. G., Cheney, M. C., Ahmed, A., Radwan, S. H., Burns, S. A., Silva, P. S. & Sun, J. K. Cone Photoreceptor Irregularity on Adaptive Optics Scanning Laser Ophthalmoscopy Correlates With Severity of Diabetic Retinopathy and Macular Edema. *Investigative Ophthalmology & Visual Science* **57**, 6624–6632 (2016).
105. Chui, T. Y. P., Dubow, M., Pinhas, A., Shah, N., Gan, A., Weitz, R., Sulai, Y. N., Dubra, A. & Rosen, R. B. Comparison of adaptive optics scanning light ophthalmoscopic fluorescein angiography and offset pinhole imaging. *Biomedical Optics Express* **5**, 1173–1189 (2014).
106. Dubow, M., Pinhas, A., Shah, N., Cooper, R. F., Gan, A., Gentile, R. C., Hendrix, V., Sulai, Y. N., Carroll, J., Chui, T. Y. P., Walsh, J. B., Weitz, R., Dubra, A. & Rosen, R. B. Classification of Human Retinal Microaneurysms Using Adaptive Optics Scanning Light Ophthalmoscope Fluorescein Angiography. *Investigative Ophthalmology & Visual Science* **55**, 1299–1309 (2014).
107. Tam, J., Dhamdhere, K. P., Tiruveedhula, P., Manzanera, S., Barez, S., Bearse, M. A., Adams, A. J. & Roorda, A. Disruption of the retinal parafoveal capillary network in type 2 diabetes before the onset of diabetic retinopathy. *Investigative Ophthalmology & Visual Science* **52**, 9257–9266 (2011).
108. Salas, M., Augustin, M., Ginner, L., Kumar, A., Baumann, B., Leitgeb, R., Drexler, W., Prager, S., Hafner, J., Schmidt-Erfurth, U. & Pircher, M. Visualization of micro-capillaries using optical coherence tomography angiography with and without adaptive optics. *Biomedical Optics Express* **8**, 207–222 (2017).
109. Matsui, M., Tashiro, T., Matsumoto, K. & Yamamoto, S. A study on automatic and quantitative diagnosis of fundus photographs. I. Detection of contour line of retinal blood vessel images on color fundus photographs (author's transl). *Nippon Ganka Gakkai Zasshi* **77**, 907–918 (1973).
110. Baudoin, C., Lay, B. & Klein, J. Automatic detection of microaneurysms in diabetic fluorescein angiography. *Revue d'épidémiologie et de santé publique* **32**, 254–261 (1983).
111. Patton, N., Aslam, T. M., MacGillivray, T., Deary, I. J., Dhillon, B., Eikelboom, R. H., Yegesan, K. & Constable, I. J. Retinal image analysis: Concepts, applications and potential. *Progress in Retinal and Eye Research* **25**, 99–127 (2006).
112. Changhui Rao Yu Tian, H. B. in (ed Tyson, R. K.) chap. AO-Based High Resolution Image Post-Processing (InTech, 2012).

113. Christou, J. C., Roorda, A. & Williams, D. R. Deconvolution of adaptive optics retinal images. *Journal of the Optical Society of America A* **21**, 1393–1401 (2004).
114. Vogel, C. R., Arathorn, D. W., Roorda, A. & Parker, A. Retinal motion estimation in adaptive optics scanning laser ophthalmoscopy. *Optics Express* **14**, 487–497 (2006).
115. Tomaževič, D., Likar, B. & Pernuš, F. Comparative evaluation of retrospective shading correction methods. *Journal of Microscopy* **208**, 212–223 (2002).
116. Russ, J. *The image processing handbook* 7th (CRC press, 2016).
117. Ramaswamy, G. *Pre-processing, Registration and Quality Assessment of Adaptive Optics Assisted Retinal Images* PhD thesis (National University of Ireland, Galway, 2014).
118. Ramaswamy, G. & Devaney, N. Pre-processing, registration and selection of adaptive optics corrected retinal images. *Ophthalmic and Physiological Optics* **33**, 527–539 (2013).
119. Trucco, E., Ruggeri, A., Karnowski, T., Giancardo, L., Chaum, E., Hubschman, J. P., al Diri, B., Cheung, C. Y., Wong, D., Abràmoff, M., Lim, G., Kumar, D., Burlina, P., Bressler, N. M., Jelinek, H. F., Meriaudeau, F., Quellec, G., MacGillivray, T. & Dhillon, B. Validating Retinal Fundus Image Analysis Algorithms: Issues and a Proposal. *Investigative Ophthalmology & Visual Science* **54**, 3546–3559 (2013).
120. Putnam, N. M., Hofer, H. J., Doble, N., Chen, L., Carroll, J. & Williams, D. R. The locus of fixation and the foveal cone mosaic. *Journal of Vision* **5**, 3 (2005).
121. Kitaguchi, Y., Bessho, K., Yamaguchi, T., Nakazawa, N., Mihashi, T. & Fujikado, T. In vivo measurements of cone photoreceptor spacing in myopic eyes from images obtained by an adaptive optics fundus camera. *Japanese Journal of Ophthalmology* **51**, 456–461 (2007).
122. Jan, J., Odstrcilik, J., Gazarek, J. & Kolar, R. Retinal image analysis aimed at blood vessel tree segmentation and early detection of neural-layer deterioration. *Computerized Medical Imaging and Graphics* **36**, 431–441 (2012).
123. Fraz, M., Remagnino, P., Hoppe, A., Uyyanonvara, B., Rudnicka, A., Owen, C. & Barman, S. Blood vessel segmentation methodologies in retinal images - A survey. *Computer Methods and Programs in Biomedicine* **108**, 407–433 (2012).

BIBLIOGRAPHY

124. Bergeles, C., Dubis, A. M., Davidson, B., Kasilian, M., Kalitzeos, A., Carroll, J., Dubra, A., Michaelides, M. & Ourselin, S. Unsupervised identification of cone photoreceptors in non-confocal adaptive optics scanning light ophthalmoscope images. *Biomedical Optics Express* **8**, 3081–3094 (2017).
125. Hedeker, D. & Gibbons, R. *Longitudinal Data Analysis* (Wiley, 2006).
126. Brown, H. & Prescott, R. *Applied Mixed Models in Medicine* 2nd Edition (Wiley, 2006).

APPENDIX: ADDITIONAL IMAGES

Due to limitations in space and guidelines for the publication of Paper II, some images were not included in the final version of the paper. We include here a visual example of the advantage of performing blood vessel segmentation on the cone mosaic over manual selection (Figure A.1) and the results of the complete processing of the cone mosaic on the images in Paper II (Figure A.2 and Figure A.3).

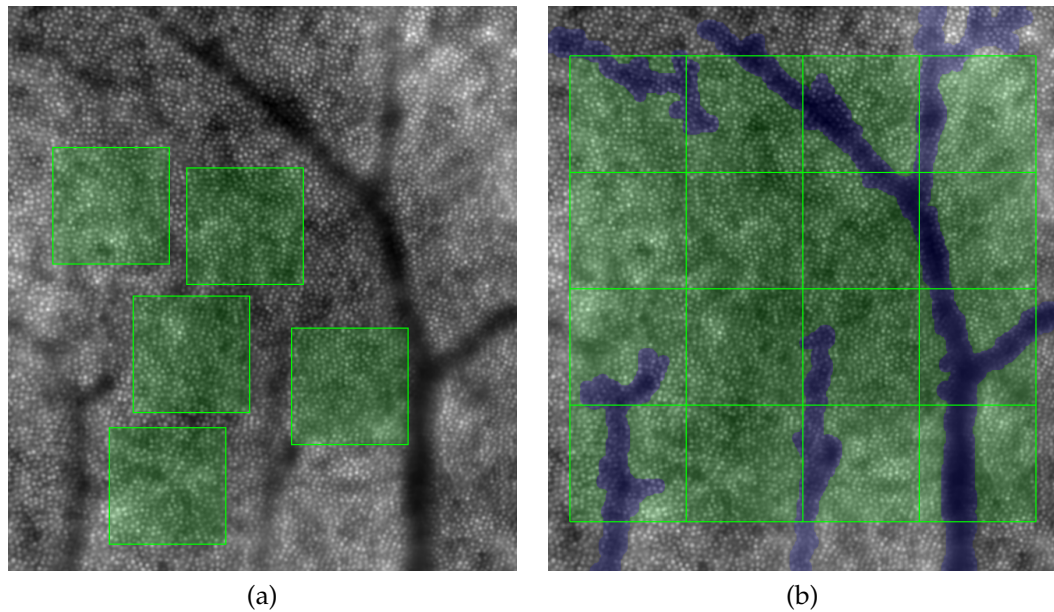


Figure A.1: (a) Example of manual selection of $160 \mu\text{m} \times 160 \mu\text{m}$ windows for the estimation of cone mosaic parameters. (b) Example of automated selection of windows of the same size with the exclusion of the area occupied by the vessel shadows. The area that is analysed is here maximised and covers the whole image, in addition to the elimination of the manual selection of the position of the windows.

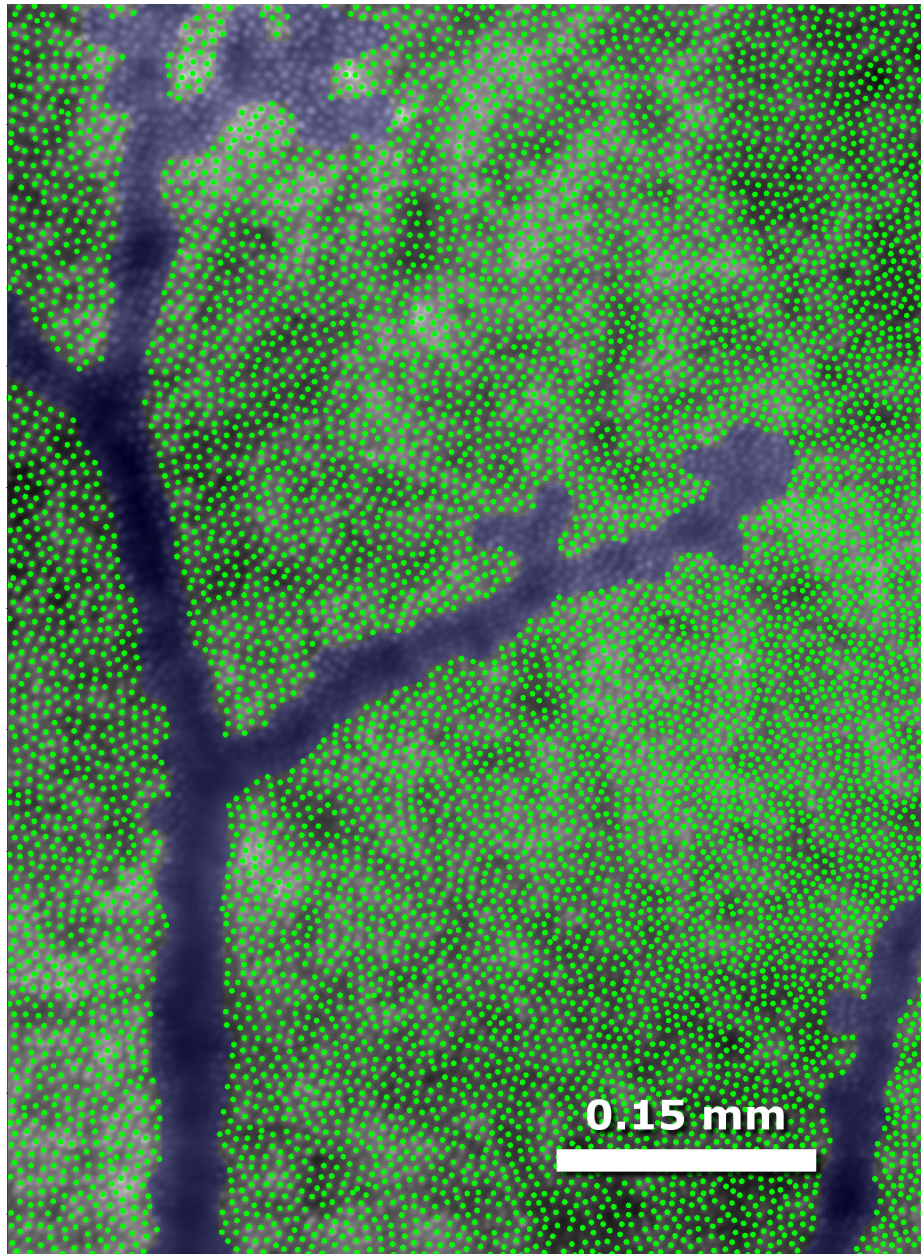


Figure A.2: Cone detection and blood vessel segmentation on the cone mosaic 2.5° temporal from the fovea. The image used is the time-average of all the images acquired at 2.5° on the subject studied in Paper II. The size of the image is $2.0^\circ \times 2.8^\circ$.

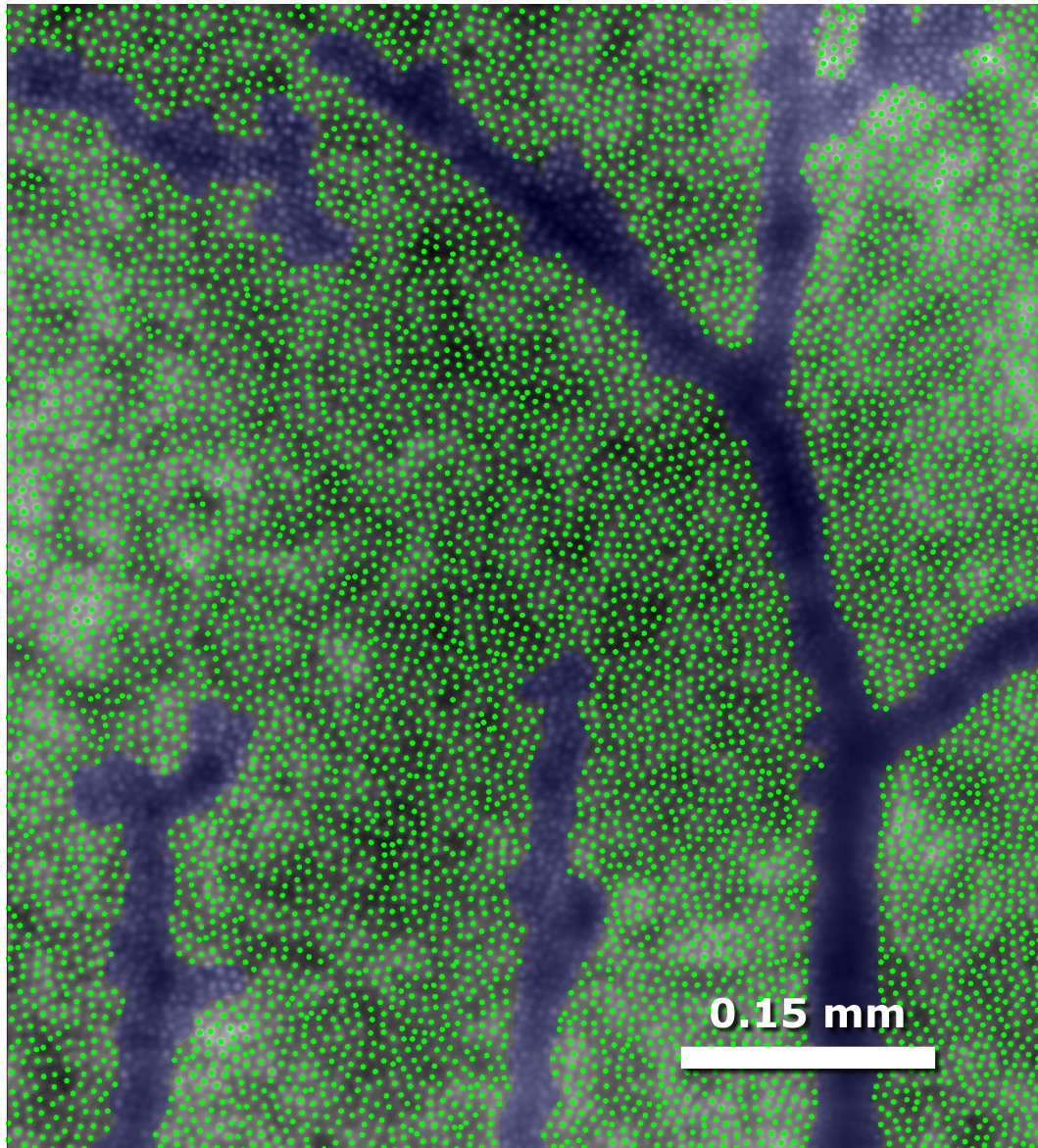


Figure A.3: Cone detection and blood vessel segmentation on the cone mosaic 4° temporal from the fovea. The image used is the time-average of all the images acquired at 4° on the subject studied in Paper II. The size of the image is $2.3^\circ \times 2.6^\circ$.

APPENDIX: DETAILS ON STATISTICAL ANALYSIS

The main purpose of the statistical analysis performed in Paper III was to determine if we could observe a significant difference in parameters related to cone reflectance between the two groups (control and mild NPDR). In addition, another important characteristic of the data set is that it included images acquired with a maximum of five year separation in time. Because of this, the influence of time is also an important factor that needed to be studied, in order to determine if cone reflectance showed significant long-time trends.

B.1 CHOICE OF A MIXED MODEL

The most common method used for the comparison between group means is the analysis of variance (ANOVA). One of the assumptions of traditional ANOVA is that measurements must not present correlation, which generally fails in the case of longitudinal data analysis (i.e. repeated measurements within the same subjects). To deal with the correlation, other variants of ANOVA have been introduced, e.g. repeated measures ANOVA or multivariate ANOVA. However, a limitation that still remains in ANOVA variants is that all results are discarded for any subject missing at least one measurement [125]. Since we had to deal with a number of missing observations for most of the subjects, I decided to apply a mixed model approach instead.

The term “mixed model” refers to the fact that two type of effects, fixed and random, are both included in the same analysis. An effect is said to be fixed when it is constant across individuals. In our analysis, I took into consideration three different fixed effects (time, retinal location and condition). These fixed effects were again divided in two categories, intra-subjects and inter-subjects. Time (year) and retinal location (2 degrees temporal, superior, nasal and inferior) were considered to be intra-subjects, as they implied repeated measurements on the same subject. Condition (healthy or

NPDR) was treated as a inter-subjects factor, as each subject could belong to only one category and it implied the division in two study groups.

The main reason behind my choice to include the random effects in the analysis is that it has been shown that the spatial metrics related to the cone mosaic present a high degree of variability even in the healthy population (Section 1.2.3.2, [2]). It was therefore also reasonable to assume that the metrics related to cone reflectance might show a high between-subject variability. This means that if we have a linear mixed model where the measurements are fitted against the fixed effects with a linear regression relationship, the addition of random effects let each subject have his/her own “personal” linear relationship, with individual intercepts and/or slopes that are distributed around the respective group mean (control or mild NPDR) following a normal distribution.

Using the same notation as in [126], a linear mixed model can be formally expressed as :

$$\mathbf{y} = \mathbf{X}\boldsymbol{\alpha} + \mathbf{Z}\boldsymbol{\beta} + \mathbf{e}$$

where

$$\begin{aligned} \mathbf{y} &= (y_1, y_2, y_3, \dots, y_n)' = \text{observed values} \\ \boldsymbol{\alpha} &= (\mu, \alpha_1, \alpha_2, \dots, \alpha_p)' = \text{fixed effects parameters} \\ \mathbf{e} &= (e_1, e_2, e_3, \dots, e_n)' = \text{residuals} \\ \boldsymbol{\beta} &= (\beta_1, \beta_2, \dots, \beta_q)' = \text{random effects parameters} \end{aligned}$$

and where \mathbf{X} is a $n \times p$ matrix (know as the design matrix) that specifies values of fixed effects corresponding to each parameter for each observation. \mathbf{Z} is a second $n \times q$ design matrix that specifies the values of the random effects corresponding to each observation. The μ parameter in $\boldsymbol{\alpha}$ corresponds to the intercept. For more details on mixed models, we remand to the specific literature [125, 126].

B.2 PROCEDURE FOR THE ANALYSIS OF THE DATA

As explained in the methods of Paper III, the parameters calculated on all the sample images were processed in two ways in order to determine if there was a significant interaction between the parameters and either the

condition of the subject, time or the retinal location. They were analysed either considering the four retinal locations separately for each subject or the average of the parameters over the four retinal locations for each subject at each time point. This approach allowed us to determine if it was possible to use only one global “clinically useful value” for the parafoveal cone mosaic reflectance that would allow discrimination between healthy and mild NPDR retinas.

Data were tested for normality with the Shapiro-Wilk test. The 95% confidence intervals were calculated as $\pm 1.96 \sigma / \sqrt{n}$, where n is the number of observations and σ is the standard deviation. Statistical analysis of the results was performed with SPSS software (version 23; SPSS Inc., Chicago, IL, USA). All the possible interactions between the factors and inclusion of random effects were tested (an overview is shown in Table B.1).

The different explanatory models for each parameter were compared using the Bayesian Information Criterion (BIC) for the penalized likelihood [125]. The BIC number penalises the likelihood based on the number of parameters in the model and the number of subjects, following the idea that it is preferred to use a simpler model where possible. The analysis was performed for each parameter by starting from the most complex model, with all possible random effects and interaction terms, and then progressively removing terms, to remain with the main effects only. The process allowed me to create a table of BIC values for all models of each parameter. Finally, the model that minimized the BIC number was chosen as the best fitting

Table B.1: Overview of the effects and interactions that were examined during the test for different explanatory models. The main effects are abbreviated as follows: condition *C*, time *T* and retinal location *L*. Condition *C* is highlighted using a bold and italic font, to stress the fact that it is a between-group factor and not a within-subject factor such as time and location. Each random effect was added with respect to the fixed effect shown in brackets.

	Main fixed effects	Fixed effects interactions	Random effects
All retinal locations	1: <i>C</i> , <i>T</i> , <i>L</i>	2: <i>T</i> * <i>L</i> , <i>T</i> * <i>C</i> , <i>L</i> * <i>C</i> 3: <i>T</i> * <i>L</i> * <i>C</i>	intercept (<i>T</i>), slope (<i>T</i>), intercept (<i>L</i>), slope (<i>L</i>)
Mean of retinal locations	1: <i>C</i> , <i>T</i>	2: <i>T</i> * <i>C</i>	intercept (<i>T</i>), slope (<i>T</i>)

Table B.2: BIC values for the mean cone intensity (averaged between the four retinal locations) calculated for all possible models. The best explanatory model is found to be the one with the main effects C and T and random intercept with respect to T (the corresponding row is highlighted with a bold font).

Main effect C	Main effect T	Interaction T*C	Random intercept (T)	Random slope (T)	BIC
Yes	Yes	Yes	Yes	Yes	-514.177
Yes	Yes	Yes	Yes	No	-535.375
Yes	Yes	No	Yes	Yes	-529.134
Yes	Yes	No	Yes	No	-551.130
Yes	Yes	No	No	No	-528.759

one. Table B.2 shows an example of BIC table calculated for the mean cone intensity on the mean of locations values.

B.3 INTERPRETATION OF THE RESULTS

The best fitting model in all cases was determined to be the one with the main effects and random intercept only (intercept with respect to time in the case of the mean of locations, intercept with respect to both time and location if all four locations were considered). This means that no interactions between the factors were observed. I decided not to go further and try to remove one by one the main effects, but instead to use the same model for all parameters (main effects and random intercept) and then produce two tables of p-values that we could use to determine which effect was significant and which one was not (Tables 1 and 2 in Paper III).

The significance of the different terms was examined extensively in the Discussion section of the paper; here we add only a couple of comments. From the results, the interaction with time and retinal location were shown to be non-significant. This means that the fit of the data was consistent in both cases with a horizontal line, so we could use the intercepts as estimates for the parameter values for the two groups. This also is consistent with the fact that the addition of a random slope did not improve the fit of the models.

The last columns of Table 1 and Table 2 report the value of the Wald Z statistic test for the random intercept, which is the significance of the

hypothesis that the intercept variance is zero. If the null hypothesis is rejected ($p \leq 0.05$) then we can conclude that the random intercept is needed. Indeed, the random intercept was shown to be necessary for most parameters, in accordance with the initial intuition that a great between-subject variability has to be accounted for.